# Tunable Plasmon-induced Charge Transport and Photon Absorption of Bimetallic Au/Ag Nanoparticles on ZnO Photoanode for Photoelectrochemical Enhancement under Visible Light


Lim Fang Sheng

B.Hons. Eng (Mechanical Engineering, Monash University Malaysia)

23767030


**Supervised by:**

Dr. Chang Wei Sea

Dr. Yap Chi Chin

A Thesis submitted in partial fulfilment of the requirements for the degree of Doctor of Philosophy at Monash University in 2020

Department of Mechanical Engineering, Faculty of Engineering

# COPYRIGHT NOTICE

©Lim Fang Sheng (2020). I certify that I have made all reasonable efforts to secure copyright permissions for third-party content included in this thesis and have not knowingly added copyright content to my work without the owner's permission.

# DECLARATION

This thesis contains no material which has been accepted for the award of any other degree or diploma at any university or equivalent institution and that, to the best of my knowledge and belief, this thesis contains no material previously published or written by another person, except where due reference is made in the text of the thesis.

Lim Fang Sheng

May 2020

# ACKNOWLEDGEMENTS

I would like to use this opportunity to express my gratitude towards the following people who have supported and guided me throughout my research journey in Monash Unviersity Malaysia.

First of all, I would like to show my deepest gratitude to my supervisor, Dr. Chang Wei Sea for her constant support and willingness to share her time and knowledge with me. The supervision and support given have aided in the progress of achieving the objective of the project. Also, she has provided critical feedback on my research which aided me in completing my research. In addition to that, my gratitude is deeply expressed to my co-supervisor, Dr. Yap Chi Chin from National University of Malaysia, Malaysia for his guidance and opinion in my research study. This research success could not have been achieved without their participation and guidance.

Special appreciation goes to Dr. Yap Chi Chin, Dr. Tan Sin Tee and their team from the School of Applied Physics in Universiti Kebangsaan Malaysia for the beneficial discussion and knowledge sharing. In addition to that, I would also like to show my appreciation for the collaborative simulation work to Dr. Kim Jung-Mu from Division of Electronic Engineering, Jeonbuk National University, Jeonju 54896, Republic of Korea, and Dr. Wu Bao, Dr. Yu Hao, as well as Dr. Wu HengAn from CAS Key Laboratory of Mechanical Behavior and Design of Materials, Department of Modern Mechanics, CAS Center for Excellence in Complex System Mechanics, University of Science and Technology of China, Hefei 230027, China.

Furthermore, I would like to thank all the lab technician and staff from the School of Engineering, Monash University Malaysia for their advice and cooperation throughout the project.

Special thanks goes to Mr. Azaruddin and Mr. Afiq from Nano-Analytical Platform (NAP) for their help with using the characterization equipment. Furthermore, I wish to thank Advanced Engineering Platform (AEP) and Monash University Malaysia for providing the scholarship throughout my studies. I am also thankful for all the discussion with Dr. Chang Wei Sea's research group members.

Lastly, I would like to express my greatest gratitude and appreciation to my parents and siblings for their support throughout the whole Doctor of Philosophy journey in Monash University Malaysia. These accomplishments would not have been possible without them.

Thank you.

***Lim Fang Sheng,***

***2020***

# TABLE OF CONTENT

# ABSTRACT

Noble metal nanostructures have been widely explored as an effective method to increase photon absorption and charge separation in plasmonic application such as photocatalysis and surface enhanced Raman scattering (SERS). In this study, we integrated two different noble metals gold (Au) and silver (Ag) into Au/Ag bimetallic nanoparticles (BNPs) via solid-state thermal dewetting to investigate the room-temperature electrical conductivity, visible light absorption and its effect on photoelectrochemical (PEC) activity. The Au/Ag BNPs give rise to extended visible light absorption range, exhibiting localized surface plasmon resonance (LSPR) effect that lead to strong SERS. X-ray photoelectron spectroscopy shows binding energy shift in Au/Ag BNPs, suggesting electron transfer from Ag to Au where charge transport behavior can be tailored. Kelvin probe force microscopy and conductive atomic force microscopy displayed a significantly enhanced electrical conduction in Au/Ag BNPs due to the lowered Schottky barrier height. When incorporating the Au/Ag BNPs onto ZnO semiconductor photoanode, the photoactivity was improved with lower charge transport resistance compared to monometallic and pristine ZnO. This work delivers a general approach to understand the plasmon-induced charge interaction hence photochemistry of noble metal BNPs/semiconductor photoanode by incorporating a controllable composition ratio which is capable of exploiting the enhanced electrical conduction and LSPR effect for PEC water splitting and SERS.

# List of Illustrations

# List of Tables

# List of Abbreviations

| | |
|---|---|
| Au/Ag BNPs | Gold/silver bimetallic nanoparticles |
| Au NPs | Gold nanoparticles |
| Ag NPs | Silver nanoparticles |
| MNPs | Monometallic nanoparticles |
| BNPs | Bimetallic nanoparticles |
| NPs | Nanoparticles |
| LSPR | Localized surface plasmon resonance |
| SPR | Surface plasmon resonance |
| PEC | Photoelectrochemical |
| SERS | Surface enhanced Raman scattering |
| UV-Vis | Ultraviolet-visible |
| SWS | Solar water-splitting |
| KPFM | Kelvin probe force microscopy |
| CAFM | Conductive atomic force microscopy |
| FESEM | Field-emission scanning electron microscopy |
| XRD | X-ray diffraction |
| TEM | Transmission Emission Microscope |
| STEM | Scanning Transmission Emission Microscope |
| PL | Photoluminescence |
| EDS | Energy dispersive spectroscopy |
| CA | Chronoamperometry |
| LSV | Linear sweep voltammetry |

| | |
|---|---|
| EIS | Electrochemical impedance spectroscopy |
| CPD | Contact potential difference |
| $O_2$ | Oxygen |
| $H_2O$ | Water |
| CPE | Constant phase element |
| HOPG | Highly orientated pyrolytic graphite |
| NHE | Normal hydrogen electrode |

# List of Symbols

| | |
|---|---|
| $C_{Au/Ag}$ | Composition ratio of Au/Ag |
| $\varepsilon'$ | Real part of permittivity |
| $\varepsilon''$ | Imaginary part of permittivity |
| $WF_{tip}$ | Work Function of the cantilever tip |
| $WF_{NPs}$ | Work function of nanoparticles |
| $e$ | Electron constant |
| $I_{SERS}$ | Raman intensity of nanoparticles sample. |
| $I_{Raman}$ | Raman intensity of reference sample. |
| $N_{SERS}$ | Number of Raman active probe molecules on nanoparticles. |
| $N_{Raman}$ | Number of Raman active probe molecules on the reference sample. |
| $n$ | Integer |
| $\lambda$ | X-ray wavelength |
| $d$ | Lattice spacing |
| $\theta$ | Diffraction angle |
| $R_s$ | Sheet resistance |
| $K$ | Geometric factor |
| $V$ | Applied voltage |
| $I$ | Measured current |
| $E_{VB}$ | Valence band |
| $E_{CB}$ | Conductance band |
| $E_F$ | Fermi level |
| $\eta$ | Photoconversion efficiency |
| $I_j$ | Photocurrent density |

| | |
|---|---|
| $V_{rev}$ | Standard state-reversible potential |
| $V_{bias}$ | Applied potential |
| $V_{mea}$ | Potential of working electrode at which photocurrent is measured |
| $V_{voc}$ | Potential of working electrode measured under the same irradiation under open-circuit conditions |
| $P_{light}$ | Incident power density |

# List of Publications

Journals:

1. **Fang Sheng Lim**, Sin Tee Tan, Yuanmin Zhu, Jhih-Wei Chen, Bao Wu, Hao Yu, Jung-Mu Kim, Riski Titian Ginting, Kam Sheng Lau, Chin Hua Chia, HengAn Wu, Meng Gu and Wei Sea Chang (2020) Tunable plasmon-induced charge transport and photon absorption of bimetallic Au-Ag nanoparticles on ZnO photoanode for photoelectrochemical enhancement under visible light. *J Phys Chem C*. [Accepted] (Q1, Impact Factor: 4.309)

Other publication**:**

1. Kok Hong Tan, **Fang Sheng Lim,** Alfred Zhen Yang Toh, Xia-Xi Zheng, Chang Fu Dee, Burhanuddin Yeop Majlis, Siang-Piao Chai, Wei Sea Chang (2018) Tunable spectrum selectivity for multiphoton absorption with enhanced visible light trapping in ZnO nanorods. Small, 14, 1704053. (Q1, Impact Factor: 9.598)
2. Kok Hong Tan, Yun-Wen Chen, Chien Nguyen, Hongliang Wang, Jhih-Wei Chen, **Fang Sheng Lim**, Khian-Hooi Chew, Qian Zhan, Chung-Lin Wu, Siang-Piao Chai, Ying-Hao Chu, Wei Sea Chang (2018) Energy band gap modulation in Nd-doped $BiFeO_3/SrRuO_3$ heteroepitaxy for visible light photoelectrochemical activity. *ACS Applied Materials & Interfaces*, 11, 1, 1655-1664. (Q1, Impact Factor: 8.097)
3. Kam Sheng Lau, Siew Xian Chin, Sin Tee Tan, **Fang Sheng Lim**, Wei Sea Chang, Chi Chin Yap, Mohammad Hafizuddin Hj Jumali, Sarani Zakaria, Soon Wei Chook, Chin Hua Chia (2019) Silver nanowires as flexible transparent electrode: Role of PVP chain length. *Journal of Alloys and Compounds*. 803, 165-171. (Q1, Impact Factor: 4.175)

# Chapter 1 Introduction

## 1.0 Research Overview

In this thesis, the development and application of bimetallic nanoparticles (BNPs) for plasmonic application such as solar water-splitting (SWS) and surface enhanced Raman scattering (SERS) have been undertaken. This thesis covers a total of seven chapters. **Chapter 1** shows the problem statement, scope of research and research objective. **Chapter 2** provides the background theory of the fabrication of metal nanoparticles and their plasmonic phenomena. The fundamentals of Metal oxide-based Semiconductors is discussed, as well as the fundamental of SWS, as well as fundamental of SERS. **Chapter 3** provides the literature review which summarized of the latest studies related to solid-state thermal dewetting, characteristic of metal NPs, as well as SWS and SERS application. **Chapter 4** describes the methodology for the fabrication of Au/Ag BNPs and zinc oxide (ZnO), as well as the characterization methods to study the structural, optical and electrical properties. **Chapter 5** focuses on the results and discussions of studying the Au/Ag BNPs with different composition ratio and their effect on structural, optical and electrical properties. Using this knowledge, SWS and SERS were used as a platform to study the tunable properties of Au/Ag BNPs. Finally, the research conclusion were made and recommendations for the future work were proposed in **Chapter 6** and **Chapter 7**, respectively.

This research demonstrates that the photon absorption, electrical conduction, as well as charge transfer and separation by the BNPs can be effectively tuned by controlling the composition ratio, and thus altering the efficiency in SERS and SWS.

## 1.1 Problem Statement

The problem statement of this thesis is highly motivated by the limitation of SWS and SERS application. In the case of SWS, the PEC performance is hindered by the large band gap of the semiconductor which limit the photon absorption to the UV region and also the fast charge carrier recombination. In the case of SERS, the limited photon absorption by the dye molecules under low concentration hindered the Raman scattering technique from the detecting the vibration of the molecules. Thus, BNPs are being used to explore the possibility to broaden the photon absorption spectrum and supress charge carrier recombination with enhanced electrical conduction. The specific problem statement of the thesis is as listed below.

To date, fabrication of BNPs consisting of Au and Ag are mostly achieved via wet chemistry solution-phase method, however, these methods have certain intrinsic drawbacks such as particle aggregation and colocation, causing poor repeatability and reproducibility [1-3]. To overcome such drawbacks, certain techniques have been explored and developed by introducing self-assembled nanostructures by templated growth [4], and electron-beam lithography [5] to synthesize arrays of bimetallic nanostructures. Despite that, additional chemical modification are still needed for the removal of excess reagents [6], as well as other driving forces such as hydrodynamic interaction and electrostatic [7, 8] for the assembly of bimetallic nanostructures. To overcome the as-stated limitation above, solid-state thermal dewetting method have been employed which involves the deposition of a thin metal film and subsequent thermal annealing to form nanoparticles. Therefore, it is crucial to fully explore the development of Au/Ag BNPs via solid-state thermal dewetting method. Furthermore, previous reports mainly focuses on the integration of MNPs in plasmonic devices, which investigated the effect of size [9-11], shape [12, 13] and material types [14-16] of MNPs on plasmonic activity. However, the understanding of

plasmon-induced charge separation and electrical conduction of BNPs with different composition ratio is still limited.

## 1.2 Scope of Research

The scope of research focuses on the fabrication of Au/Ag BNPs via low temperature solid-state thermal dewetting process and tuning the composition ratio of Au/Ag BNPs to study the structural, optical and electrical properties of BNPs for SWS and SERS detection. The plasmonic device structure consists of FTO as the transparent conductive oxide, Au/g BNPs as the plasmonic nanostructure, ZnO as the metal oxide semiconductor layer. In general, this work can be grouped as followed:

- Phase 1: Fabrication of Au/Ag BNPs on FTO by solid-state thermal dewetting method. (Au/Ag BNPs /FTO)
- Phase 2: SERS measurements using Au/Ag BNPs /FTO.
- Phase 3: Fabrication of ZnO thin film by sol gel spin casting method. (Au/Ag BNPs/ ZnO/ FTO)
- Phase 4: PEC measurements using Au/Ag BNPs/ ZnO/ FTO.

## 1.3 Research Objective

The main objective of this research is the development of Au/Ag BNPs with reproducible tunable composition ratio to understand the plasmon-induced charge separation and electrical conduction in driving photochemistry activity. This involves the investigation of the fundamentals of structural, optical and electrical properties of the BNPs. In order to accomplish this aim, several sub-objectives to be achieved are listed as:

- To design and develop plasmonic NPs and metal oxide semiconductor:
    I. Synthesis of Au NPs and Ag NPs.
    II. Synthesis of Au/Ag BNPs.
    III. Synthesis of ZnO.

- Investigation of the structural properties:
    I. Surface morphology using Field-emission scanning electron microscopy (FESEM).
    II. Crystallographic properties and crystalline orientation using X-ray diffraction (XRD).
    III. Elemental composition and phase distribution using energy dispersive spectroscopy (EDS).
    IV. Molecular dynamic simulation.

- Investigation of the optical properties:
    I. Absorption spectra using Ultraviolet-visible spectroscopy (UV-Vis).
    II. Electromagnetic field simulation.

- Investigation of the electrical properties:
    I. Electron-hole separation and recombination using photoluminescence spectroscopy (PL).
    II. Drift current using conductive atomic force microscope (CAFM).
    III. Surface potential using Kelvin probe force microscopy (KPFM).

- Investigation of the SERS performance:
    I. Enhancement factor and detection limit using Raman spectroscopy.

- Investigation of the PEC performance:
    I. Photocurrent density using chronoamperometry (CA).
    II. Charge transfer using linear sweep voltammetry (LSV).
    III. Resistance using electrochemical impedance spectroscopy (EIS).

# Chapter 2 Background Theory

## 2.1 Fabrication of metallic NPs

In general, plasmonic metallic NPs can be synthesized either via chemical approach or physical vapour method. Recently, wet chemical synthesis methodology has been widely applied for the fabrication of NPs with controlled shapes and sizes [17-21]. Using this approach, complicated structure such as nanorods[18], multipods [22, 23] and core-shell NPs [24-26] can be synthesized. However, due to the nature of wet chemical synthesis, it has resulted in undesirable contamination of the plasmonic devices due to the surfactants used during the fabrication process.

To solve the contamination issue, pulsed laser ablation of a solid target immersed in a liquid medium has been explored [27-29]. This technique is capable of producing a large variety of NPs which are uncontaminated by both surface-active substances and counter ions. As a result, the absence of unwanted reagents such as stabilizers and by-products which are usually generated during wet chemical process are advantageous when NPs are used for application as these reagents might result in morphological changes to the embedded layers in the device. In physical vapour method, conventional deposition methods such as vapor-phase deposition, photo- and nanosphere lithography, and electrodeposition have been widely employed to deposit the thin metallic film. Subsequently, fabrication of metallic NPs can be performed by dewetting of the thin film via atomic diffusion when the activation energy is exceeded by nanosecond pulsed laser annealing [30-36], ion beam [37-39], electron beam [40] and thermal annealing[41-45]. However, the fabrication of metallic NPs on transparent conductive oxide (TCO) electrode through solid-state dewetting method via thermal annealing is emphasized in this report.

The mechanism of solid-state dewetting via thermal annealing will be explained in the following section. Solid-state thermal dewetting process of a thin metallic film deposited on a substrate involves the formation of droplets from a continuous or partially continuous film during atomic diffusion as shown in Figure 1(a) and Figure 1(b), respectively. This process is driven by the total surface free energy minimization of the metallic film. Initially, the dewetting starts by the nucleation of holes in the continuous film which reach the substrate surface. However, in the case whereby the film is not continuous and exists as island structure, the dewetting process will proceed to the growing of the holes over time which will develop a thickened rim at the edges due to the mass-conservation and local curvature gradient at their edges [45]. Subsequently, the rim increases its thickness with time which resulted in the reduction of its net curvature and also its edge retraction velocity. After that, the rims break apart by a fingering instability as the corners of the hole growing become thermodynamically unstable with the consequent formation of material lines that decays into droplets through a Rayleigh-like instability [46]. Generally, metal-metal interface has a stronger bonding compared to metal- non-metal interface [47, 48]. Hence, metallic thin films deposited on non-metal substrate are thermodynamically unstable at elevated temperature, which resulted in the initiation of dewetting process below the melting temperature of the metal upon thermal annealing. The energy required to initiate the dewetting process of the metallic film via the activation of atomic diffusion can be transferred to the film by standard thermal annealing. The complete transformation of the metallic film into nanoparticles (NPs) and their properties depends on factors such as annealing temperature, initial film thickness, type of metallic film and the properties of the underlying substrate. Generally, dewetting process of different metallic films with the same film thickness requires low annealing temperature for metals with high thermal conductivity, and for a particular metallic film, the annealing temperature

increases with the film thickness for dewetting to occur [49]. Araújo et al. demonstrated that parasitic absorption of Ag nanostructures can be reduced by using an underlying substrate with high conductivity ($\sigma = 59.5$ S cm$^{-1}$) and low roughness (approximately 1 nm) [50]. In other works, Ruffino et al. displayed that Ag nanoparticles on ITO have larger diameters compared to Au NPs with the same initial film thickness of 5nm and similar applied energy [34]. In addition to that, Ruffino et al. also demonstrated that the diameter of the nanoparticles with initial film thickness over a certain threshold is dependent on the substrate morphology [51]. It was reported that initial film thickness above the root mean square of the textured substrate will result in bimodal nanoparticle diameter distribution.

Besides MNPs, BNPs can be fabricated by solid-state thermal dewetting via deposition of bilayer metallic films. However, the shape uniformity and nanoparticles diameter distribution of the BNPs are highly dependent on the individual layer thickness, stacking sequence of the bilayer, material properties, annealing temperature and annealing atmosphere. For instance, Herz et al. reported that tungsten (W) layer functioned as a passivation layer for gold (Au) during the formation of Au-W bimetallic nanoparticles [52]. Furthermore, Seo et al. reported that the bimetallic Pt-Ni nanoparticles composition can be effectively controlled by the thickness ratio of the deposited Pt-Ni bilayer films [53]. As a result, it is crucial to optimize parameters such as annealing temperature, initial individual film thickness and stacking sequence of the bilayer film of the metallic films to obtain the desired nanostructures.

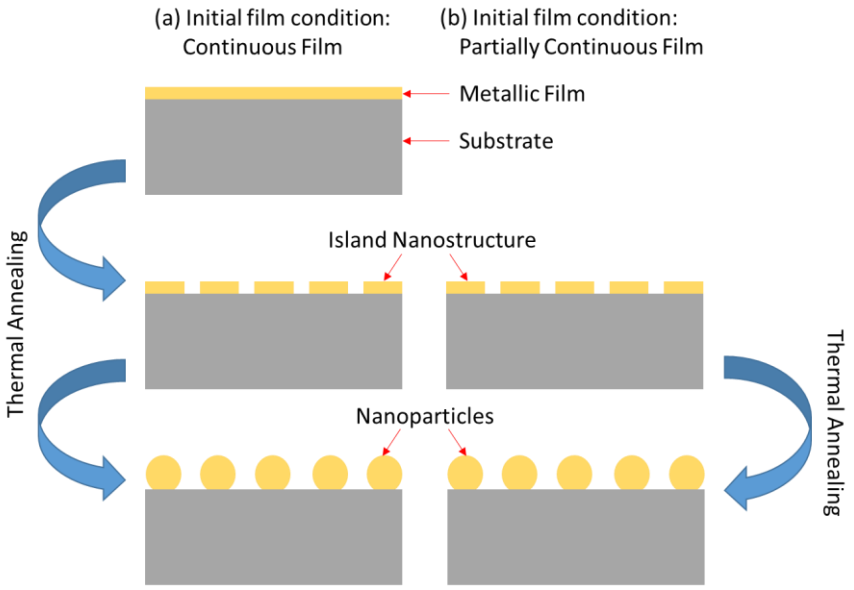


**Figure 1.** Solid state dewetting via thermal annealing of metallic nanoparticles. (a) Initial film condition is continuous and (b) Initial film condition is partially continuous.

## 2.2 Fundamental of Plasmonic Phenomena

Plasmonic enhancement by metal nanoparticles (NPs) in plasmonic applications can be attained via mechanisms such as localized surface plasmon resonance (LSPR), light scattering or hot electron injection.

In the case of light scattering (Figure 2(a)), metal NPs function as sub-wavelength scattering nanostructures that trap and redirect the incident photon into the semiconductor layer, thereby increasing the photon propagation path length within the layer. At the region of heterogeneous interface, metal NPs will preferentially scatter light into the medium with high permittivity. During the scattering process, enhancement of the photon absorption efficiency is achieved by light being scattered with specific angular spreads, which improves the optical

propagation pathway via multi-photon scattering. Subsequently, this allows more photons to pass through the semiconductor layer during the light scattering process. As a result, enhancement of plasmonic devices via light scattering involved increasing the light propagation pathway in the semiconductor layer to improve the absorption efficiency.

. On the other hand, in the case of LSPR (Figure 2(b)), metal NPs function as sub-wavelength antennas which focuses the photon of specific wavelength in the spectrum on the surface of NPs. This results in the improvement of the electromagnetic (EM) field upon photon irradiation, hence facilitates photon absorption of the semiconductor layer. Metal NPs is capable of absorbing and concentrating light at its surrounding via LSRP. This mechanisms involves MNPs located within the vicinity of the semiconductor layer (in contact or not in contact with the semiconductor material). LSPR phenomena are initiated when the frequency of the incident photon matches with the frequency of the oscillation excited electron of metal NPs. As a result of the resonance effect, the enhancement of the electromagnetic field leads to the effective photon concentration of the visible to infrared region surrounding the metal NPs.

For the case of hot electron injection (Figure 2(c)), excited electrons in the metal NPs due to the surface plasmon resonance are injected into the conduction band of the semiconductor, resulting in efficient charge transfer and separation. In this mechanism, the metal NPs function as a sensitizer, which absorb the incident photons and, subsequently, transfer the excited electrons from the plasmon band of the metal to the conduction band of the semiconductor. It is important to note that the hot electron injection mechanism is only possible if the energy of the electrons are sufficiently high to move across the Schottky barrier formed between the metal and semiconductor heterojunction. Similar to LSPR and light scattering, the hot electron injection mechanisms also depends on the nanostructure characteristic such as metal type, size, shape and nature of the metal-

semiconductor heterojunction. The metal type, shapes, sizes and location of integration of metal NPs will significantly affect the enhancement mechanisms.

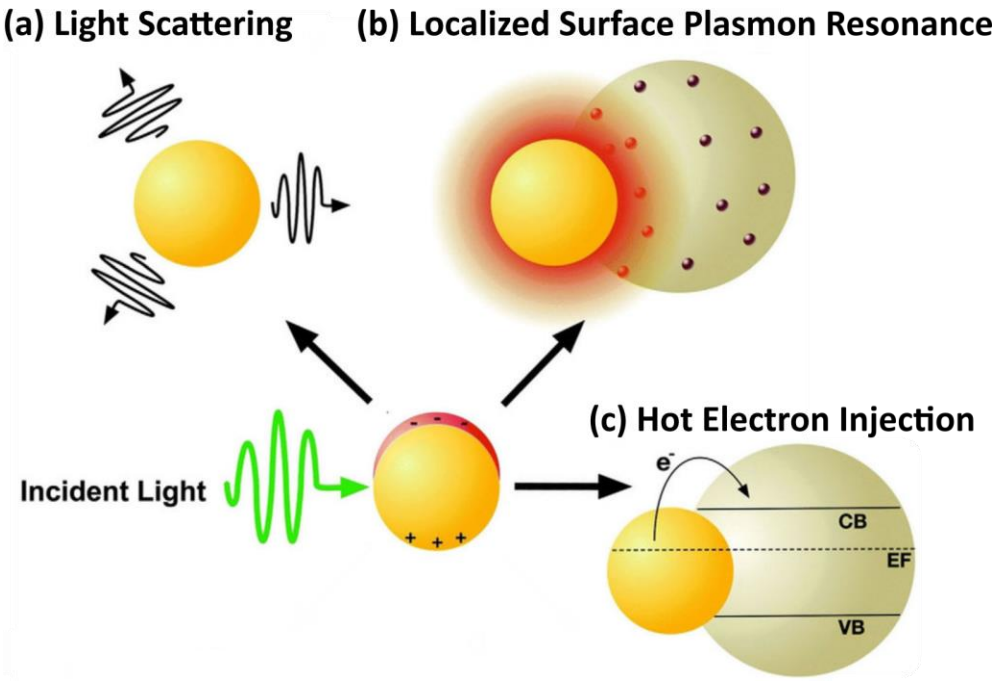


**Figure 2.** Schematic diagram for plasmonic phenomena: (a) Light scattering, (b) Localized surface plasmon resonance, and (c) Hot electron injection.

## 2.3 Metal oxide-based Semiconductors

In general, metal oxide based photo-anodes semiconductor are considered to be stable in harsh liquid medium. Among the many metal oxides, materials such as ZnO [54, 55], $TiO_2$ [56-58], $WO_3$ [59-61], and $Fe_2O_3$ [62-65] are widely utilized in SWS research due to their chemical stability and low cost. For instance, ZnO and $TiO_2$ has the capability to perform unassisted water electrolysis reaction under solar illumination. However, the PEC performance of these photo-anodes are relatively low because of their large band gap and limited absorption range in the UV region (5% of total solar spectrum) as shown in Figure 3. In order to overcome these obstacles,

several strategies such as nanostructure surface design [66-68], doping [69-71] and heterojunction modification [72-74] have been applied to enhance the plasmonic performance. To date, plasmonic applications with the aid of noble metal nanostructures has gained much attention due to the effectiveness of these metal nanostructures and semiconductor heterojunction formation in improving photon absorption and supress charge recombination [75-79].

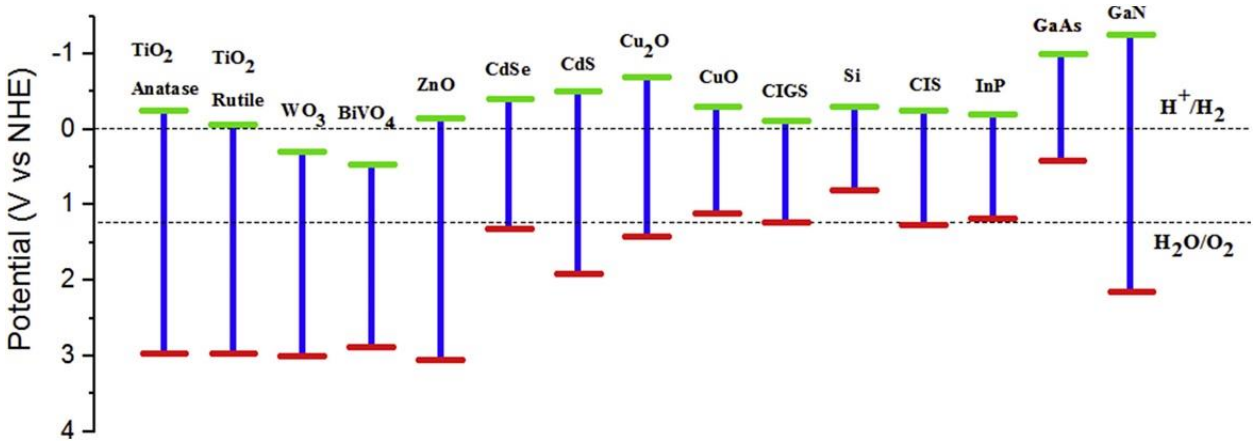


**Figure 3.** Band edge potentials of metal oxide semiconductors (interfaced with a pH 0 electrolyte solution). [80]

## 2.4 Fundamental of Solar Water Splitting (SWS)

Photoelectrochemical (PEC) water-splitting has been widely explored as a viable solar-to-chemical pathway by oxidizing/reducing $H_2O$ molecules with electron-hole pairs using a semiconductor. The configuration of a typical PEC device encompasses of a semiconductor photoelectrode layer whereby electron-hole pairs are created upon photon absorption. Upon charge carrier generation and separation, the electrons are transferred to the counter electrode to reduce the water molecules to hydrogen, while the holes at the valence band of the semiconductor will oxidize the water molecules to oxygen.

The requirement of an ideal semiconductor photo-anode used for solar water splitting (SWS) is as followed: (i) suitable band gap of > 1.23 eV + 0.8 eV to pass the kinetic barriers; (ii) conduction band located above the $H^+/H_2$ equilibrium potential for $H_2$ evolution and valence band below the $O_2/H_2O$ equilibrium potential for $O_2$ evolution (Figure 4); and (iii) photo-corrosion stability in electrolyte [81]. Ideally, the photo-generated charge carrier transfer to the respective electrode and liquid junction without recombination, however, charge recombination tend to occur during the electron transfer process which resulted in deterioration in PEC performance [82]. Therefore, the band gap of semiconductor used to drive the SWS process should have values in the range of 1.6 to 2.2 eV [83]. Furthermore, the semiconductor should have a low cost and photo-corrosion stable.

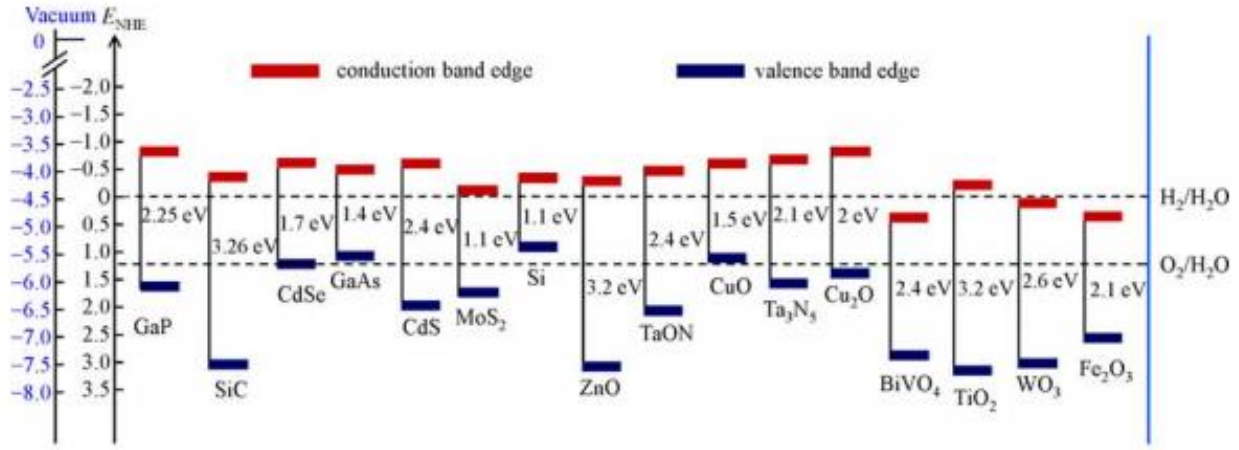


**Figure 4.** Schematic diagram of band edge positions of semiconductors relative to vacuum and normal hydrogen electrode (NHE) level. [84]

Solar water splitting (SWS) uses photons to create a chemical reaction, in particular, the splitting of water molecules into hydrogen gas ($H_2$) and oxygen gas ($O_2$). The SWS cells commonly

consists of an anode and cathode electrode submerged in an electrolyte solution and connected by external circuit. One of the two electrodes is a photon absorbing semiconductor layer and another electrode is commonly a metal, such as platinum (Pt) as shown in Figure 5. When the semiconductor is excited by photons with energy larger than the band gap of the semiconductor, electrons are excited from the valance band (VB) to the conduction band (CB) of the semiconductor, thus creating an electron-hole pairs. Next, the photo-generated charge carrier will either undergo recombination process or be separated by the electric field exist in the space-charge between the semiconductor- electrolyte interface. At the working electrode (anode)'s semiconductor surface, the photo-generated holes separate the $H_2O$ molecules into $O_2$ and $H^+$ (oxygen evolution reaction) as shown in the following Equation 1:

$$2H_2O + 4h^+ \rightarrow O_2 + 4H^+ \qquad \text{Equation 1}$$

Next, the photo-generated electrons are transferred to the cathode (counter electrode) via the external circuit, while the hydrogen ions move to the cathode via the electrolyte. Protons are then reduced at the cathode to generate gaseous $H_2$ (hydrogen evolution reaction) as shown in the following Equation 2:

$$4H^+ + 4e^- \rightarrow 2H_2 \qquad \text{Equation 2}$$

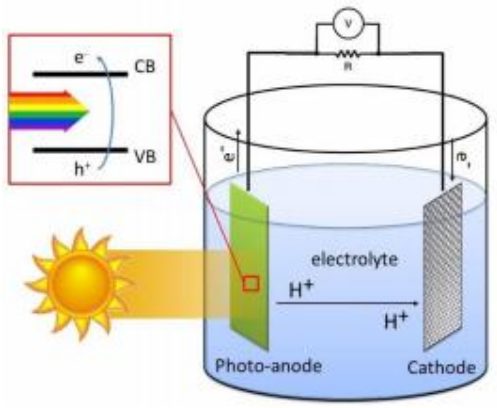


**Figure 5.** Diagram of solar water splitting device that encompasses the semiconductor photo-anode and metal cathode.

## 2.5 Fundamental of Surface Enhanced Raman Scattering (SERS)

Surface enhanced Raman scattering (SERS) has been widely utilized as a detection method to identify and quantify ultra-low concentration of chemical/bio- molecules in numerous fields such as environmental science and medical diagnostic [85-87]. Among the other molecule identification methods, SERS is considered as among the most sensitive, reliable and selective method for non-destructive analysis via harnessing the electromagnetic field of plasmonic nanostructures [88-90].

Raman scattering indicates the inelastic scattering phenomena that happen when photon interacts with a molecules. The characterization of the molecule frequency shift due to Raman scattering is a method called Raman spectroscopy, which provides molecular identification via vibrational modes. However, certain molecules are weakly responsive to the photons during excitation, thus surface enhanced Raman scattering (SERS) is utilized to improve the photon absorption of the target molecules. SERS consists of a nanostructured metal surfaces whereby the

Raman signal of the desired molecule to be analysed is enhanced due to the plasmonic effect as shown in Figure 6. SERS enhancement originate from two possible mechanisms, namely, electromagnetic enhancement and chemical enhancement. The chemical enhancement is mainly due to the charge transfer reactions with chemisorbed species that are not plasmonic but give a Raman signal enhancement. Thus, this report focuses on the electromagnetic enhancement which originate from the electric field created by the LSPR acting on the desired target molecules.

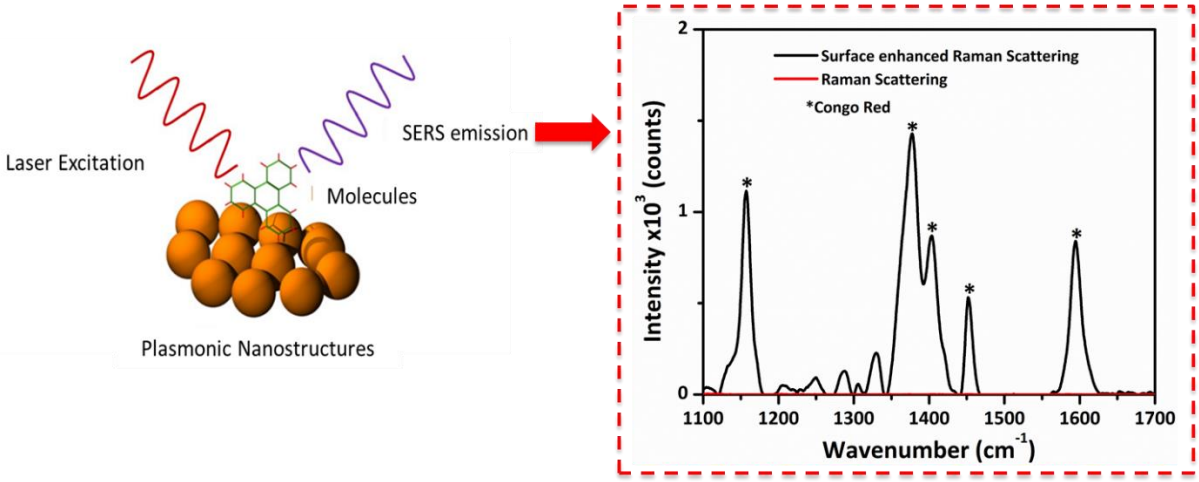


**Figure 6.** Schematic drawing of SERS with the corresponding SERS signal.

# Chapter 3 Literature Review

## 3.1 Solid-state Thermal Dewetting of metal NPs

The solid-state thermal dewetting process is highly dependent of the type of materials, bottom layer material, annealing temperature and annealing duration. As the rate of diffusion is high, the required annealing temperature is lower. For instance, Ag has a higher rate of diffusion than Au, thus the required annealing temperature for complete formation of nanoparticles will be lower for Ag as compared to Au [91]. Table 1 and Table 2 summarize the latest studies on the solid-state thermal dewetting for MNPs and BNPs, respectively.

**Table 1.** Solid-state thermal dewetting parameters of MNPs.

| Materials | Bottom layer Material | Coating Method | Coating Condition | Annealing Temperature | Annealing Duration | Ref. |
|---|---|---|---|---|---|---|
| Ni | $TiO_2$ nanotube array | Sputtering | 16 mA $10^{-2}$ mBar | 450 $^oC$ | 1 hour | [92] |
| Cu | $TiO_2$ nanotube array | Sputtering | 16 mA $10^{-2}$ mBar | 450 $^oC$ | 1 hour | [92] |
| Pt | Sapphire | Pulsed Laser Deposition | $1x10^{-4}$ Torr | 500 to 900 $^oC$ | 120 s | [93] |
| Au | $TiO_2$ film | Thermal Evaporation | $2x10^{-5}$ mBar | 500 $^oC$ | 2 hours | [94] |
| Au | Antimony | Ion Beam Coater | n/a | 900 $^oC$ | 15 minutes | [91] |
| Ag | Antimony | Ion Beam Coater | n/a | 750 $^oC$ | 30 minutes | [91] |
| Ag | $SiO_2$ | Thermal Evaporation | $10^{-3}$ Pa | 200 $^oC$ | 1 hour | [95] |

**Table 2.** Solid-state thermal dewetting parameters of BNPs.

| Materials | Bottom layer Material | Coating Method | Coating Condition | Annealing Temperature | Annealing Duration | Ref. |
|---|---|---|---|---|---|---|
| Ni/Cu | $TiO_2$ nanotube array | Sputtering | 16 mA $10^{-2}$ mBar | 450 $^oC$ | 1 hour | [92] |
| Ag/Pt | Sapphire | Pulsed Laser Deposition | $1x10^{-4}$ Torr | 500 to 900 $^oC$ | 120 s | [93] |
| Ag/Pd | Sapphire | Sputtering | 3mA $1x10^{-1}$ Torr | 400 to 800 $^oC$ | 120 s | [96] |
| Au/Ag | Glass | Co-sputtering | n/a | 500 $^oC$ | 1 hour | [97] |
| Ag/Au | Quartz | Thermal Evaporation | $1x10^{-5}$ Torr | 700 $^oC$ | 1 hour | [98] |
| In/Pt | Sapphire | Sputter | $1x10^{-1}$ Torr | 550 to 900 $^oC$ | 450 s | [99] |

## 3.2 Characteristic of metal NPs

The material, shapes, sizes and location of metal NPs will significantly affect the enhancement mechanisms of the plasmonic devices. The plasmonic performance (SWS and SERS) can be enhanced either by LSPR, light scattering, or hot electron injection, which is dependent on the characteristic of the metal NPs.

### 3.2.1 Effect of metal NPs Material Properties

Based on the desired plasmonic enhancement mechanism, plasmonic materials with the appropriate optical properties are selected. For plasmonic applications, plasmonic metals that are commonly integrated into the devices are gold (Au), silver (Ag), copper (Cu) and aluminium (Al). The absorption spectra of Au and Cu falls within the visible spectrum, whereas Ag and Al corresponds to absorption spectra within the ultraviolet region [100, 101]. The strategy for deciding the suitable material is to compare the real ($\varepsilon'$) and the imaginary ($\varepsilon''$) component of the

permittivity property. The spectra range of the surface plasmon resonance can be estimated using the crossover wavelength ($\lambda$ where $\varepsilon'$ becomes negative). Thus, a larger negative $\varepsilon'$ should exhibits an enhancement of the electromagnetic near field with a larger absorption cross-section. In contrast, $\varepsilon''$ indicates the optical losses, hence, a higher $\varepsilon''$ exhibits a weaker SPR and a more dissipative decay for heat generation. Based on the permittivity properties ($\varepsilon'$ and $\varepsilon''$), Ag displays the best balance between high negative $\varepsilon'$ and very low $\varepsilon''$, which indicates low losses over the whole spectra range [102]. Au and Cu have the second-best optical properties with a high negative $\varepsilon'$ and relatively low $\varepsilon''$, although displaying higher losses than Ag in the spectra range between 300 to 600 nm due to interband transition [103]. Lastly, Al has the relatively high negative $\varepsilon'$ and displaying the highest optical losses due to the intense interband transitions strongly damping the metallic properties [104].

### 3.2.2 Effect of metal nanostructures Shape

The effect of NPs shape on the surface plasmon resonance and light scattering was widely reported by numerous researchers. For instance, Au nanorods exhibit more efficient PEC performance compared to Au nanosphere due to the enhanced electron transfer pathway and also increased photon absorption [105]. In terms of SERS, Ag nanocubes with sharp corners exhibited enhanced SERS efficiency compared to truncated Ag nanocubes due to their enhanced electromagnetic field (EMF) via LSPR [106]. This is mainly because of the concentrated EMF generated at the sharp corners, while the EMF is spread uniformly over the spherical NPs [107]. The SPR wavelength of gold nanospheres (Au NSs) shows single peak at 540nm, whereas gold nanorods (Au NRs) are having two peaks at 780nm and 540nm due to the longitudinal and transverse mode of LSPR, respectively. Furthermore, Kozanoglu et al. investigated the effect of

different Au nanostructures such as Au nanostars (NSts), Au NRs, and Au NSs on plasmonic performance [12]. Among the different Au nanostructures, Au NSts displayed the highest plasmonic efficiency due to the broaden absorbance spectra, which resulted in the highest light scattering and LSPR effect at the tips of the Au NSts, thereby increasing the plasmonic effects for a wider range of wavelengths. Figure 7 displayed the absorbance spectra of Au (a) NSts, (b) NRs, and (c) NSs. In conclusion, the shape of nanostructures plays a significant role in affecting the plasmonic enhancement.

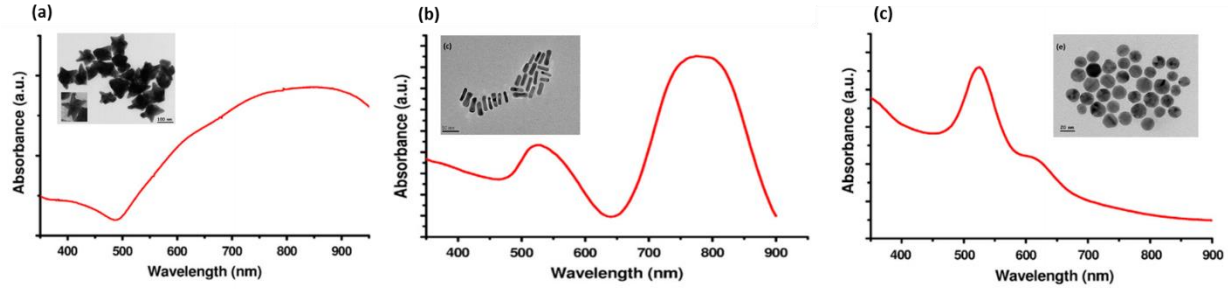


**Figure 7.** Absorbance spectra of Au NPs: (a) Au NSts, (b) Au NRs, and Au NSs. Inset shows the FESEM images of the nanostructures [12].

### 3.2.3 Effect of metal NPs Size

As metal NPs can exhibit enhancement mechanisms of both light scattering and LSPR, as well as hot electron injection, the size of the NPs will determine the contribution of each phenomena. For NPs with size of 50 nm or less, LSPR is the more dominant enhancement mechanism, whereas large NPs with size above or equal to 50nm, light scattering will be more dominant [108]. For instance, Ag nanocubes with increased size (90 to 100 nm) exhibit enhanced SERS enhancement factor [106]. In addition to that, Zhang et al. determined that scattering effect was predominant for Au NPs with diameter larger than 60 nm, while LSPR mechanism for smaller

Au NPs of less than 40 nm [109]. For instance, it was reported that small metal NPs (1 – 4 nm) with distinct corners are preferable in hot electron injection [110, 111]. As the plasmonic mechanisms depends on the NPs size, it is crucial to optimize the NPs size to obtain the desired enhancement mechanisms in plasmonic applications.

### 3.2.4 Location of metal NPs in Semiconductor

Plasmonic effects depending on NPs characteristics such as material, shapes, and sizes have been widely investigated within plasmonic device architecture. Furthermore, another crucial consideration is the integration location of NPs in plasmonic devices, whereby it can be categorized into two major classes: (i) NPs in contact with semiconductor layer, (ii) NPs not in contact with semiconductor layer. However, this thesis will be focusing on NPs in contact with the semiconductor layer. Identification of these classes are essential as they are fundamentally different from each other in terms of performance enhancement mechanism. For instance, metal NPs not in contact with semiconductor is unable to experience hot electron injection enhancement mechanism because photo-excited electrons in the NPs is unable to freely move across to the semiconductor. In this case, LSPR and light scattering are the possible mechanism for NPs not in contact with semiconductors. Therefore, careful design and considerations must be taken to harness the desired enhancement mechanism in the plasmonic device.

In summary, plasmonic performance of applications such as solar water-splitting (SWS) and surface enhanced Raman scattering (SERS) are highly dependent on NPs characteristics such as material, shapes, sizes and location have been widely investigated. Past researches on SWS and SERS applications are compiled as shown in the tables below.

## 3.3 Solar Water-Splitting (SWS)

Integration of plasmonic nanostructures on semiconductor in SWS resulted in performance improvement by enhancement mechanism such as LSPR, light scattering or hot electron injection [112]. Thus, it is crucial to identify the enhancement mechanisms by plasmonic nanostructures for SWS as shown in Table 3. In addition to that, it can be observed that NPs, especially BNPs are typically synthesized via wet chemistry method, thus it is of great interest to explore solid-state methods such as solid-state thermal dewetting.

**Table 3.** Summary of solar water-splitting (SWS).

| Structure | NPs preparation | Enhancement mechanisms | Ref |
|---|---|---|---|
| AuPd/Graphene- ZnO NRs | Wet chemistry (alloyed) | Hot electron injection | [113] |
| Cu- $TiO_2$ nanotube | Wet chemistry | LSPR | [114] |
| Au- ZnO NWs | Wet chemistry | Hot electron injection and LSPR | [115] |
| Au- ZnO/CdS nanotube | Wet chemistry | LSPR and hot electron injection | [116] |
| AuNPs / $Al_2O_3$/ ZnO NRs | Wet chemistry | LSPR and hot electron injection | [117] |
| AuAg – $TiO_2$ NRs | Wet chemistry (alloyed) | Hot electron injection | [118] |
| AuAg – $TiO_2$ NRs | Wet chemistry (core-shell) | LSPR, light scattering and multipolar resonance | [119] |
| AuAg- ZnO NRs | Wet chemistry (alloyed) | Hot electron injection | [120] |
| AuPd – $TiO_2$ NRs | Wet chemistry (alloyed) | LSPR and hot electron injection | [121] |

| | | | |
|---|---|---|---|
| AuPd – $TiO_2$ NRs | Sputtering (alloyed) | Hot electron injection | [122] |
| Au – $TiO_2$ thin films | Thermal dewetting | Hot electron injection | [123] |

## 3.4 Surface Enhanced Raman Scattering (SERS) detection

Utilization of plasmonic nanostructures in SERS detection resulted in performance improvement by enhancement mechanism such as LSPR and light scattering. The performance of SERS is often expressed in terms of enhancement factor (EF), which indicates the ratio of intensity factor detected by the Raman probes using plasmonic nanostructures against the reference substrate without the nanostructures. Table 4 summarizes the enhancement factors of MNPs and BNPs, which indicates that the EF are generally higher for BNPs as compared to MNPs. This can be attributed to the enhanced photon absorption by the BNPs which broadened the absorption wavelength spectrum of the Raman probe molecules.

**Table 4.** Summary of surface enhanced Raman scattering (SERS)

| Plasmonic Nanostructures | NPs preparation | Target molecule | Enhancement factor | Ref |
|---|---|---|---|---|
| Au nanoparticles | Wet chemistry | Methylene blue | $4.0 \times 10^4$ | [124] |
| Ag nanocubes | Wet chemistry | 1,4- benzendithiol | $3.6 \times 10^5$ | [106] |
| Au/Ag nanoparticles | Wet chemistry | Thiabendazole | $3.1 \times 10^6$ | [125] |
| Au nanoparticles | Wet chemistry | 2-naphthalenethiol | $2.0 \times 10^5$ | [126] |
| Au core – Ag shell nanoparticles | Wet chemistry | 4-nitrophenylthiophenol | $3.4 \times 10^6$ | [127] |
| Au-Ag nanoparticles | Wet chemistry | Rhodamine 6G | $1.0 \times 10^8$ | [128] |

| | | | | |
|---|---|---|---|---|
| Au nanorods | Wet chemistry | 4-MPy-BMP | $5.6 \times 10^7$ | [129] |
| Ag nanoparticles | Wet chemistry | 4-NTP | $2.0 \times 10^6$ | [130] |
| Ni/Au core-shell nanoparticles | Laser ablation | Rhodamine 6G | $2.5 \times 10^6$ | [131] |
| Ag/ZnO | Laser Ablation | Ammonium nitrate | N/A | [132] |
| Ag/Cu nanoparticles | Magnetron sputtering | Crystal violet | $3.0 \times 10^5$ | [133] |
| Au nanoparticles | Thermal evaporation | Rhodamine 6G | $1.5 \times 10^6$ | [134] |

# Chapter 4 Methodology

## 4.1 Fabrication of Metallic Nanoparticles

### 4.1.1 Substrate Cleaning

FTO substrates (13 Ohm/sq) were purchased from Sigma Aldrich. FTO substrate were cut to dimensions of 1 $cm^2$ and cleaned prior to deposition by rubbing the top and bottom surface with Acetone using a cotton bud. Each FTO was placed in a glass jar and separated using Teflon substrate holder. The substrates were sonicated using Acetone for 15 minutes, then the Acetone was replaced with iso-propanol (IPA) and sonicated for another 15 minutes. The substrates were then dried on a hot plate at 110 $^oC$ for 10 minutes, followed by ultraviolet-ozone (UV-ozone) cleaning for 10 minutes to remove any organic contaminants.

### 4.1.2 Fabrication of Au NPs and Ag NPs on FTO

High purity (99.99%) Au and Ag metal target with diameter of 57 mm was purchased from Quorum Technologies. Au NPs and Ag NPs on FTO substrate (1 cm x 1 cm) were prepared from thin Au and Ag films, respectively, by solid-state dewetting. In order to etch the surface of the metal target to avoid contaminants and metal oxides from depositing on the sample, the sputter machine was set to sputter for 30 s without any samples inside of the chamber. Deposition of films with total film thickness of 10 nm were performed using Quorum DC rotary sputter machine. The sputter coater parameters for Au and Ag films were utilized as shown in Table 5. The film thickness calibration of Au and Ag was performed using AFM thickness measurement as shown in Figure S1.

**Table 5**. DC sputtering parameters for Au NPs and Ag NPs.

| Parameters | Au | Ag |
|---|---|---|
| Target diameter | 57 mm | 57 mm |
| Sputter time | 35 s (10 nm) | 14 s (10 nm) |
| Sputter current | 25 mA | 50 mA |
| Tooling factor | 1.10 | 1.00 |
| Distance from metal target | 4.6 cm | 4.6 cm |

4.1.3 Fabrication of Au/Ag BNPs on FTO

Au/Ag BNPs were prepared from thin Au and Ag bilayer films by solid-state dewetting. Deposition of combination of 10 nm total film thickness between Au and Ag bilayer films on FTO substrate were performed using Quorum DC rotary sputter machine. During the deposition process, Au film was first sputtered on FTO, followed by a layer of Ag film. The sputter coater parameters for Au and Ag films were utilized as shown in Table 6. In order to investigate the effect of different Ag content in bimetallic NPs, different ratio of Au and Ag bilayer film thickness was sputtered on FTO substrate and tabulated in Table 7.

**Table 6.** DC sputtering parameters for Au/Ag BNPs.

| Parameters | Au | Ag |
|---|---|---|
| Target diameter | 57 mm | 57 mm |
| Sputter time | 17 s (5 nm)<br>14 s (4 nm)<br>11 s (3 nm)<br>7 s (2 nm) | 7 s (5 nm)<br>8 s (6 nm)<br>9 s (7 nm)<br>10 s (8 nm) |
| Sputter current | 25 mA | 50 mA |
| Tooling factor | 1.10 | 1.00 |
| Distance from metal target | 4.6 cm | 4.6 cm |

**Table 7.** Au and Ag ratio for bimetallic nanoparticles.

| Ratio ($Au_X Ag_Y$) | Au/Ag ratio | Au (nm) | Ag (nm) |
|---|---|---|---|
| $Au_{0.4} Ag_{0.6}$ | 0.67 | 4 | 6 |
| $Au_{0.3} Ag_{0.7}$ | 0.43 | 3 | 7 |
| $Au_{0.2} Ag_{0.8}$ | 0.25 | 2 | 8 |

The samples were then placed in the furnace for the annealing process from Au/Ag bilayer films into Au/Ag BNPs as shown in Figure 8. The annealing temperature and holding time were fixed at 300 ºC and 10 minutes, respectively. The heating ramping rate was fixed at 3ºC per minute.

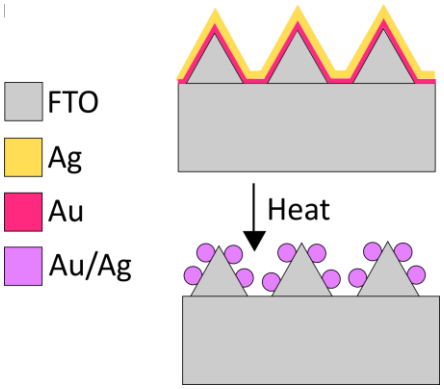


**Figure 8.** Schematic illustration of facile fabrication of Au/Ag BNPs via successive thin film sputtering and thermal dewetting.

4.1.4 Fabrication of Zinc Oxide Thin Film

ZnO uniform thin films were synthesized and homogeneously distributed on the FTO substrate using sol-gel spin coating process. Specifically, ZnO sol-gel precursor was synthesized by mixing 0.2 M of zinc acetate dehydrate (Sigma Aldrich, > 99%) into a solvent of 8 mL ethanol (Sigma Aldrich, > 99%) and, subsequently, 154 µL of diethanolamine (Sigma Aldrich) was added

into the mixture under a constant stirring of 600 rpm at temperature of 60 ℃ for 30 min. Next, the solution was sealed and kept inside the dry cabinet for the aging process (24 h). For the ZnO spin coating step, 25 μL of ZnO sol-gel was spin-coated onto the FTO substrate at a speed of 3000 rpm for 30 s. Lastly, the spin coated samples were annealed in a furnace at a temperature of 300 $^{o}$C for 60 minutes using a ramping time of 30 minutes to improve the crystallinity of ZnO.

## 4.2 Material Characterization

| Characterization Equipment (methods) | Function |
|---|---|
| Bruker Multimode 8 Atomic force microscopy (Scan-Asyst Air) | Perform surface roughness and topography imaging |
| Bruker Multimode 8 Atomic force microscopy (PeakForce Kelvin Probe Force Microscopy- PF KPFM) | Perform nanoscale surface potential mapping of nanoparticles |
| Bruker Multimode 8 Atomic force microscopy (PeakForce Tunneling Atomic Force Microscopy-PF TUNA) | Perform nanoscale current mapping and IV spectroscopy of nanoparticles. |
| Keithley sourcemeter (2 point probe bulk IV testing) | Perform macroscale IV spectroscopy of nanoparticles. |
| Tecnai G20 Transmission electron microscopy (HRTEM and STEM-EDS) | Measure lattice parameter and element mapping analysis of nanoparticles. |
| Bruker D8 Discover X-ray diffractometer<br>X-ray diffraction (XRD) | Determine the crystallographic orientation. |

| | |
|---|---|
| Hitachi Field-emission scanning electron microscopy (FESEM) | Perform morphology imaging of semiconductor and metallic nanoparticles |
| Agilent ultraviolet-visible spectrophotometer (UV-Vis spectroscopy) | Determine the absorption spectra of semiconductor and metallic nanoparticles |
| Horiba Scientific LabRAM HR Photoluminescence spectrophotometer (PL spectroscopy) | Determine the electron-hole pair recombination |
| Horiba Scientific LabRAM HR Raman spectrophotometer (Raman spectroscopy) | Determine the surface enhanced Raman scattering (SERS) performance |
| Gamry Potentiostat (three electrode measurement) | Determine the photoelectrochemical (PEC) performance |

4.2.1 Surface Roughness Mapping

Surface roughness characterization under Scan Asyst Air mode was performed using Bruker Multimode 8 atomic force microscopy (AFM) under ambient atmosphere with relative humidity of less than 40%. Bruker tip (Scan Asyst Air) is made up of silicon (Si) tips of 2.5-8 μm tip height with resonant frequency of 45 kHz and spring constant of 0.2 $Nm^{-1}$. For consistency, all images of the monometallic nanoparticles (MNPs) and bimetallic nanoparticles (BNPs) in a particular series were measured using the same cantilever tip. It is important to note that the nominal tip radius of the cantilever tip is 2 nm and it might increase to a maximum value of 12 nm due to the rounding effect after multiple usage, which might affect the resolution of the topography. For surface roughness mapping, the parameters used are listed in Table 8.

**Table 8.** AFM parameters for surface roughness mapping under Scan-Asyst Air mode.

| AFM parameters | Value |
|---|---|
| Scan size | 1 μm |
| Scan rate | 0.5 Hz |
| Gain | 5 |
| Setpoint | 0.05 V |

4.2.2 Surface Potential Mapping

Surface potential characterization under PF KPFM mode was performed using Bruker Multimode 8 atomic force microscopy (AFM) under ambient atmosphere with relative humidity of less than 40%. Bruker conductive tip (PFQNE-AL) is made up of highly-doped silicon (Si) tips of 2.5-8 μm tip height with resonant frequency of 300 kHz and spring constant of 0.8 $Nm^{-1}$. PFQNE-AL were utilized for all KPFM measurements. Conventional Pt/Ir coated silicon tips were not utilized because of the potential wear off of the conductive coating upon multiple scanning, which will affect the accuracy of the contact potential difference (CPD) due to the changed tip work function. In our case, wearing off will not be an issue as the tip is made up of highly-doped Si. As the tip is made up of a single material, the tip work function will not significantly change upon multiple scanning. In order to determine the work function of the tip, the surface potential of the tip was calibrated with standard samples such as Au-Si-Al and highly orientated pyrolytic graphite (HOPG) as shown in Figure S2 . HOPG was selected due to its stable work function of 4.6 eV under ambient condition. As the CPD between the cantilever tip and HOPG sample is zero, hence the surface potential of the cantilever tip is estimated to be 4.6 eV. For consistency, all images of the MNPs and BNPs in a particular series were measured using the same cantilever tip. It is important to note that the nominal tip radius of the PFQNE-AL is 5 nm and it might increase to a maximum value of 12 nm due to the rounding effect after multiple usage, which might affect the resolution of the topography and surface potential results. Both topography and Kelvin imaging were performed by a two pass (trace and retrace) technique, whereby a single line will be scanned

two times. In the first scan, the topographical information was obtained via Bruker propriety PeakForce Tapping mode (non-contact). After the topography data were stored, the tip will be lifted up to a height based on the value of the lift scan height and the Kelvin probe signals were stored in the second scan. The lift scan height is approximately 30 nm higher than the highest morphology of the scanned area. For consistency, the lift scan height was set to 100 nm for all KPFM measurements. For surface potential mapping, the parameters used are listed in

Table **9**.

**Table 9.** AFM parameters for surface potential mapping under PF KPFM mode.

| AFM parameters | Value |
|---|---|
| Scan size | 1 μm |
| Scan rate | 0.5 Hz |
| Gain | 5 |
| Setpoint | 0.05 V |
| PeakForce amplitude | 150 nm |
| Lift scan height | 100 nm |
| Drive amplitude | 500 mV |
| Lockin-2 bandwidth | 27 Hz |
| Bias routing | Tip routing |

The calibrated CPD value of the nanoparticles is related to the work function of cantilever tip and work function of nanoparticles by the Equation 3:

$$CPD = \frac{\left(W_{Tip} - W_{NP}\right)}{e} \qquad \text{Equation 3}$$

where $W_{Tip}$ and $W_{NP}$ are the work functions of cantilever tip and the nanoparticles, respectively. $e$ is the absolute value of the elementary charge. Based on this relation, the changes in CPD and work function are of opposite sign.

4.2.3 Current mapping and IV spectroscopy

Current mapping and IV spectroscopy characterization under PF TUNA mode was performed using Bruker Multimode 8 atomic force microscopy (AFM) under ambient atmosphere with relative humidity of less than 40%. Olympus conductive tip (ACM240TM) is made up of Antimony n-doped silicon (Si) tips of 10-15 μm tip height with resonant frequency of 70 kHz and spring constant of 2 $Nm^{-1}$. ACM240TM were utilized for all current measurements. The tip is coated with a layer of Pt/Ir, which may potentially wear off upon multiple scanning and excessive applied sample bias. For accuracy and consistency purposes, all images of the monometallic and bimetallic nanoparticles in a particular series were measured using a new cantilever tip. It is important to note that the nominal tip radius of the ACM240TM is 15 nm and it might increase to a maximum value of 20 nm due to the rounding effect after multiple usage, which might affect the resolution of the topography and current measurements. For current mapping, the parameters used are listed in Table 10. In order to perform IV spectroscopy, the cantilever tip was ramped on the nanoparticles with a linear voltage sweep from 0 to 5 V.

**Table 10.** AFM parameters for current mapping under PF TUNA mode.

| AFM parameters | Value |
|---|---|
| Scan size | 1 μm |
| Scan rate | 0.5 Hz |
| Gain | 10 |
| Setpoint | 0.1 V |
| PeakForce amplitude | 100 nm |
| Sample bias | 0 V and 0.2 V |
| Ramp begin | 0 |
| Ramp end | 5 V |

### 4.2.4 Two-point probe IV measurement

Bulk IV linear sweep was performed using a Keithley 2450 sourcemeter source measure unit (SMU) instrument. In order to etch away the MNPs and BNPs to reveal the FTO substrate, dilute hydrochloric acid (0.1 M) was used, followed by acetone to remove the acid. Copper adhesive tape was used as the connection to the positive and negative terminal. All measurements were performed at room temperature and relative humidity of 25 $^{o}$C and <40%, respectively.

### 4.2.5 High resolution- Transmission Electron Microscopy (HR-TEM) imaging and Energy Dispersive Spectroscopy (EDS)

Transmission electron microscopy (TEM) lattice spacing and energy dispersive spectroscopy elemental composition analysis of nanoparticles were carried out using a FEI Tecnai G2 F20 instrument and the operation voltage is 200 kV. Samples preparation was performed using a lamella preparation method via Helios Nanolab 600 Dual Beam Focused Ion Beam Milling System (FIB).

### 4.2.6 X-ray diffraction (XRD)

Crystallographic structure of MNPs and BNPs was characterized using Bruker D8 Discover X-ray diffractometer instrument with filter at 1.54 Å. The diffraction angle was collected with a 2 theta range between 20$^{o}$ to 80$^{o}$ with a fix scan rate of 0.02$^{o}$ per step and step size of 0.02$^{o}$ per minutes.

### 4.2.7 Field-emission scanning electron microscopy (FESEM)

Hitachi S-3400 II was utilized to characterize the diameter and density of the MNPs and BNPs. The specification used during FESEM imaging include; voltage: 15.0 kV, Magnification: X70k and X300k, probe current: high. The distance between the sample and secondary electron (SE) detector was maintained at 8 mm.

### 4.2.8 Ultraviolet-visible Spectroscopy (UV-Vis spectroscopy)

Absorption spectra of MNPs and BNPs on FTO were recorded using Agilent Cary 100 Ultraviolet-visible spectrophotometer between wavelength range of 200$^{o}$ to 900$^{o}$.

### 4.2.9 Photoluminescence (PL) spectroscopy

Steady-state PL spectroscopy measurement of ZnO/ MNPs and ZnO/ BNPs were recorded using LabRAM HR from Horiba Scientific with excitation wavelength of 325 nm with specification as shown in Table 11.

**Table 11.** PL spectroscopy parameters.

| Parameters | Value |
|---|---|
| Range (nm) | 200 - 900 |
| Acquisition time (s) | 5 |
| Accumulation | 2 |
| RTD time (s) | 5 |
| Objective | NUV 40 |
| Grating | 600 gr/mm |
| ND Filter (%) | 100 |
| Hole | 100 |
| Range | Ultraviolet |

4.2.10 Raman spectroscopy

Raman spectroscopy measurement were recorded using LabRAM HR from Horiba Scientific with excitation wavelength of 514 nm. The parameters used during the characterization is as shown in Table 12.

**Table 12.** Raman spectroscopy parameters.

| Parameters | Value |
|---|---|
| Range ($cm^{-1}$) | 500 - 2000 |
| Acquisition time (s) | 5 |
| Accumulation | 2 |
| RTD time (s) | 5 |
| Objective | X50 |
| Grating | 1800 gr/mm |
| ND Filter (%) | 100 |
| Hole | 100 |
| Range | Visible |

4.2.11 Gamry Potentiostat (Photoelectrochemical measurement)

PEC measurements were performed with a potentiostat (Gamry Interface 1000E Potentiostat) in a three-electrode system using 0.5 M sodium carbonate ($Na_2CO_3$) as the electrolyte. The ZnO photo-anode, a Pt electrode, and an Ag/AgCl electrode were utilized as the working, counter, and reference electrodes, respectively. To excite the sample, an external 500W Xenon light source (CHF-XM-500W) coupled with an AM 1.5G filter (UV-Vis-NIR) was used with light intensity of 100 mW $cm^{-2}$. Chronoamperometry (CA) measurement was conducted with an applied bias of 0.4 V. Linear sweep voltammetry (LSV) was measured at a scan rate of 10 mV $s^{-1}$ from -1.0 to 1.2 V versus Ag/AgCl in the positive sweep direction. Electrochemical impedance spectroscopy (EIS) was performed between frequencies of 0.1 Hz to 100 kHz with an applied AC bias of 0.5V. All the measurements were performed in ambient condition.

## 4.3 Theoretical Simulation

### 4.3.1 Molecular dynamics (MD) simulations

MD simulations of the BNPs formation were performed to understand the atomic diffusion process. The initial model was set to mimic the deposition process of Ag and Au films as shown in Figure S3(a). The interatomic potential was calculated by the embedded atom method (EAM) proposed by [135], which can effectively describe the self-diffusion and impurity diffusion of fcc metals, such as Ag and Au. The time scale of thermal diffusion at such low temperature in our experiment is much larger than the capacity that MD simulation can achieve. In order to speed up the diffusion time scales to be within those accessible to MD simulations, the initial model was heated to 1400K for a period of time of 4 ns, and then gradually decreased the temperature to 600K at a rate of 0.05 K/ps. The simulation work is collaborated with Dr. Kim Jung-Mu.

### 4.3.2 Electromagnetic Field Simulation

The electric field distribution profiles of Ag NPs and 0.25 Au/Ag BNPs were obtained using a finite element method, FEM (HFSS ANSYS, Inc., USA) under excitation wavelength of 532 nm. The simulation was conducted by assuming a 56 nm of single Ag NPs and 50 nm of Au/Ag BNPs growth on a FTO region. The estimated diameter for both NPs were obtained using a HRTEM analysis. In the model, the dimension of whole layers was symmetry with the schematic view. The light source was considered as a plane wave propagates along the -Z direction with a polarization along the X direction. The simulation region including radiation box for boundary condition is $200 \times 200 \times 200$ nm$^3$ with a mean mesh volume of 0.01 nm$^3$. The simulation work is collaborated with Dr. Yu Hao, Dr Wu Bao and Dr Wu HengAn.

# Chapter 5 Result and Discussion

## 5.1 Phase 1: Fabrication of Au/Ag BNPs /FTO

### 5.1.1 Structural Characterization:

Structural analysis were performed to study the physical dimension, crystallographic orientation plane, elemental composition and distribution of the synthesized MNPs and BNPs. In order to synthesize Au/Ag BNPs, it is crucial that monometallic Au NPs and Ag NPs were investigated with regards to their annealing temperature with a nominal film thickness of 10 nm. The film thickness was determined based on the surface roughness of the substrate. The surface roughness of the FTO substrate was determined to be 15.45 nm. If a thicker metal film thickness as compared to the surface roughness was deposited, solid-state thermal dewetting process will result in the formation of non-uniform size NPs, while a thinner metal film thickness as compared to the surface roughness will result in the formation of uniform size NPs. The annealing temperature during solid-state thermal dewetting is an important factor. Figure 9 shows the FESEM images of the morphology with respect to different annealing temperature ranging from 200 $^{o}$C to 450 $^{o}$C. It is worthy to note that the electrical and optical properties of the FTO substrate will be damaged if the annealing temperature exceed 500 $^{o}$C. Solid-state thermal dewetting process can be mainly categorized into several process, namely, initiation of cracks, propagation of cracks, void growth and formation of nanoparticles. Based on Figure 9, at 200 $^{o}$C, initiation of cracks were observed for Au film, while both initiation and propagation of cracks occurred in Ag film. As the annealing temperature increases to 250 $^{o}$C, propagation of cracks occurred for Au film, while void growth was observed for Ag film. Furthermore, at 300 $^{o}$C, void growth was observed for Au film, while the formation of fully spherical nanoparticles occurred for Ag film. As the temperature

further increased above 300 ºC, formation of fully spherical nanoparticles occurred for Au film, while micro-particles were formed for Ag film at 350 ºC. The formation of micro-particles is undesirable as it diminishes the LSPR effect.

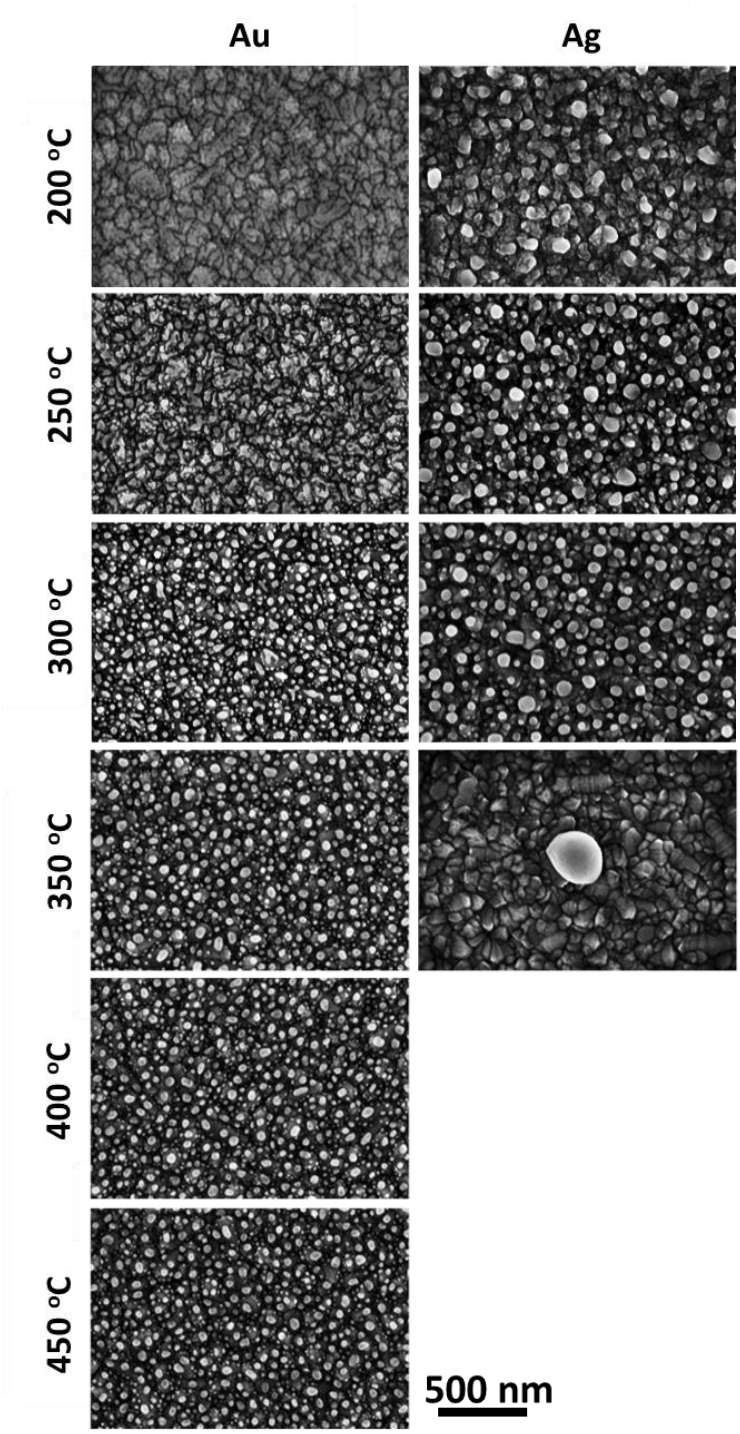


**Figure 9.** FESEM image of monometallic Au NPs and Ag NPs thermally annealed at various temperatures.

A layer of Au/Ag BNPs was successfully deposited on FTO substrate via successive thin film sputtering and solid-state thermal dewetting process. The detailed fabrication procedure described in the experimental methods. The structural properties of BNPs were investigated by varying the composition ratio, $C_{Au/Ag,}$ of Au and Ag (0.25, 0.43 and 0.67 Au/Ag). It is important to systematically investigate the annealing temperature of Au/Ag deposited film as shown in Figure 10. The morphology of the Au/Ag BNPs shows initiation of cracks and propagation of cracks at 200 $^{o}$C, void growth at 250 $^{o}$C and formation of NPs at 300 $^{o}$C. This is in accordance to the results from Au and Ag as shown in Figure 9, which indicate that the annealing temperature of 300 $^{o}$C is sufficient to transform the deposited bi-metal films to NPs. Figure S4 displays the histogram plot of the average diameter and its size distribution of MNPs and BNPs. As the $C_{Au/Ag}$ decreases from 0.67 to 0.25 (Ag composition ratio increased), both the average diameter and interparticle spacing increases linearly as observed in Figure 11. This further validates the $C_{Au/Ag}$ within the BNPs as Ag has a higher diffusion rate compared to Au, thus resulting in the increase of average diameter and interparticle spacing as the Ag composition ratio increases.

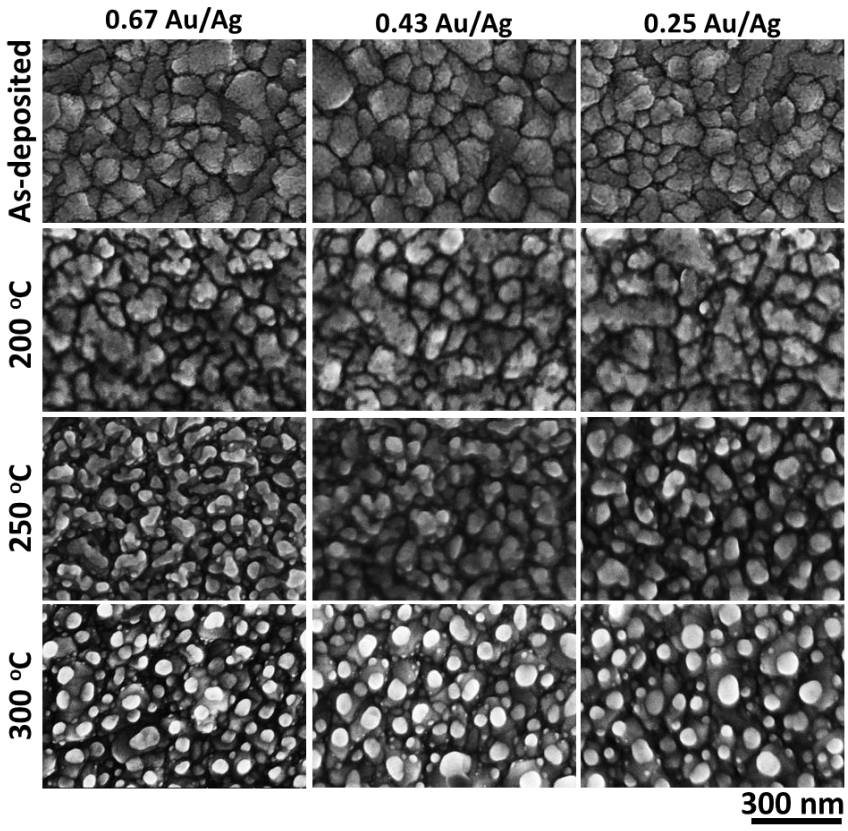


**Figure 10.** FESEM image of Au/Ag BNPs thermally annealed at various temperatures.

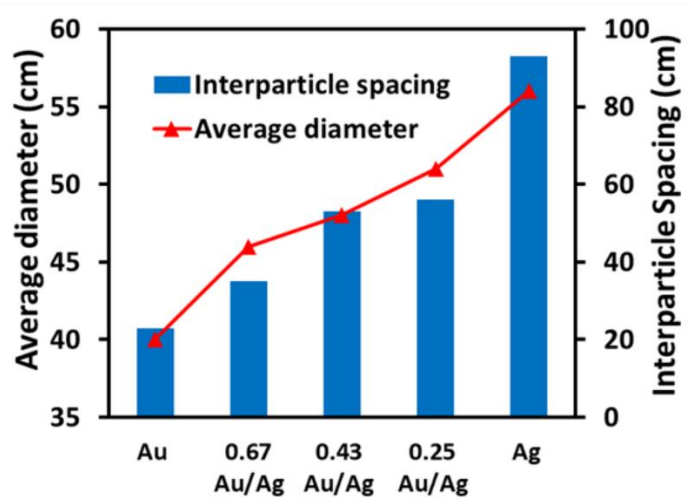


**Figure 11.** Interparticle spacing and average diameter against the various composition.

The crystallographic structure of the BNPs was confirmed by XRD. Overall, there were no others impurity peaks being observed in the XRD spectrum as shown in Figure 12. The Bragg reflection peaks are located at angles of 38.0° and 44.5°, which can be indexed to (111) and (200) lattice plane, respectively. Both Au and Ag element has the same diffraction peaks because of the similar face centered cubic (FCC) structure and lattice constant. Furthermore, the ratio of the diffraction peak intensity of (200) crystallographic plane to (111) plane was determined to be 0.12, which indicate the dominance of the (111) plane. As a result, this indicates that (111) is the predominant crystallographic plane in the MNPs and BNPs in this study.

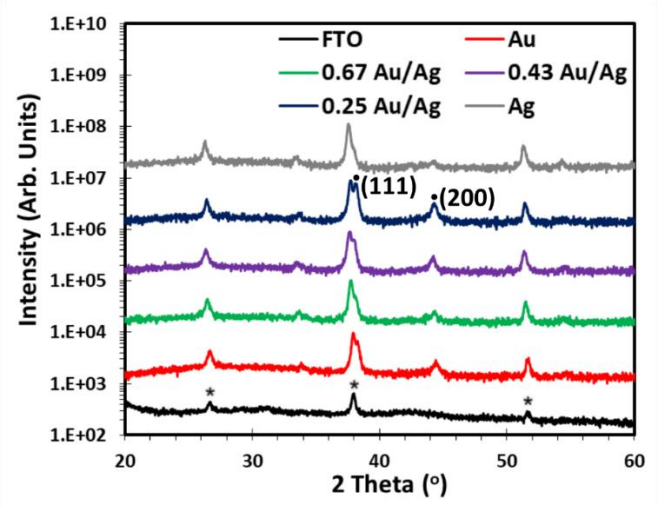


**Figure 12.** XRD spectrum of Au NPs, Ag NPs and various composition of Au/Ag BNPs. The black asterisks indicate the peaks of FTO substrate.

. Figure 13(a) shows the formation of optimal 0.25 Au/Ag BNPs is validated using a high resolution TEM and its corresponded EDS images in Figure 13(b). Few elements are detected namely Ag, Au, Sn and O, whereas the observed Cu and Pt peaks attributed to Cu grid and Pt was used for the preparation of lamella lift out process (refer to Figure S5). The images of sample prepared from lamella method were subjected to cross-sectional EDS mapping. Interestingly, it

was found that both the Au and Ag were distributed uniformly within the BNPs with Ag clusters indicated by the red dotted circle as shown in Figure 13(c), suggesting relatively low annealing process at 300$^{o}$C promotes the inter-diffusion of Ag and Au atoms. Such low sintering temperature for Au/Ag alloying is correlated to the melting temperature of Au/Ag being significantly lower compared to the bulk values due to the nanoparticle size effect [136]. This finding is in accordance to the previous report [137]. The detailed mechanism related to the formation of Au/Ag BNPs was further confirmed via de-alloying method. Typically, the prepared sample was immersed in concentrated nitric acid and the corresponded sample was then observed via HRTEM-EDS mapping analysis as shown in Figure 13(d). It is found that the Ag was partially removed from the crystal lattice of BNPs, evidencing the self-diffusion mechanism of as-growth BNPs via dewetting approach. The alloying process of Au/Ag BNPs can be explained due to the low activation energy of Ag compared to Au and the vacancy energy formation of Ag (1.10 eV) is higher than Au (0.83 eV) [137], therefore Ag atoms are more mobile and possess higher tendencies to diffuse into Au vacancies. The diffusion of Ag NPs towards the surface of FTO after the annealing process also can be related to a higher lattice matching between the ion $Ag^{+}$ and FTO as compared to $Au^{+}$ [138]. In addition, the results of MD simulation also show that the mean square displacement (MSD) of Ag is slightly larger than Au as shown in Figure S3(b), indicating that the diffusion rate of Ag is greater. Hence, a smaller energy tends to diffuse the $Ag^{+}$ towards the surface of FTO. In addition to that, EDS analyses were performed to determine the element atomic ratio within the NPs in comparison with the deposited Au and Ag film thickness ratio as shown in Figure 13(e) and Figure 13(f), respectively. It can be observed that the Au and Ag EDS atomic ratio corresponded well with the deposited Au and Ag film ratio (Table S1), thus indicating that tunable Au/Ag BNPs atomic ratio can be achieved by controlling the deposited Au and Ag film thickness ratio.

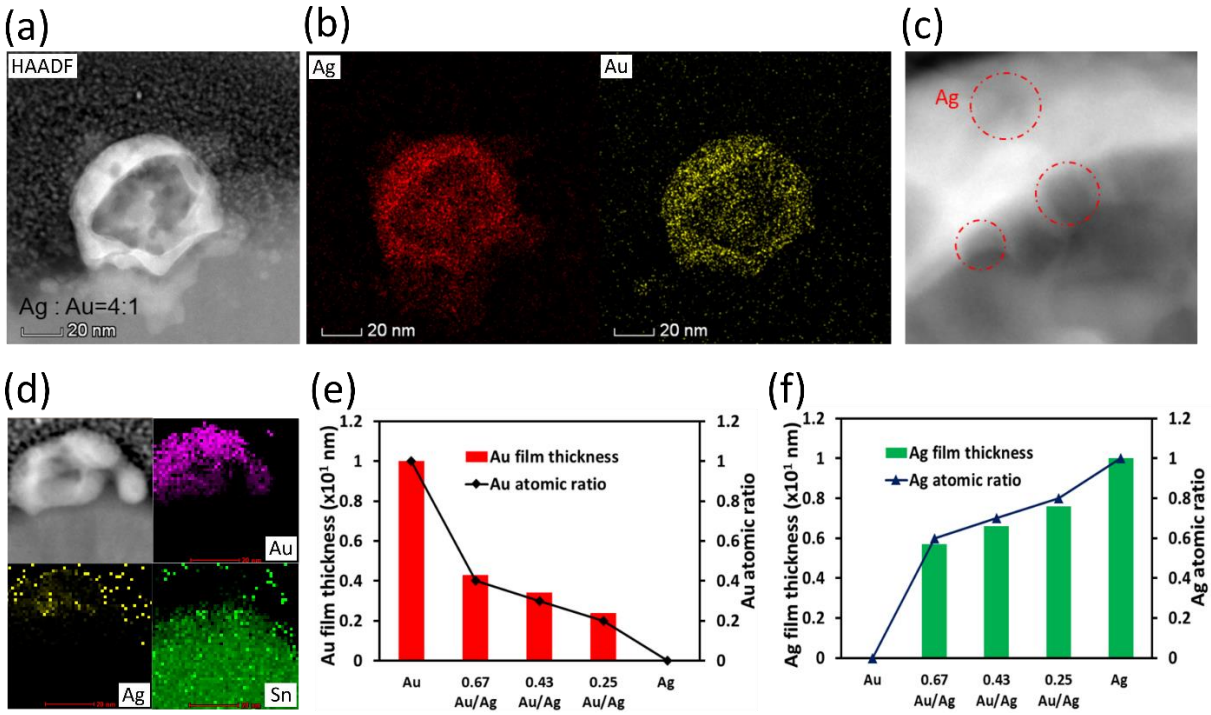


**Figure 13.** (a) HRTEM images for 0.25 Au/Ag BNPs, corresponded (b) EDS mapping for sample prepared and (c) Ag clusters within the BNPs. (d) EDS mapping of dealloyed 0.25 Au/Ag BNPs. Individual metal film thickness and EDX atomic ratio of (e) Au and (f) Ag element.

5.1.2 Optical Characterization:

Figure 14 shows the absorbance spectra of the Au and Ag nanostructures at various annealing temperatures using UV-Vis spectroscopy. It was observed that both Au film and Ag film were unable to exhibit distinct surface plasmon resonance (SPR) peak as shown in Figure 14(a) and Figure 14(b), respectively. As the annealing temperature increases to 200 $^{o}$C, the emergence of the SPR peak is due to the initiation and propagation of cracks on the metallic film for both Au and Ag. As the metallic film transformed into nano-islands due to the void growth at 250 $^{o}$C, the SPR peak was blue-shifted. At 300 $^{o}$C, a more prominent SPR peak was observed. Additional increase in the annealing temperature above 300 $^{o}$C resulted in no noticeable shift in the SPR peak

for Au as the formation of NPs have been achieved and stabilized. Meanwhile, the SPR peak for Ag diminished for annealing temperature above 300 $^{o}$C, indicating that the nanoparticles have been transformed into micro-scale structures which loses the SPR effect as the dimension of the structure is larger than the wavelength of the incoming photons. Therefore, this further validated that the optimal annealing temperature for both Au and Ag is 300 $^{o}$C.

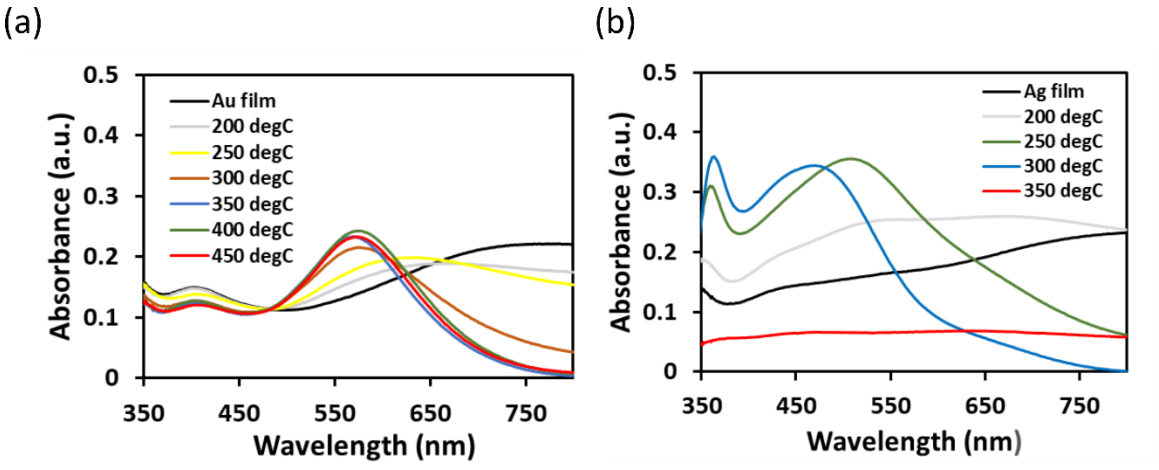


**Figure 14.** Absorbance spectra for (a) Au and (b) Ag with various thermal annealing temperature.

Figure 15 shows the physical color changes of the samples, indicating a unique absorbance spectra of the BNPs and MNPs. There are only single peaks observed in the absorbance spectra at the visible region as shown in Figure 16(a). Typically, Ag NPs and Au NPs exhibited a prominent measured SPR peak at 465 nm and 559 nm, respectively. The different SPR peaks of the metallic NPs can be related to the material dependent effect. When the ratio of BNPs decreased from 0.67 to 0.25 (Ag ratio increased), a hypochromic shift (blue shift) was observed and justified via Mie theory as shown in Figure 16(b). However, the distribution of the peaks were remained at the interval between the element Ag and Au. Furthermore, the FWHM of the peaks were found to be

varied with the ratio of BNPs. Au NPs have SPR phenomena active in the range from 500 to 650 nm, while Ag NPs is active in the range from 400 nm to 500 nm. However, Au/Ag BNPs result in a broad peak that was observed in the lower visible wavelength region between 400 to 650 nm. The combination of Au and Ag is responsible for the broadening of the LSPR, and it also increases the imaginary component of dielectric function of metals. It also resulted in the formation of hot electrons due to a fast rate of LSPR relaxation. It is worthy to note that the bimetallic 0.25 Au/Ag NPs has broaden absorption spectrum as compared to Au NPs and Ag NPs. To gain further insight on the elemental distribution of BNPs in this study, the absorption spectra trend of different BNPs structures by other studies was considered. For instance, studies have shown that physical mixture of monometallic Au NPs and Ag NPs resulted in two absorption peaks due to the SPR of Au and Ag atoms, respectively [139]. Also, it was reported that no shift in the SPR peaks were observed by altering the physical blending ratio, except the relative intensity of the two SPR peaks. Furthermore, core shell structure with thin or thick shell thickness exhibited two SPR peaks (core and shell) [26] or single SPR peaks (shell) [140], respectively. Therefore, the presence of only one SPR peak and its shift with different elemental composition clearly support the formation of alloyed Au/Ag BNPs, which corroborated with the EDS elemental distribution mapping in Figure 13(b).

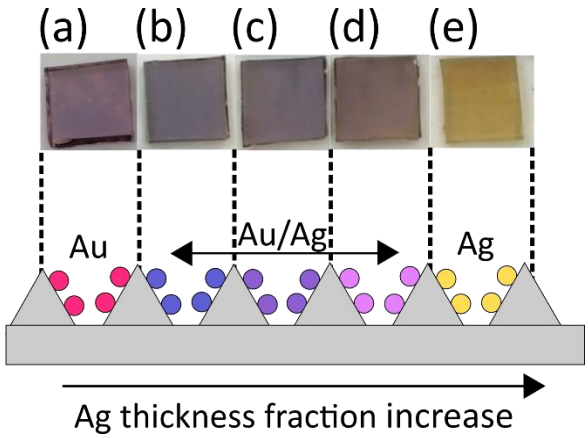


**Figure 15.** Physical images of the (a) Au NPs, (b) 0.67 Au/Ag BNPs, (c) 0.43 Au/Ag BNPs, (d) 0.25 Au/Ag BNPs, and (e) Ag NPs, with increasing Ag thickness fraction.

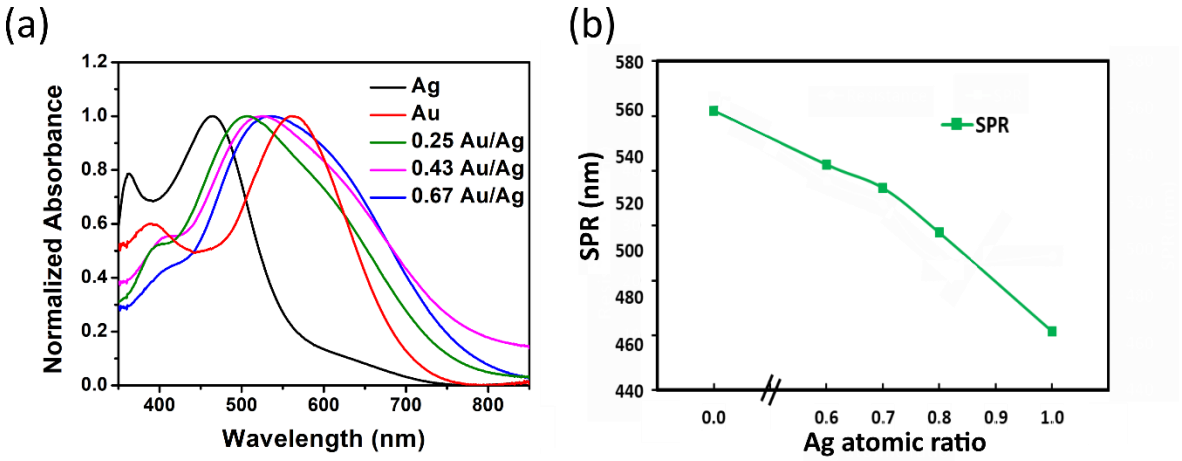


**Figure 16.** (a) Normalized absorbance spectra for prepared samples and (b) surface plasmon resonance graph against Ag atomic ratio.

### 5.1.3 Electromagnetic Field Simulation

To further verify the electrical field distribution and plasmonic properties of bimetallic NPs, finite element method (FEM) was performed for sample Ag NPs and 0.25 Au/Ag BNPs. The

data on the morphology and the size of Ag and 0.25 Au/Ag BNPs were obtained from experimental measurements. Based on FEM simulations, Figure 17(a) and Figure 17(b) exhibit the electric field distribution of a single Ag NPs and 0.25 Au/Ag BNPs on the surface of FTO at incident wavelength of 532 nm. Compared to the single Ag NPs, it can be clearly observed that 0.25 Au/Ag alloy BNPs display stronger E-field enhancement not only in the original locations around the semispherical shape, but also E-field around the high-density Au NPs inside the BNPs. This result is in good agreement with previous report [141], where Au/Ag BNPs exhibit higher electric field than Au NPs and Ag NPs. Therefore, according to the FEM, it is confirmed that 0.25 Au/Ag BNPs have great potential for SERS application.

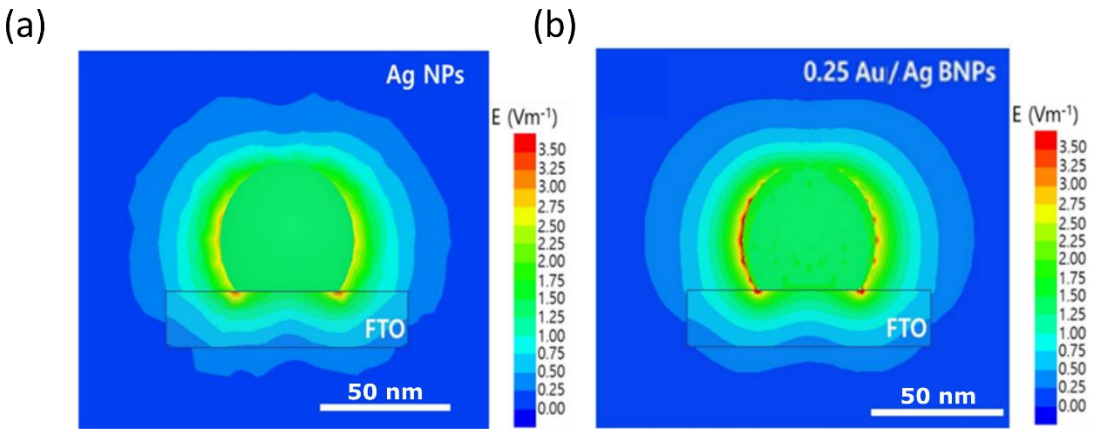


**Figure 17.** Simulation of electrical field distribution of (a) Ag NPs and (b) 0.25 Au/Ag BNPs using FEM methods. The simulation work is collaborated with Dr. Kim Jung-Mu.

### 5.1.4 Electrical and Energy Band Characterization

Furthermore, the electronic states of 0.25 Au/Ag BNPs was further evaluated using XPS analysis and compared to the reference sample of Ag NPs and Au NPs. The narrow scan spectra for the element Ag and Au were plotted in Figure 18(a) and Figure 18(b), respectively. According

to Table **S3**, the gaps between the $4f_{7/2}$ and $4f_{5/2}$ peaks of Au ($\Delta$=3.7 eV) as well as those between the $3d_{5/2}$ and $3d_{3/2}$ peaks of Ag ($\Delta$=6.0 eV) are similar as the values for zero-valent Au and Ag [142]. This result demonstrates that Au and Ag atoms exist in a zero-valent state in all prepared nanoparticles. The binding energy position of monometallic nanoparticles were similar to their corresponding bulk metallic state (84.0 eV for bulk Au and 368.2 for bulk Ag) as indicated by the black dotted lines in Figure 18**.** There are no significant changes (approximately zero) in the orbital splitting for the spectra of both Ag NPs and Au NPs in Figure 18(a) and Figure 18(b), respectively, which indicates the ionization energy of Au and Ag remains unchanged. However, a negative and positive core level shift was observed for 0.25 Au/Ag BNPs alloy, where Ag $3d_{5/2}$ shifts from 368.2 eV to 367.7 eV (Figure 18(a)) and Au $4f_{7/2}$ from 84.0 eV to 84.2 eV (Figure 18(b)) as compared to Ag NPs and Au NPs, respectively. The observation of positive and negative binding energy shifts can be attributed to the formation of metal-metal bonds. This further confirms that sintering process promotes an alloying formation of Au/Ag BNPs. The shifts of Ag $3d_{5/2}$ to lower binding energies in BNPs alloy can be associated to the electron transfer from the Ag to Au atoms because of higher electron affinity of Au compared to Ag [143], thus decreasing the electron density of the Ag. Meanwhile, the shifts of Au $4f_{7/2}$ is attributed to the reduced coordination number of Au atoms and related to the degree of rounding of Au [144]. This occurrence can be related to the strong electronic interaction between Au and Ag atoms within the crystal domain of BNPs.

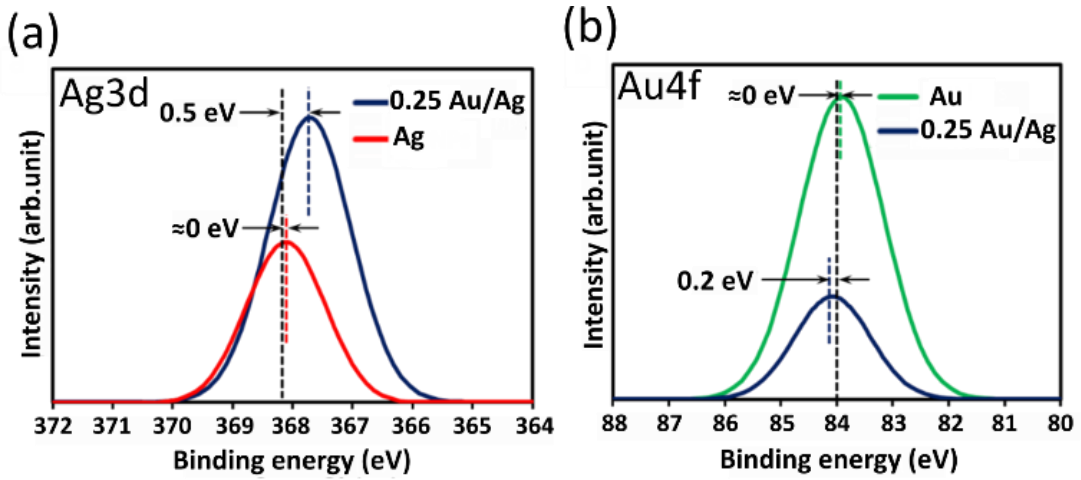


**Figure 18.** Narrow scan XPS analysis at specific region of (a) Ag $3d_{5/2}$ and (b) Au $4f_{7/2}$ of Au NPs, Ag NPs, and 0.25 Au/Ag BNPs.

To study the electrical properties of the BNPs, bulk current-voltage (I-V) characteristic measurements were performed using a two point probe system as shown in Figure 19(a). A two point probe system was used, instead of a four point probe system, to provide a relative comparison of the resistance between the samples before proceeding to nanoscale electrical characterization. The sheet resistance values are obtained using the resistance value extracted from the linear voltage sweep results in Figure 19(a). It is important to note that the calculated sheet resistance of the samples in Table S4 is based on the sheet resistance of FTO substrate (13 Ω/sq) provided by the manufacturer as reference. Generally, formation of NPs on the FTO substrate resulted in the reduction of resistance due to the large coverage of NPs acting as parallel conduction channels connected in series with the FTO. As the equivalent resistance of any two resistors, in our case, FTO and NPs, is always lower than the constituent resistances, the overall sheet resistance of FTO with NPs will reduced. Furthermore, as the MNPs and BNPs are relatively large with an average diameter ranging from 39 nm to 56 nm (Figure S4), the NPs are able to bridge any electrical discontinuity at the grain boundaries on the FTO film, which has a root mean square (RMS)

roughness of 15.2 nm ±0.437 nm. According to Figure 19(b), for monometallic NPs, Ag NPs have a lower sheet resistance compared to Au NPs. The reduction of sheet resistance by Ag NPs and Au NPs as compared to pristine FTO are 63.4 % and 22.3 %, respectively. This is due to the fact that Ag (111) has a lower work function of approximately 4.74 eV, as compared to Au (111) of 5.20 eV. The work function corresponds to the minimal energy required to remove an electron from the metal atom. Hence, for Ag NPs, the probability of electrons having energy more than the minimal energy required for electron transfer is higher than Au NPs. This explained the better electrical conductivity of Ag NPs, and hence higher reduction of sheet resistance.

The calculated sheet resistance of the samples in Figure 19(b) shows a linear decreasing trend as the Ag atomic ratio increases before slightly increases as the Ag atomic ratio reach 1.0. Au NPs and Ag NPs have a sheet resistance of 10.11 Ω/sq and 4.76 Ω/sq, respectively. In the case of BNPs, as the Ag composition ratio increases, the sheet resistance of the sample decreases. Remarkably, 0.25 Au/Ag BNPs have the lowest sheet resistance of 4.63 Ω/sq among the NPs. This shows a 64.401% reduction of the sheet resistance as compared to the reference FTO. The electrical conductivity is highly dependent on the type of metal. In general, Ag has a better electrical conductivity compared to Au due to the lower work function. Therefore, as the Ag atomic ratio increases, the resistance gradually decreases. However, Ag NPs have a higher resistance compared to the optimal 0.25 Au/Ag BNPs, which might be due to the surface oxidation of Ag NPs during the thermal annealing process. In this case, Au might potentially serve as a surface oxidation mitigation agent for the BNPs. To further investigate the reduction of resistance, CAFM and KPFM mapping were performed to study the nanoscale electrical properties.

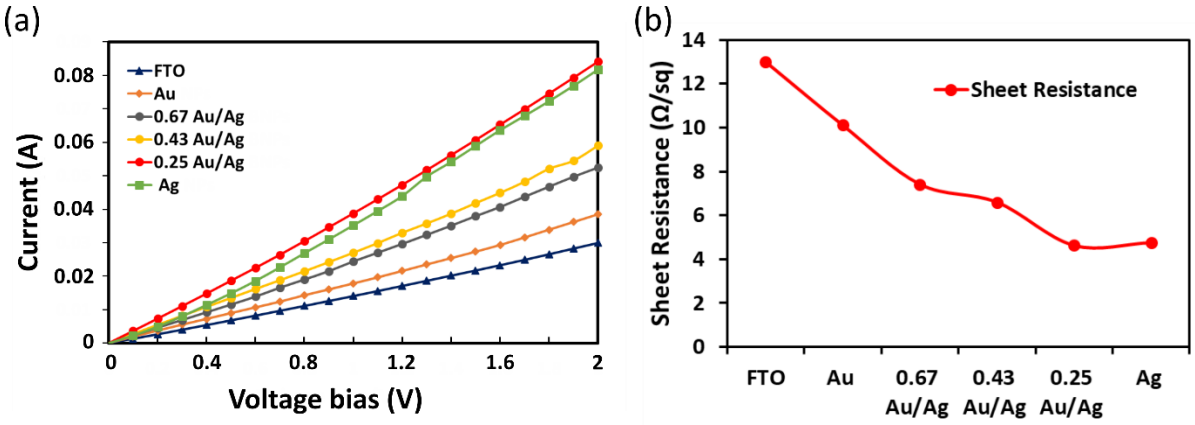


**Figure 19.** (a) Current against voltage bias using macroscopic two-point IV measurement. (b) Sheet resistance against Ag atomic ratio.

5.1.5 Nanoscale Electrical Characterization

Before further analysing the electrical properties, terms such as contact potential difference and work function must be clearly defined in this study. The contact potential difference ($V_{CPD}$) can be defined as the difference in surface potential between cantilever tip and nanoparticles, and work function corresponds to the minimal energy required to remove an electron from the metal atom. It is important to note that the negative sign of the $V_{CPD}$ indicates that a negative DC bias is required to null the positively-charged cantilever tip during Fermi equilibrium [145]. Hence, comparison of the surface potential difference was done using the absolute value. Figure 20 shows the correlation between contact potential difference and work function with Ag atomic ratio. It can be observed that the work function and $V_{CPD}$ decreases with the increase of Ag atomic ratio with 0.25 Au/Ag BNPs having the lowest value before increasing with Ag NPs. This shows that the addition of optimal ratio of Au/Ag will lower the $V_{CPD}$ and work function as compared to Ag NPs during the thermal dewetting fabrication process.

The in-depth electrical properties were evaluated using KPFM and CAFM to determine the contact potential difference and the localized current of BNPs and MNPs. The detailed procedure was highlighted in the appendix (Figure S7). Figure 21(a-c) show the AFM topography images for sample Au NPs, Ag NPs and 0.25 Au/Ag BNPs. It was observed that fine-grain and homogeneous distributed nanoparticles on the FTO substrate surface. Among all of the sample, 0.25 Au/Ag BNPs possess a higher surface roughness value of 18.62 nm and the high surface roughness properties of 0.25 Au/Ag BNPs could be beneficial to the higher amount of hot spots generated throughout the surface that promising to enhance the SERS performance of the plasmonic BNPs alloy [146]. These results are in accordance with the FESEM analysis in Figure 21(d-f) depicts the KPFM mapping of the sample. It is noted that 0.25 Au/Ag BNPs exhibited a lower $V_{CPD}$ values of -99.16 mV as compared to Au NPs and Ag NPs of -245.90 mV and -118.88 mV, respectively. By utilizing the Equation 3, the effective work function can be determined from the value of $V_{CPD}$ and the results are summarized in Table S2. The detail calculation of work function from $V_{CPD}$ are described in Figure S7. The value of work function (WF) for Au NPs and Ag NPs were calculated to be 5.29 eV, and 5.18 eV, respectively. The WF of Au NPs is in good agreement with previous report [147], meanwhile WF of Ag NPs is closed to the reported values as measured by KPFM depending on the NPs size of Ag [148]. Meanwhile, the work function of 0.25 Au/Ag BNPs exhibited slightly lower values of 5.16 eV compared to monometallic NPs, which is related to the equilibrium position of Fermi level between Ag and Au [149]. Theoretically, Au NPs has a higher work function (5.31 eV) [150] than Ag NPs (4.26 eV) [151]. Therefore, the work function of Au/Ag BNPs should have a value between the theoretical range of 5.31 eV and 4.26 eV. However, in this study, the measured work function of Au NPs and Ag NPs were 5.29 eV and 5.18 eV, respectively. It is important to note that the work function of Ag NPs in this study were influenced

by the Ag oxide formed on the surface of the NPs. Due to the inertness of Au element during the thermal annealing process, the work function of Au NPs (5.29 eV) is comparable to the theoretical value of Au which is approximately 5.31 eV. However, Ag element are not thermally stable under ambient condition, hence, a layer of metal oxide (Ag oxide) were potentially formed on the surface of Ag NPs upon thermal annealing at 300 $^{o}$C under ambient condition[95, 152]. Theoretically, the formation of Ag oxide on the Ag resulted in the increased of work function by approximately 0.96 eV [153] from 4.26 eV to 5.22 eV, which is comparable to the value (5.18 eV) measured in this study. As a result, the work function of Ag NPs (5.18 eV) is higher compared to the theoretical value of Ag. Therefore, 0.25 Au/Ag BNPs has the ability to suppress Ag oxidation with the presence of Au, thus slightly lower work function (5.16 eV) compared to Ag NPs (5.18 eV). Meanwhile, the alloying of the Ag element with Au element within the BNPs gives lower work function (5.16 eV) than Au NPs (5.29 eV).

Furthermore, the localized current mapping for all of the sample were performed using CAFM and the results are presented in Figure 21(g-i). During the measurement, the average drift current of the sample was collected by applying a positive sample bias of 0.2 V. It was observed that Au NPs displayed a smallest current as compared to Ag NPs which are 27 pA and 78 pA, respectively, while, 0.25 Au/Ag BNPs displayed the highest drift current value of 507 pA, thus signifying the highest concentration of free charge carrier and effective charge transfer in BNPs. In addition to that, IV spectroscopy shows that 0.25 Au/Ag BNPs exhibited linear IV behaviour in the forward and reverse bias (Figure 21(j)) which indicate the possible direct tunneling of the electrons across the potential barrier. To further validate the electrical enhancement, the histogram in Figure 21(k) displays the overall surface potential distribution, which indicate that 0.25 Au/Ag BNPs has the lowest overall surface potential, hence lowest work function.

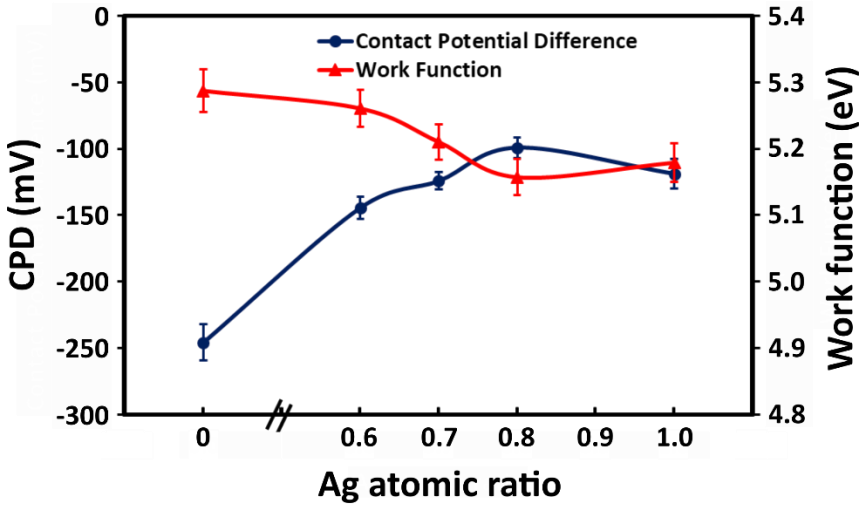


**Figure 20.** Contact potential difference (CPD) and work function against Ag atomic ratio.

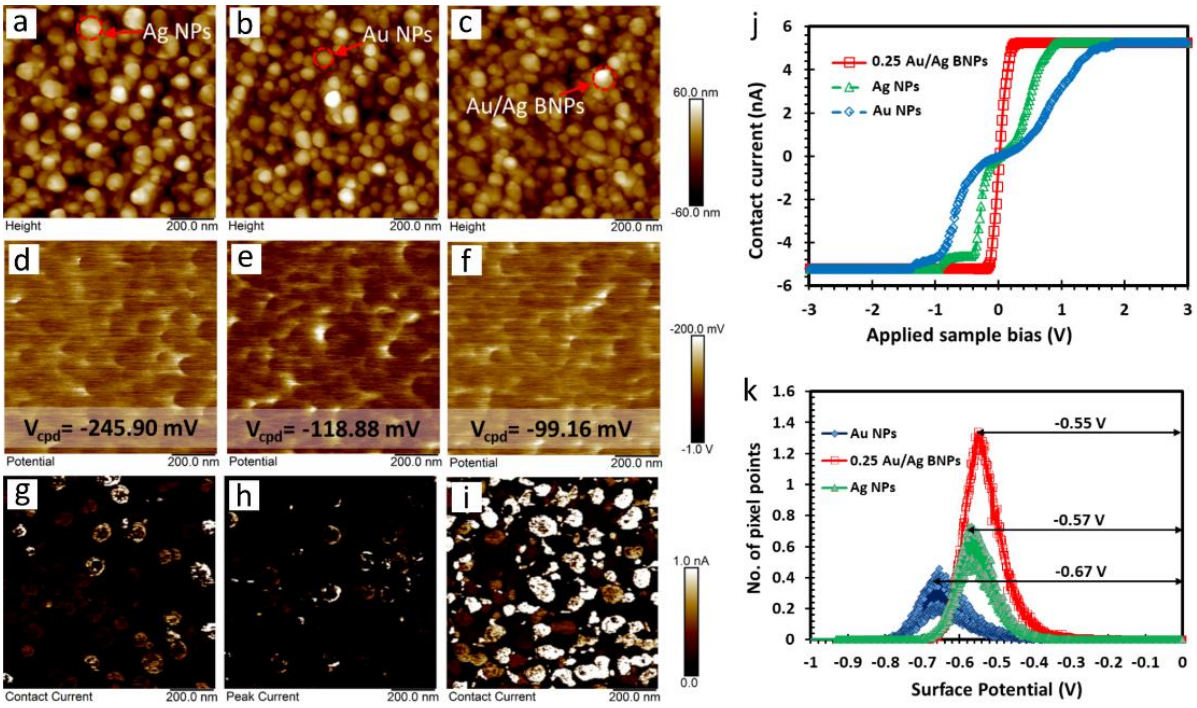


**Figure 21.** The AFM topography and the corresponding localized electrical properties measured using KPFM and CAFM for specific samples of Ag NPs (a,d,g), Au NPs (b,e,h) and 0.25 Au/Ag BNPs (c,f,i). IV spectroscopy and surface potential histogram performed using CAFM and KPFM, respectively.

## 5.2 Phase 2: SERS of Au/Ag BNPs /FTO

### 5.2.1 Enhancement Factor of Congo Red Dye Molecules

To further investigate the plasmonic properties of bimetallic 0.25 Au/Ag NPs, surface enhanced Raman spectroscopy (SERS) using Congo red (CR) dye with concentration of 5μM as the Raman active probe was performed as shown in Figure 22(a). The observed Raman band at 1155 $cm^{-1}$ (N-C stretching mode), 1375 $cm^{-1}$ to 1452 $cm^{-1}$ (N=N stretching mode) and 1595 $cm^{-1}$ (phenyl ring mode) can be attributed to the molecular structure of CR. Based on Figure 22(b), it was observed that bimetallic 0.25 Au/Ag BNPs exhibited a much stronger and better resolved spectrum than that of other MNPs and BNPs with enhancement factor of 1.60 x $10^7$, compared to 8.64 x $10^6$ (0.43 Au/Ag BNPs), 4.71 x $10^6$ (0.67 Au/Ag BNPs), 9.44 x $10^6$ (Ag NPs), and 3.56 x $10^5$ (Au NPs) at Raman band of 1155 $cm^{-1}$. The enhancement factor of 0.25 Au/Ag BNPs is 46% and 71% higher compared to 0.43 Au/Ag and 0.67 Au/Ag, respectively, thus indicating that increased Ag atomic ratio in Au/Ag BNPs exhibits enhanced plasmonic properties. This finding is accordance with the trend in E-field enhancement of 0.25 Au/Ag BNPs based on FEM simulation (Figure 17(a) and Figure 17(b)). Detailed calculation of the enhancement factor can be found in the supporting information (using Equation S3). The enhancement can be attributed to electronic ligand effect in BNPs and localized electric field enhancement. As the WF of Ag (5.18 eV) is smaller than Au (5.29 eV), which will be further discussed in the following section, the Au atoms within the bimetallic NPs have a strong electronic effect on the surface of the Ag atom by charge transfer, thus causing the surface of Ag atoms neighbouring Au atoms to become more active as the Ag atomic ratio increased. Charge transfer between the NPs and the Raman probe molecules occurred during the adsorption process, hence resulting in the formation of a low-energy

absorption band. This absorption band represents the electronic transition from the Fermi level of the NPs to the lowest unoccupied molecular orbital (LUMO) of the Raman probe molecules. Based on the results obtained from KPFM and CAFM, 0.25 Au/Ag BNPs exhibited higher Fermi level compared to Ag NPs, and followed by Au NPs. This claims reflected that the electrons in 0.25 Au/Ag BNPs are dominantly excited from the metal conduction band to the LUMO of the molecules upon laser irradiation during SERS analysis.

a

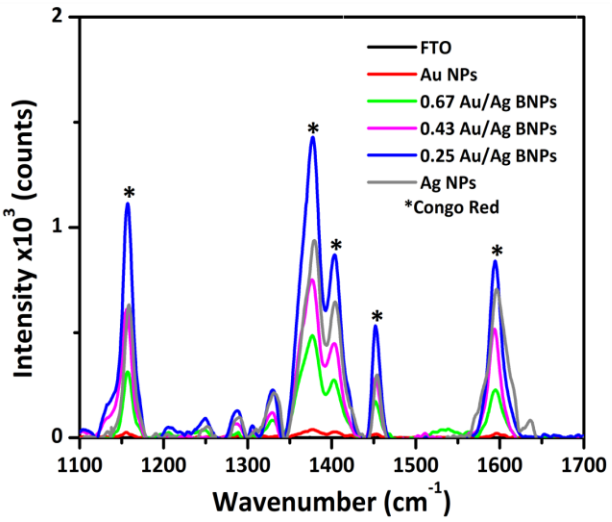


b

| Samples | Enhancement Factor |
|---|---|
| Au NPs | $3.56 \times 10^5$ |
| 0.67 Au/Ag BNPs | $4.71 \times 10^6$ |
| 0.43 Au/Ag BNPs | $8.64 \times 10^6$ |
| 0.25 Au/Ag BNPs | $1.60 \times 10^7$ |
| Ag NPs | $9.44 \times 10^6$ |

**Figure 22.** (a) SERS spectra for samples detected via Congo red (λ laser= 532 nm). (b) Table of SERS enhancement factor for samples calculated using the SERS spectra.

### 5.2.2 Detection Sensitivity of Rhodamine B (R6B) Dye Molecules

In addition to that, the sensitivity of SERS of 0.25 Au/Ag BNPs was also performed under the R6B dye detection. It is noted that the 0.25 Au/Ag NPs exhibited an excellent sensitivity to the dye material and the results are depicted in Figure 23(a). The dominant peaks of R6B are detected at 619 $cm^{-1}$, 1193 $cm^{-1}$, 1275 $cm^{-1}$, 1354 $cm^{-1}$, 1504 $cm^{-1}$, 1523 $cm^{-1}$, and 1642 $cm^{-1}$ [154]. To

confirm the detection signal, the R6B was tested under the bare FTO substrate. There is no signal originated from R6B are detected (refer to Figure S6, affirming the SPR properties from synthesized BNPs sample. Moreover, the detection limit of R6B on the 0.25 Au/Ag BNPs was tested in the different of concentration ranging from 0.01 mg/L to 10 mg/L. Surprisingly, the prepared bimetallic sample is able to enhanced the SERS signal of R6B when the concentration is set in a very low limit of 0.10 mg/L as shown in Figure 23(b). These results indicate the effectiveness of 0.25 Au/Ag BNPs served as a potential materials apply in SERS detector application.

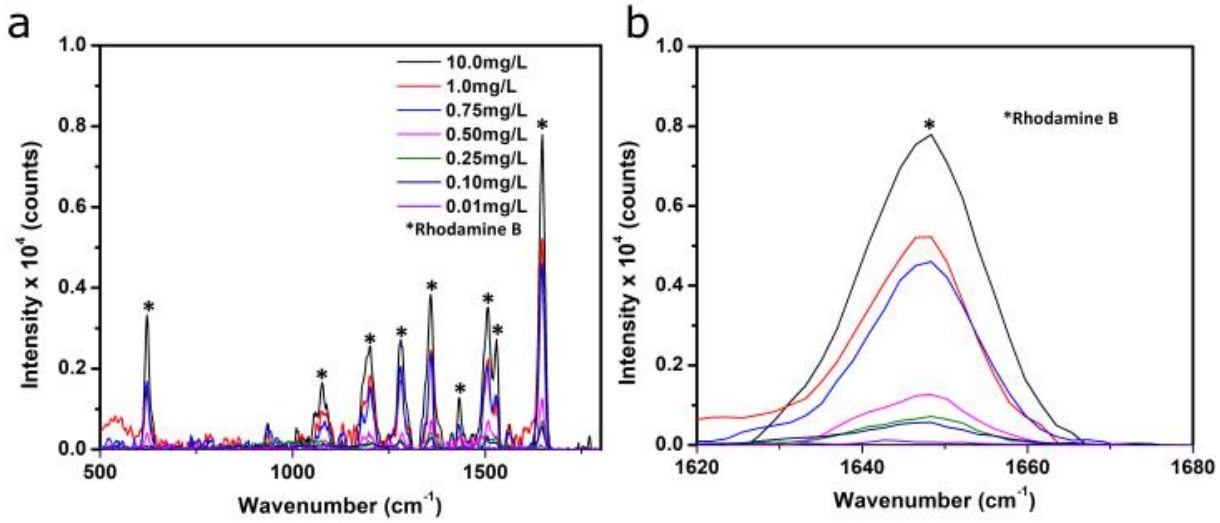


**Figure 23.** (a) Sensitivity of R6B SERS detector using 0.25 Au/Ag BNPs (λ laser= 532 nm). (b) Narrow scan of 1650 $cm^{-1}$ peak.

## 5.3 Phase 3: Synthesis of Au/Ag BNPs/ ZnO/ FTO

### 5.3.1 Surface Morphology of Au/Ag BNPs/ ZnO/ FTO by FESEM

Figure 24 shows the FESEM imaging of pristine ZnO, Au-ZnO, 0.67 Au/Ag.ZnO, 0.43 Au/Ag-ZnO, 0.25 Au/Ag-ZnO, and Ag-ZnO. It is important to note that the atomic ratio of BNPs

deposited on ZnO thin film was determined to be similar as the BNPs deposited on FTO (Figure 13(e) and Figure 13(f)) due to the similar fabrication parameters. As observed in all the images in Figure 24, the spin-coated ZnO nanoparticles thin film have a wide and uniform coverage on FTO substrate, thus forming a continuous thin film. It is important to note any discontinuous defect of the ZnO film will result in the recombination of electron-hole pairs and shorting in the PEC device due to the exposed FTO. This is because ZnO functions as a photo-anode semiconductor layer which enabled generation of electron-hole pair charge carrier upon photon excitation. Therefore, it is crucial to ensure that the ZnO layer forms a continuous film. The thickness of the ZnO thin film is approximately 200 nm based on cross-sectional FESEM imaging. To further analyse the film structural properties of the ZnO film, AFM characterization is utilized to map the morphology of the film as observed in Figure 25. It can be observed that ZnO nanoparticles formed a continuous grainy-textured layer on the surface plane as shown in the insets of Figure 25, as opposed to the FESEM and AFM topography of FTO substrate (smooth plane) as shown in Figure S8. Furthermore, the root mean square (RMS) surface roughness of the ZnO film were characterized under different deposition of metallic NPs. It was observed that the surface roughness value of ZnO film increases as the Ag composition ratio of the BNPs increases. As the fabrication method of Au/Ag BNPs remained the same, the atomic ratio of Au/Ag loaded on ZnO was determined to be similar to the values obtained from the Au/Ag loaded on FTO indicated by EDS characterization in Figure 13e and Figure 13f.

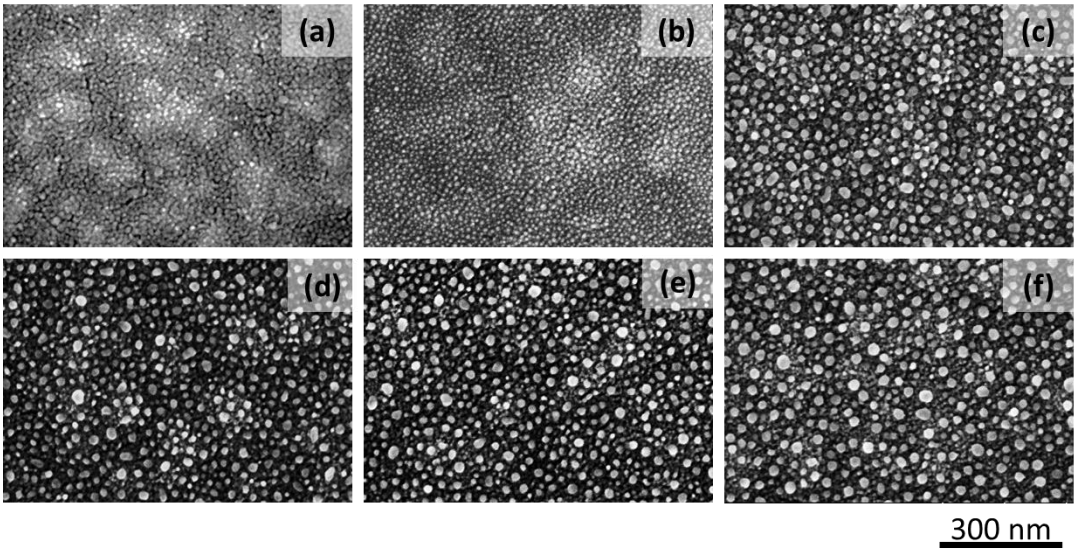


**Figure 24.** FESEM images of (a) Pristine ZnO, (b) Au NPs-ZnO, (c) 0.67 Au/Ag BNPs-ZnO, (d) 0.43 Au/Ag BNPs-ZnO, (e) 0.25 Au/Ag BNPs-ZnO, and Ag NPs-ZnO. Scale of 300 nm indicated by the black line.

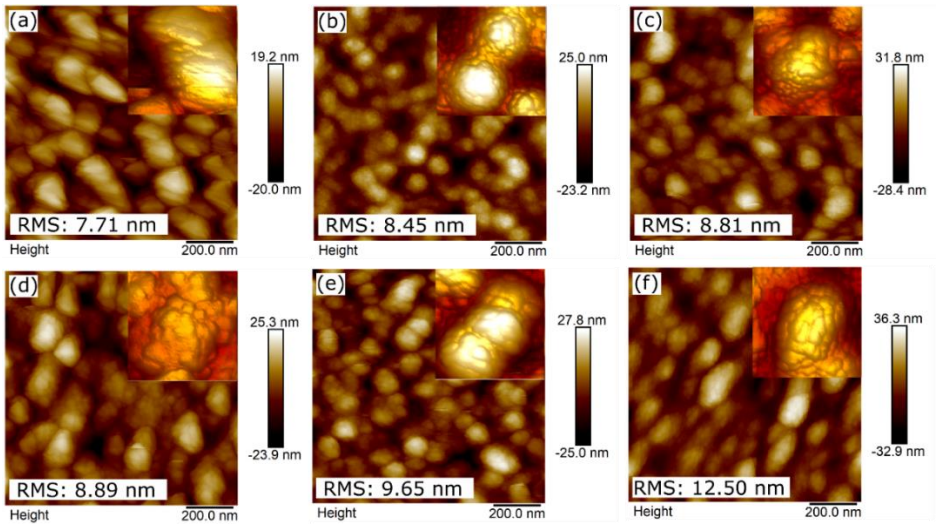


**Figure 25.** AFM topography images (a) Pristine ZnO, (b) Au NPs-ZnO, (c) 0.67 Au/Ag BNPs-ZnO, (d) 0.43 Au/Ag BNPs-ZnO, (e) 0.25 Au/Ag BNPs-ZnO, and Ag NPs-ZnO. The Inset shows the 3D topography mapping.

5.3.2 Crystallographic orientation by XRD

XRD analysis were performed to characterize the crystal orientation of the ZnO. For the XRD analysis of all ZnO thin film with different Au/Ag BNPs as shown in Figure 26, the Bragg reflection peaks are located at angles of 34.0° and 38.0°, which corresponds to lattice spacing of 2.63 Å and 2.37 Å, respectively, and can be indexed to (002) and (111) lattice plane, respectively. While the (002) diffraction peaks indicate a c-oriented ZnO film, the (111) diffraction peaks exhibit face centered cubic (FCC) structure for Au-Ag BNPs. This indicates that the SSTD is a reliable fabrication method as the crystal orientation of Au/Ag BNPs remain unchanged under different underlying material.

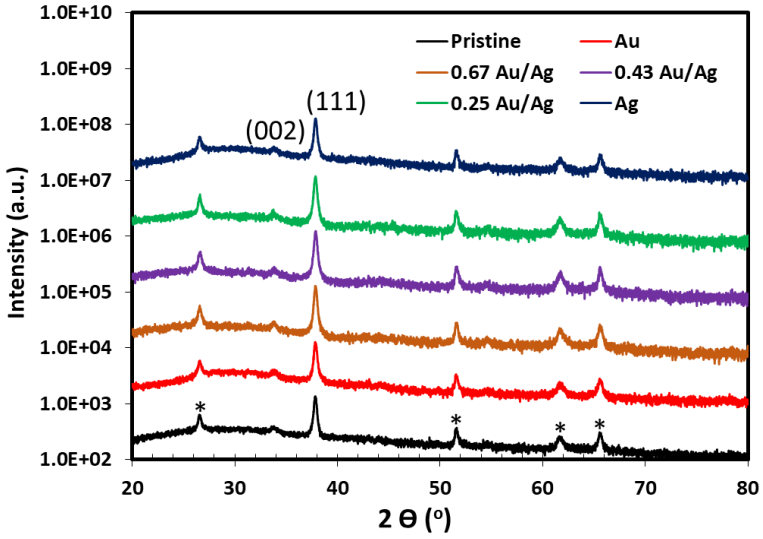


**Figure 26.** XRD patterns of pristine ZnO, Au NPs/ ZnO, 0.67 Au/Ag BNPs/ ZnO, 0.43 Au/Ag BNPs/ ZnO, 0.25 Au/Ag BNPs/ ZnO, and Ag NPs/ ZnO. The black asterisks indicate the crystallographic peak of FTO substrate.

5.3.3 Absorption Spectra by UV-Vis spectroscopy

In order to understand the enhancement by the metallic nanoparticles, the absorption spectra of ZnO with different ratio of Au/Ag BNPs integrated beneath the ZnO thin film was analysed as shown in Figure 27. It was observed that the SPR of the metal nanoparticles without the active layer are: Au NPs-ZnO (622 nm), 0.67 Au/Ag-ZnO (580 nm), 0.43 Au/Ag-ZnO (558 nm), 0.25 Au/Ag-ZnO (536 nm), and Ag-ZnO (513 nm). As the Ag composition ratio increased, a blue shift of the SPR wavelength was observed which is in accordance to the dominance of the metal type with higher composition ratio in a BNPs. This observation is in accordance to the absorption spectra observed in Figure 16.

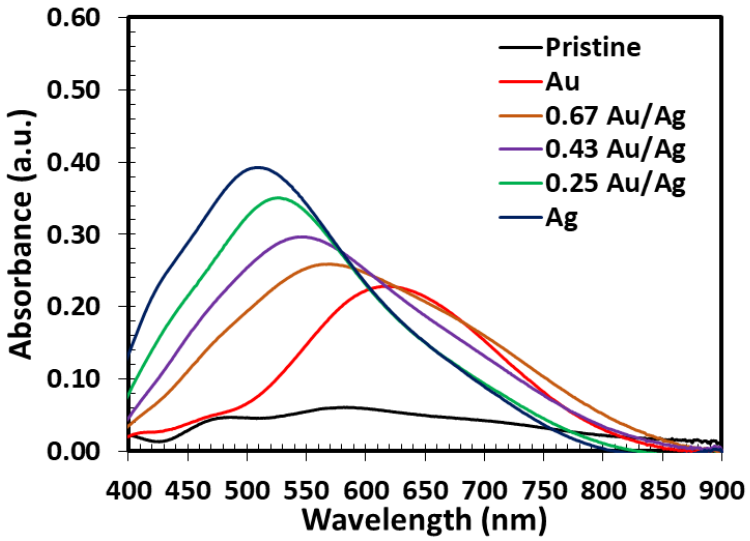


**Figure 27.** Absorption spectra of pristine ZnO, Au NPs/ ZnO, 0.67 Au/Ag BNPs/ ZnO, 0.43 Au/Ag BNPs/ ZnO, 0.25 Au/Ag BNPs/ ZnO, and Ag NPs/ ZnO.

5.3.4 Charge Transfer by photoluminescence (PL) spectroscopy:

PL measurements were performed to study the rate of electrical charge generation, separation, and transfer of the Au/Ag-ZnO photo-anodes containing BNPs with different $C_{Au/Ag}$ as shown in Figure 28. All the spectra revealed two emission bands located at the UV region and the visible region. During photo-excitation with energy equivalent or greater than the band gap of ZnO, the electrons in the valence band were excited to the conduction band, whereby the electrons can be separated from the holes or undergo recombination process with the holes. The distinct UV emission band (385 nm) has been commonly attributed to the excitons (electron-hole pairs) emission band which is due to the radiative recombination of excitons, while the broad visible band (peaked at 585 nm) ranges from 500 to 600 nm has been assigned to the recombination of photo-generated holes originated from intrinsic defects such as oxygen vacancies and Zinc interstitial [155]. The increased in PL intensity of the UV region can be attributed to the increased generation of excitons, which indicates more electron-hole pairs are available for the separation process during photo-excitation. On the other hand, the increased in PL of the visible region are commonly associated with the increased recombination of electrons, suggesting that more surface defects or trap sites were present which prevent the separation of excitons, hence potentially leading to poor photo-activity performance. Therefore, it is crucial to achieve a high UV emission, as well as maintaining a low visible emission for enhanced PEC performance. Based on Figure 28, it can be observed that 0.25 Au/Ag BNPs exhibited the lowest visible emission to UV emission ratio of 0.14. This can be explained by the results from UV-Vis spectroscopy and nanoscale electrical characterization which indicated that 0.25 Au/Ag BNPs exhibited broaden and enhanced photo absorption spectra, as well as the formation of a suitable Schottky barrier with ZnO that prevent the recombination of electrons. This suggests that integration of optimal $C_{Au/Ag}$ is capable

of increasing the generated excitons, as well as resulting in the reduction of the recombination of excitons. In order to determine the photo-activity, PEC measurements such as chronoamperometry (CA), linear sweep voltammetry (LSV), as well as electrochemical impedance spectroscopy (EIS) were further conducted.

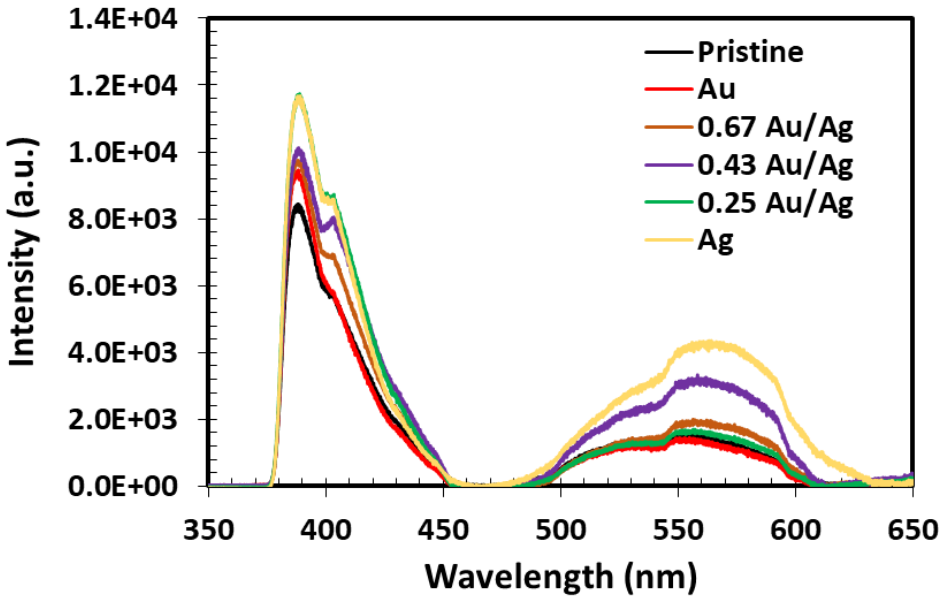


**Figure 28.** Steady-state photoluminescence spectroscopy of pristine ZnO, Au NPs/ ZnO, 0.67 Au/Ag BNPs/ ZnO, 0.43 Au/Ag BNPs/ ZnO, 0.25 Au/Ag BNPs/ ZnO, and Ag NPs/ ZnO.

## 5.4 Phase 4: Photoelectrochemical (PEC) Measurement of Au/Ag BNPs/ ZnO/ FTO

### 5.4.1 Chronoamperometry (CA)

The photo-activity of the synthesized ZnO photo-anode versus time has been measured under AM1.5 and visible illumination as shown in Figure 29(a) and Figure 29(b), respectively, using a CA technique in a fixed anodic bias of V=0.4 V. The measured photo-current was stable

over time as shown in Figure S9, which indicated that photo-generated holes are in close contact with electrolyte, thus resulting in efficient water oxidation reaction. Wavelength encompassing the visible and UV-Vis region were utilized, namely visible and AM1.5 filters, to study the photo-excitation of Au/Ag BNPs, as well as both Au/Ag BNPs and ZnO, respectively. Under AM1.5 illumination, integration of NPs to the ZnO resulted in the increased of photocurrent density, with 0.25 Au/Ag-ZnO exhibiting the highest increased in photocurrent density from 4.0 uA $cm^{-2}$ (pristine ZnO) to 7.3 uA $cm^{-2}$ as shown in Figure 29(a), which indicates an enhancement of approximately 80%. Meanwhile, under visible illumination, 0.25 Au/Ag-ZnO also displayed the highest photocurrent density as compared to the other photo-anodes, while pristine ZnO exhibited zero photocurrent density as shown in Figure 29(b). This indicates that integration of 0.25 Au/Ag BNPs have extended and enhanced the photocurrent of the photo-anodes into the visible region due to the LSPR effect.

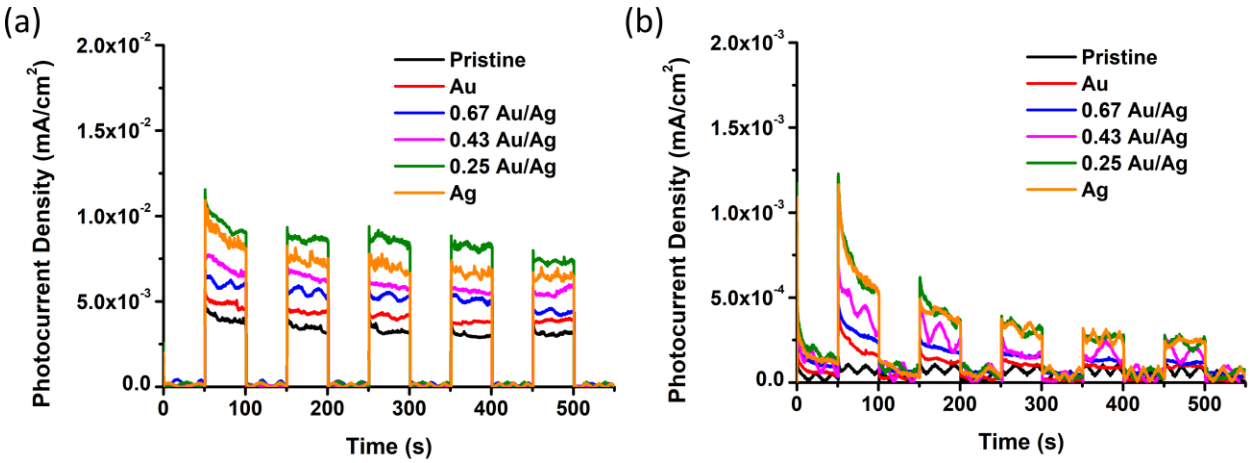


**Figure 29.** Chronoamperometry (CA) under (a) AM1.5 and (b) visible illumination. All measurements were recorded in 0.5 M $Na_2CO_3$ electrolyte solution under 1 Sun illumination (with an intensity of 100 $mW/cm^2$). Pristine indicates ZnO without NPs.

5.4.2 Linear sweep voltammetry (LSV)

Figure 30(a) and Figure 30(b) shows the LSV under AM1.5 and visible illumination, respectively. In regards to this, 0.25 Au/Ag-ZnO resulted in a significant increase of approximately 4.7 and 2.2 factors (at 1.0V vs Ag/AgCl) as compared to Au-ZnO and Ag-ZnO, respectively. In this case, the role of NPs is to facilitate charge transfer to the semiconductor which eventually resulted in an enhanced photocurrent. Both the combination of Au and Ag in BNPs increases the electron density around the ZnO photo-anode and the SPR-excited form of bi-metals enhances the electron transfer from BNPs to the ZnO semiconductor. These results are in accordance to the electrical conduction shown in Figure 19.

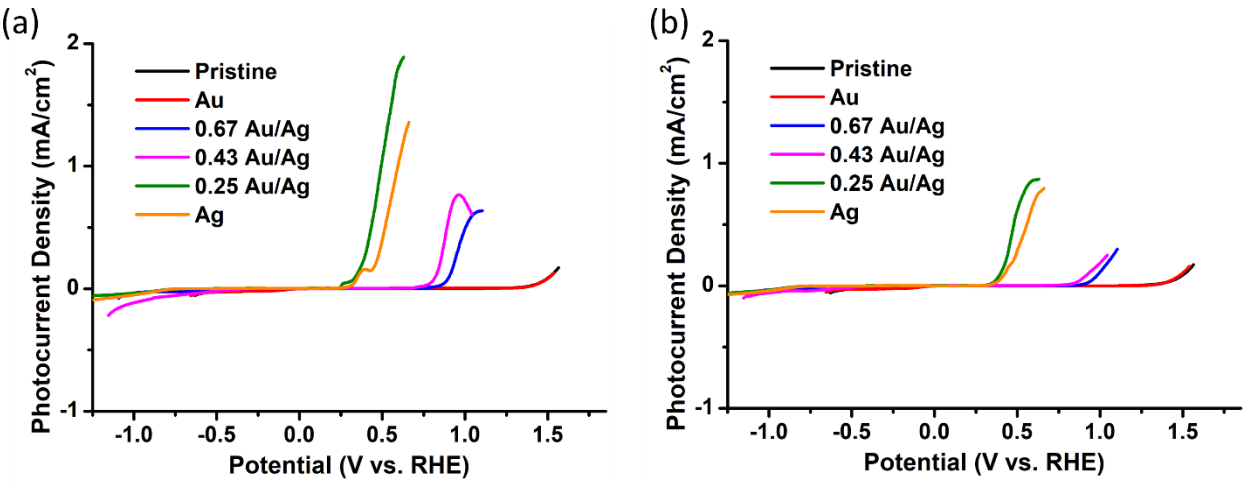


**Figure 30.** Linear sweep voltammetry (LSV) under light with (a) AM1.5 and (b) visible illumination. All measurements were recorded in 0.5 M $Na_2CO_3$ electrolyte solution under 1 Sun illumination (with an intensity of 100 mW/cm$^2$). Pristine indicates ZnO without NPs.

5.4.3 Electrochemical impedance spectroscopy (EIS)

In addition to that, EIS is a powerful method for studying electrode charge transfer properties. EIS measurement exhibited single arc which suggest that surface charge transfer is the sole process occurring and the arc diameter is inversely proportional to the charge separation of charge carriers. In this case, 0.25 Au/Ag-ZnO exhibited the smallest arc diameter among the synthesized photo-anodes as shown in Figure 31(a) and Figure 31(b) under AM1.5 and visible illumination, respectively. The smaller arc gives lower impedance, therefore fast interfacial charge transport with effective charge separation and longer charge carrier lifetime, thus reduce charge recombination rate. This leads to higher photocurrent generation as shown in the CA and LSV results in Figure 29 and Figure 30, respectively. The corresponding circuit model of charge transfer in the BNPs-ZnO photo-anodes is shown in Figure 32. Constant phase element (CPE) was utilized to better analyse the data on account of the non-ideal capacitance (C) behaviour of the nanostructure surface of the metal nanoparticles and ZnO. In the correspondent circuit model, $R_1$ represents the solution resistance. $R_2$ and $C_1$ are the charge transfer resistance and capacitance of 0.25 Au/Ag BNPs, respectively. $R_3$ and $CPE_1$ are the charge transfer resistance and constant phase element (CPE) of the particle spacing within the BNPs, respectively. Meanwhile, $R_4$ and $CPE_2$ are the charge transfer resistance and constant phase element of ZnO, respectively. The fitting results obtained from the EIS measurement were presented in Table S5. By corroborating the UV-Vis absorption, KPFM, CAFM, PL, as well as the PEC results, the high photo-activity of 0.25 Au/Ag-ZnO was contributed by the combination of: (i) optimal $C_{Au/Ag}$ increases the electrical conduction and broaden the LSPR wavelength, (ii) the tunability of the Schottky barrier which improves electron-hole pair separation rate, and (iii) the high charge transfer efficiency at the interface

between the sample and electrolyte. The proposed mechanism will be highlighted in the next section to further understand the enhancement mechanism behind Au/Ag BNPs.

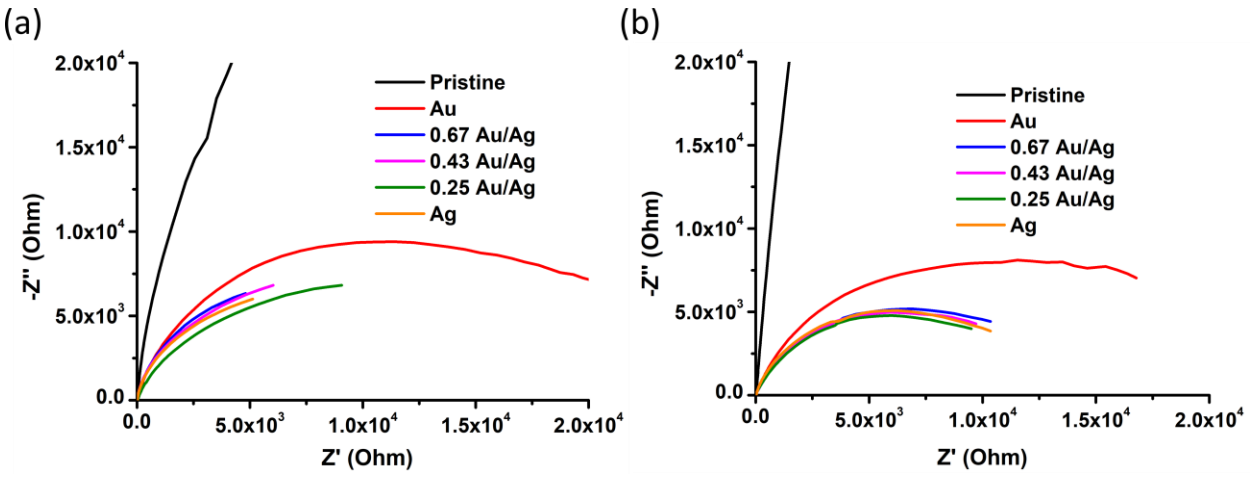


**Figure 31.** Electrochemical impedance spectroscopy (EIS) under light with (a) AM1.5 and (b) visible illumination. All measurements were recorded in 0.5 M $Na_2CO_3$ electrolyte solution under 1 Sun illumination (with an intensity of 100 mW/cm$^2$). Pristine indicates ZnO without NPs.

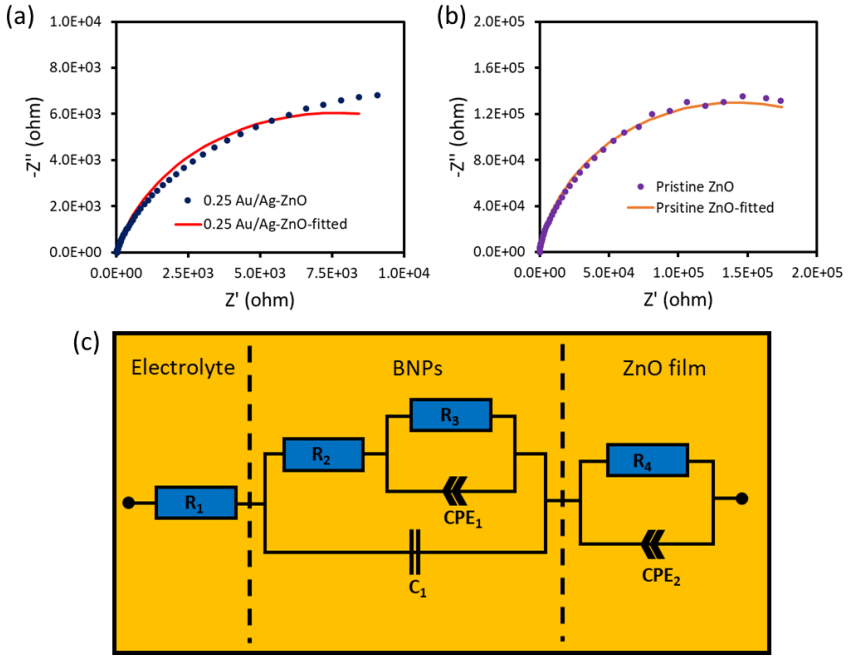


**Figure 32.** Nyquist plot of (a) 0.25 Au/Ag-ZnO and (b) pristine ZnO with the fitted equivalent circuit; (c) Equivalent circuit model of the photo-anodes.

The performance of the ZnO photoanodes can also be quantitatively determined through the efficiency of converting photon energy to chemical energy, which is commonly known as photoconversion efficiency. By utilizing the LSV data in Figure 30(a), the photoconversion efficiency, $\eta$ of the photoanodes can be estimated from the expression: $\eta = \left[I_j \times (V_{rev} - |V_{bias}|)\right]/P_{light}$,[156] where $I_j$ is the photocurrent density (mA/cm$^2$), $V_{rev}$ is the standard state-reversible potential (which is 1.23 V versus normal hydrogen electrode (NHE)), $P_{light}$ is the incident power density (100 mW/cm$^2$), and $V_{bias}$ is the applied potential. The $V_{bias}$ can be expressed as $V_{bias} = V_{mea} - V_{voc}$, where $V_{mea}$ is the potential of working electrode (versus reversible hydrogen electrode (RHE)) at which photocurrent is measured under illumination and $V_{voc}$ is the potential of working electrode (versus RHE) measured under the same irradiation under open-circuit conditions. Based on Figure 33, under AM 1.5G illumination the obtained maximum $\eta$ of 0.25 Au/Ag-ZnO was approximately 0.033 % at 0.3 V (versus RHE), which is much higher than the values on pristine ZnO (0.005 %), Au-ZnO (0.013 %) and Ag-ZnO (0.023 %). It is worthy to note that the calculated photoconversion efficiency can only be used as an approximation on the performance of the individual photoanodes, and not the overall PEC cell performance. Nevertheless, incorporation of 0.25 Au/Ag BNPs on the ZnO photoanodes demonstrated the highest photoconversion efficiency which is in agreement with the CA measurements shown in Figure 29.

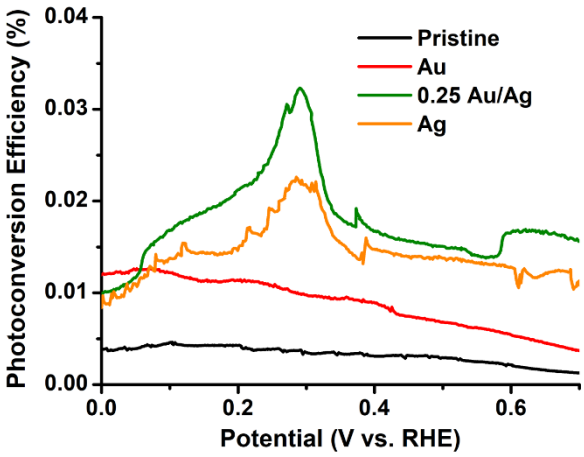


**Figure 33.** Photoconversion efficiency against applied potential curves for 0.25 Au/Ag, Au NPs, Ag NPs and pristine ZnO photoanode.

5.4.4 Proposed Mechanism

The proposed mechanism of Au/Ag BNPs integrated on ZnO based photoanode was shown in Figure 34. Figure 34(a) shows that valence electrons are excited from the valence band ($E_{VB}$) to the conductance band ($E_{CB}$) of ZnO upon UV illumination. However, when Au/Ag BNPs were deposited on ZnO, electron transfer from both Au and Ag to ZnO occurred until the whole system reach Fermi equilibrium due to the redistribution of the free electrons across the Au/Ag BNPs-ZnO interface, thereby forming a Schottky barrier. In this case, the Schottky barrier exhibited a downward bending characteristic as the Fermi level of ZnO is located below than that of Au and Ag because of ZnO (5.2 eV) having a larger work function than Au (5.1 eV) and Ag (4.6 eV). Subsequently, the photo-generated electrons move freely from the $E_{CB}$ to Au or Ag because the newly-shifted $E_{CB}$ is located higher than the Fermi energy level upon reaching Fermi equilibrium as shown in Figure 34(b). As pointed out on the basis of Figure 21(d)-(f), $V_{CPD}$ of the NPs demonstrated relative Schottky barrier height ($E_{SBH}$) tuning at the interface; for instance, the $V_{CPD}$

of 0.25 Au/Ag BNPs has been decreased to -99.16 mV as compared to -245.90 mV (Au NPs) and -118.88 mV (Ag NPs). As a result, an increased in $e^-$- $h^+$ pairs separation and transfer were observed via EIS characterization as shown in Figure 31(a) and Figure 31(b). In addition to the electrical tuning by Au/Ag BNPs, absorption spectra demonstrated tuning of the LSPR peaks in the visible region as shown in Figure 16(a). From this point of view, upon visible illumination, the surface plasmon of Au/Ag BNPs are excited (Figure 34(c)) and the highly energized electrons are injected back into the $E_{CB}$ to be extracted by the electrode as shown in Figure 34(d). However, due to the lowest $E_{SBH}$ exhibited by 0.25 Au/Ag BNPs, more excited electrons with energy greater than the $E_{SBH}$ are generated as shown in the CA plots in Figure 29(a) and Figure 29(b). Furthermore, the charge transfer improvement are also influenced by the conduction of electrons across the NPs as indicated by the LSV in Figure 30(a) and Figure 30(d). These results supported the improvement of charge transfer via increased $e^-$- $h^+$ pairs separation and enhanced visible light SPR effect by integrating 0.25 Au/Ag BNPs on the ZnO photo-anodes. With all of the above findings, the effect of composition ratio of Au/Ag BNPs on the overall electrical and optical properties on Photoelectrochemical performance was established.

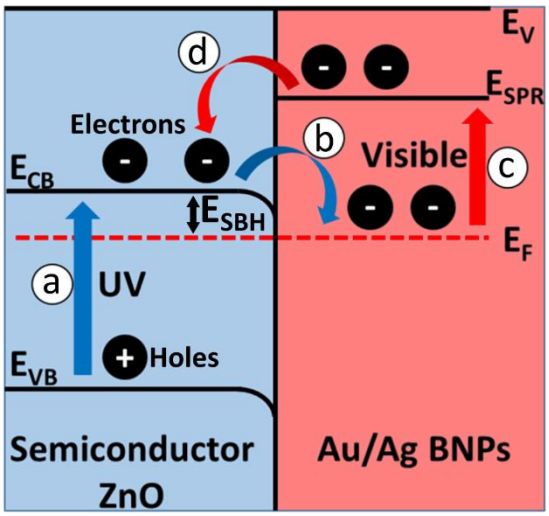

**Figure 34.** Electron flow between ZnO and Au/Ag BNPs upon illumination. Upon UV illumination, (a) electrons are excited from the valence band ($E_{VB}$) to conductance band ($E_{CB}$) and, subsequently, (b) ease of transfer to the Au/Ag BNPs without requiring extra energy as the Fermi level ($E_F$) is located below the $E_{CB}$, which resulted in suppressed charge recombination. Upon visible illumination, (c) localized surface plasmon resonance phenomena results in energized electron clouds at the NPs surface. (d) The energized electrons are then injected to the $E_{CB}$ of ZnO.

# Chapter 6 Conclusion

In conclusion, this study explored the facile solid-state fabrication method of Au/Ag BNPs via solid-state thermal dewetting method and their contribution of plasmon-induced charge separation and electrical conduction in plasmonic applications. To ensure the complete formation of nanoparticles, Au and Ag are investigated individually and the ideal annealing temperature is determined to be 300 $^{o}$C. The optical, electrical and PEC properties of the Au/Ag BNPs were systematically characterized by tuning the compositional ratio. In regards to this, 0.25 Au/Ag BNPs was found to exhibit enhanced electrical and optical properties as compared to other MNPs and BNPs. It was observed that Au and Ag elements are uniformly distributed in the BNPs, forming an alloyed nanostructure as indicated by HRTEM-EDS mapping. The SPR peak of the BNPs exhibited a blue shift as the Ag composition ratio increase and a broad absorbance enhancement spectra width in visible light spectrum from 451 nm to 614 nm which encompasses the spectra width of monometallic Au NPs and Ag NPs was observed. This can be attributed to the Au and Ag elements being uniformly distributed in the BNPs, forming an alloyed nanostructure as indicated by HRSTEM-EDS mapping. To validate the plasmonic performance, SERS of Congo

red molecules indicate that 0.25 Au/Ag BNPs has the highest enhancement factor of 1.60 x $10^7$ and exhibited high sensitivity of Rhodamine B molecules with low concentration of 0.1 mg/L. In terms of electrical conduction, KPFM and CAFM displayed the lowest contact potential difference of -99.157 mV and highest drift current of 507 pA, indicating efficient charge transport by 0.25 Au/Ag BNPs due to the lowered Schottky barrier height. PEC measurement shows improvement of photocurrent density, enhanced charge transfer and reduction in resistance indicated by CA, LSV and EIS, respectively. The enhancement in PEC can be mainly attributed to enhanced photo absorption and charge carrier separation due to LSPR and hot electron injection. This study suggests that optimized Au/Ag composition ratio of BNPs is able to exploit the enhanced electrical conduction and LSPR, leading to improved charge carrier separation and photon absorption upon photon excitation in PEC and SERS application.

# Chapter 7 Recommendation for Future Work:

According to the findings of this research, there are tremendous potential and development that could be observed in this field. Based on the findings in this thesis, it was determined that the formation of Au/Ag BNPs with optimized composition ratio can significantly enhance the plasmonic performance of applications such as SERS and PEC water splitting. Thus, the future work of this research would emphasize on the real-life applications to achieve potential industrial and commercial application.

The stability of the developed BNPs is one of the most concern aspects in an industrial and commercial applications. The present SERS and PEC experimental works were conducted using prepared dye solution and 0.5M $Na_2CO_3$ buffer solution, respectively. However, real life application of SERS and PEC are commonly performed using contaminated water that often contains various organic compounds and saltwater, respectively. Therefore, it is crucial to conduct the experiment in contaminated water and saltwater to observe the effect of water quality towards the SERS and PEC performance, respectively.

In addition, it is of paramount importance the developed BNPs are photoactive and correspond well with the photon spectrum of direct natural sunlight. In this current work, the PEC

water splitting experiments were performed using of a Xenon arc lamp coupled with an AM 1.5 filter to simulate the photon spectrum of sunlight. Thus, natural sunlight could be employed in the PEC experiment to improve the significance of this research. Furthermore, other crucial PEC water splitting reaction parameters, such as reaction temperature and pH should be carried out for the future work to fully understand the contribution by the BNPs.

Finally, the properties of the materials used in BNPs are important in determining the enhancement efficiency in SERS and PEC water splitting. Hence, the research and development of new materials should be conducted to improve the optical and electrical properties. The full understanding of the design and fabrication method, as well as research based on theoretical calculations would be beneficial in exploring these new materials of BNPs.

# REFERENCE


1. Gibson, M.I., M. Danial, and H.-A. Klok, *Sequentially Modified, Polymer-Stabilized Gold Nanoparticle Libraries: Convergent Synthesis and Aggregation Behavior.* ACS Combinatorial Science, 2011. **13**(3): p. 286-297.
2. Mallin, M.P. and C.J. Murphy, *Solution-Phase Synthesis of Sub-10 nm Au−Ag Alloy Nanoparticles.* Nano Letters, 2002. **2**(11): p. 1235-1237.
3. Sun, L., W. Luan, and Y.J. Shan, *A composition and size controllable approach for Au-Ag alloy nanoparticles.* Nanoscale Research Letters, 2012. **7**(1): p. 225.
4. Liu, S., et al., *Synthesis of Monodisperse Au, Ag, and Au–Ag Alloy Nanoparticles with Tunable Size and Surface Plasmon Resonance Frequency.* Chemistry of Materials, 2011. **23**(18): p. 4098-4101.
5. Nishijima, Y. and S. Akiyama, *Unusual optical properties of the Au/Ag alloy at the matching mole fraction.* Optical Materials Express, 2012. **2**(9): p. 1226-1235.
6. Shah, A., et al., *Synthesis, characterization, and application of Au–Ag alloy nanoparticles for the sensing of an environmental toxin, pyrene.* Journal of Applied Electrochemistry, 2015. **45**(5): p. 463-472.
7. Musick, M.D., et al., *Electrochemical properties of colloidal Au-based surfaces: Multilayer assemblies and seeded colloid films.* Langmuir, 1999. **15**(3): p. 844-850.
8. Brown, K.R., et al., *Hydroxylamine seeding of colloidal Au nanoparticles. 3. Controlled formation of conductive Au films.* Chemistry of Materials, 2000. **12**(2): p. 314-323.
9. Valenti, M., et al., *The Role of Size and Dimerization of Decorating Plasmonic Silver Nanoparticles on the Photoelectrochemical Solar Water Splitting Performance of BiVO4 Photoanodes.* ChemNanoMat, 2016. **2**(7): p. 739-747.
10. Tan, K.H., et al., *Self-Assembled Heteroepitaxial AuNPs/SrTiO3: Influence of AuNPs Size on SrTiO3 Band Gap Tuning for Visible Light-Driven Photocatalyst.* The Journal of Physical Chemistry C, 2017. **121**(25): p. 13487-13495.
11. Wang, N., T. Tachikawa, and T. Majima, *Single-molecule, single-particle observation of size-dependent photocatalytic activity in Au/TiO2 nanocomposites.* Chemical Science, 2011. **2**(5): p. 891-900.
12. Kozanoglu, D., et al., *Power conversion efficiency enhancement of organic solar cells by addition of gold nanostars, nanorods, and nanospheres.* Organic Electronics, 2013. **14**(7): p. 1720-1727.
13. Ng, A., et al., *Enhanced Performance of PTB7:PC71BM Solar Cells via Different Morphologies of Gold Nanoparticles.* ACS Applied Materials & Interfaces, 2014. **6**(23): p. 20676-20684.
14. Heo, M., et al., *High-Performance Organic Optoelectronic Devices Enhanced by Surface Plasmon Resonance.* Advanced Materials, 2011. **23**(47): p. 5689-5693.
15. Kim, K. and D.L. Carroll, *Roles of Au and Ag nanoparticles in efficiency enhancement of poly(3-octylthiophene)/C60 bulk heterojunction photovoltaic devices.* Applied Physics Letters, 2005. **87**(20): p. 203113.
16. Perdikaki, A., et al., *Ag and Cu Monometallic and Ag/Cu Bimetallic Nanoparticle–Graphene Composites with Enhanced Antibacterial Performance.* ACS Applied Materials & Interfaces, 2016. **8**(41): p. 27498-27510.

17. Jana, N.R., L. Gearheart, and C.J. Murphy, *Wet chemical synthesis of high aspect ratio cylindrical gold nanorods.* The Journal of Physical Chemistry B, 2001. **105**(19): p. 4065-4067.
18. Sau, T.K. and C.J. Murphy, *Room temperature, high-yield synthesis of multiple shapes of gold nanoparticles in aqueous solution.* Journal of the American Chemical Society, 2004. **126**(28): p. 8648-8649.
19. Demortiere, A., et al., *Shape-controlled platinum nanocubes and their assembly into two-dimensional and three-dimensional superlattices.* The Journal of Physical Chemistry B, 2008. **112**(46): p. 14583-14592.
20. Skrabalak, S.E., et al., *Facile synthesis of Ag nanocubes and Au nanocages.* Nature protocols, 2007. **2**(9): p. 2182-2190.
21. Sau, T.K. and C.J. Murphy, *Seeded high yield synthesis of short Au nanorods in aqueous solution.* Langmuir, 2004. **20**(15): p. 6414-6420.
22. Chen, H.M., et al., *Synthesis and characterization of multi-pod-shaped gold/silver nanostructures.* The Journal of Physical Chemistry C, 2007. **111**(16): p. 5909-5914.
23. Kuo, C.-H. and M.H. Huang, *Synthesis of branched gold nanocrystals by a seeding growth approach.* Langmuir, 2005. **21**(5): p. 2012-2016.
24. Joo, S.H., et al., *Thermally stable Pt/mesoporous silica core–shell nanocatalysts for high-temperature reactions.* Nature materials, 2009. **8**(2): p. 126-131.
25. Mallik, K., et al., *Seed Mediated Formation of Bimetallic Nanoparticles by UV Irradiation: A Photochemical Approach for the Preparation of "Core−Shell" Type Structures.* Nano Letters, 2001. **1**(6): p. 319-322.
26. Haldar, K.K., S. Kundu, and A. Patra, *Core-Size-Dependent Catalytic Properties of Bimetallic Au/Ag Core–Shell Nanoparticles.* ACS Applied Materials & Interfaces, 2014. **6**(24): p. 21946-21953.
27. Dolgaev, S., et al., *Nanoparticles produced by laser ablation of solids in liquid environment.* Applied surface science, 2002. **186**(1): p. 546-551.
28. Yan, Z. and D.B. Chrisey, *Pulsed laser ablation in liquid for micro-/nanostructure generation.* Journal of Photochemistry and Photobiology C: Photochemistry Reviews, 2012. **13**(3): p. 204-223.
29. Kazakevich, P., et al., *Laser induced synthesis of nanoparticles in liquids.* Applied Surface Science, 2006. **252**(13): p. 4373-4380.
30. Henley, S., J. Carey, and S. Silva, *Pulsed-laser-induced nanoscale island formation in thin metal-on-oxide films.* Physical Review B, 2005. **72**(19): p. 195408.
31. Trice, J., et al., *Pulsed-laser-induced dewetting in nanoscopic metal films: Theory and experiments.* Physical Review B, 2007. **75**(23): p. 235439.
32. Ruffino, F., et al., *Formation and evolution of nanoscale metal structures on ITO surface by nanosecond laser irradiations of thin Au and Ag films.* Science of Advanced Materials, 2012. **4**(7): p. 708-718.
33. Nikov, R.G., et al., *Characterization of Ag nanostructures fabricated by laser-induced dewetting of thin films.* Applied Surface Science, 2016. **374**: p. 36-41.
34. Ruffino, F., et al., *Rayleigh-instability-driven dewetting of thin Au and Ag films on indium–tin-oxide surface under nanosecond laser irradiations.* Micro & Nano Letters, 2013. **8**(3): p. 127-130.
35. Oh, Y. and M. Lee, *Single-pulse transformation of Ag thin film into nanoparticles via laser-induced dewetting.* Applied Surface Science, 2017. **399**(Supplement C): p. 555-564.

36. Ruffino, F., et al., *Size-selected Au nanoparticles on FTO substrate: Controlled synthesis by the Rayleigh-Taylor instability and optical properties.* Superlattices and Microstructures, 2016. **100**(Supplement C): p. 418-430.
37. Maier, S.A., et al., *Plasmonics—a route to nanoscale optical devices.* Advanced Materials, 2001. **13**(19): p. 1501-1505.
38. Cen, X., A.M. Thron, and K. van Benthem, *In-situ study of the dewetting behavior of Au/Ni bilayer films supported by a SiO2/Si substrate.* Acta Materialia, 2017. **140**(Supplement C): p. 149-156.
39. Lian, J., et al., *Patterning metallic nanostructures by ion-beam-induced dewetting and Rayleigh instability.* Nano Letters, 2006. **6**(5): p. 1047-1052.
40. Kojima, Y. and T. Kato, *Nanoparticle formation in Au thin films by electron-beam-induced dewetting.* Nanotechnology, 2008. **19**(25): p. 255605.
41. Giermann, A.L. and C.V. Thompson, *Solid-state dewetting for ordered arrays of crystallographically oriented metal particles.* Applied physics letters, 2005. **86**(12): p. 121903.
42. Wang, D. and P. Schaaf, *Ni–Au bi-metallic nanoparticles formed via dewetting.* Materials Letters, 2012. **70**: p. 30-33.
43. Petersen, J. and S. Mayr, *Dewetting of Ni and NiAg solid thin films and formation of nanowires on ripple patterned substrates.* Journal of Applied Physics, 2008. **103**(2): p. 023520.
44. Andres, C., et al., *9.4% efficient Cu2ZnSnSe4 solar cells from co-sputtered elemental metal precursor and rapid thermal annealing.* Thin Solid Films, 2017. **633**(Supplement C): p. 141-145.
45. Ruffino, F., et al., *Nanoporous Au structures by dealloying Au/Ag thermal- or laser-dewetted bilayers on surfaces.* Superlattices and Microstructures, 2017. **103**(Supplement C): p. 28-47.
46. Müller, C.M. and R. Spolenak, *Dewetting of Au and AuPt alloy films: A dewetting zone model.* Journal of Applied Physics, 2013. **113**(9): p. 094301.
47. Amram, D., L. Klinger, and E. Rabkin, *Anisotropic hole growth during solid-state dewetting of single-crystal Au–Fe thin films.* Acta Materialia, 2012. **60**(6): p. 3047-3056.
48. De Monestrol, H., et al., *Kinetics and mechanisms of reactive solid state dewetting in the system Ag–Ni–O.* Acta materialia, 2001. **49**(9): p. 1655-1660.
49. Benkouider, A., et al., *Ordered arrays of Au catalysts by FIB assisted heterogeneous dewetting.* Nanotechnology, 2015. **26**(50): p. 505602.
50. Araújo, A., et al., *Influence of the Substrate on the Morphology of Self-Assembled Silver Nanoparticles by Rapid Thermal Annealing.* The Journal of Physical Chemistry C, 2016. **120**(32): p. 18235-18242.
51. Ruffino, F., *Experimental Analysis on the Molten-Phase Dewetting Characteristics of AuPd Alloy Films on Topographically-Structured Substrates.* Metals, 2017. **7**(9): p. 327.
52. Herz, A., et al., *Solid-state dewetting of single-and bilayer Au-W thin films: Unraveling the role of individual layer thickness, stacking sequence and oxidation on morphology evolution.* AIP Advances, 2016. **6**(3): p. 035109.
53. Seo, O., et al., *Controlling the alloy composition of PtNi nanocrystals using solid-state dewetting of bilayer films.* Journal of Alloys and Compounds, 2016. **667**(Supplement C): p. 141-145.

54. Wolcott, A., et al., *Photoelectrochemical study of nanostructured ZnO thin films for hydrogen generation from water splitting.* Advanced Functional Materials, 2009. **19**(12): p. 1849-1856.
55. Yang, X., et al., *Nitrogen-doped ZnO nanowire arrays for photoelectrochemical water splitting.* Nano letters, 2009. **9**(6): p. 2331-2336.
56. Chen, X. and S.S. Mao, *Synthesis of titanium dioxide (TiO2) nanomaterials.* Journal of nanoscience and nanotechnology, 2006. **6**(4): p. 906-925.
57. Nowotny, J., et al., *Titanium dioxide for solar-hydrogen I. Functional properties.* International journal of hydrogen energy, 2007. **32**(14): p. 2609-2629.
58. Fujishima, A., X. Zhang, and D.A. Tryk, *TiO2 photocatalysis and related surface phenomena.* Surface science reports, 2008. **63**(12): p. 515-582.
59. Su, J., et al., *Vertically aligned WO3 nanowire arrays grown directly on transparent conducting oxide coated glass: synthesis and photoelectrochemical properties.* Nano letters, 2011. **11**(1): p. 203-208.
60. Gonçalves, R.H., L.D. Leite, and E.R. Leite, *Colloidal WO3 nanowires as a versatile route to prepare a photoanode for solar water splitting.* ChemSusChem, 2012. **5**(12): p. 2341-2347.
61. Wang, G., et al., *Hydrogen-treated WO3 nanoflakes show enhanced photostability.* Energy & Environmental Science, 2012. **5**(3): p. 6180-6187.
62. Le Formal, F., M. Grätzel, and K. Sivula, *Controlling photoactivity in ultrathin hematite films for solar water-splitting.* Advanced Functional Materials, 2010. **20**(7): p. 1099-1107.
63. Sivula, K., et al., *Photoelectrochemical water splitting with mesoporous hematite prepared by a solution-based colloidal approach.* Journal of the American Chemical Society, 2010. **132**(21): p. 7436-7444.
64. Tilley, S.D., et al., *Light-induced water splitting with hematite: improved nanostructure and iridium oxide catalysis.* Angewandte Chemie International Edition, 2010. **49**(36): p. 6405-6408.
65. Kay, A., I. Cesar, and M. Grätzel, *New benchmark for water photooxidation by nanostructured α-Fe2O3 films.* Journal of the American Chemical Society, 2006. **128**(49): p. 15714-15721.
66. Wang, B.-S., et al., *An overlapping ZnO nanowire photoanode for photoelectrochemical water splitting.* Catalysis Today, 2019. **321-322**: p. 100-106.
67. Marlinda, A.R., et al., *Tailoring morphological characteristics of zinc oxide using a one-step hydrothermal method for photoelectrochemical water splitting application.* International Journal of Hydrogen Energy, 2019. **44**(33): p. 17535-17543.
68. Commandeur, D., et al., *Defect-rich ZnO nanorod arrays for efficient solar water splitting.* ACS Applied Nano Materials, 2019. **2**(3): p. 1570-1578.
69. Wang, M., et al., *N Doping to ZnO Nanorods for Photoelectrochemical Water Splitting under Visible Light: Engineered Impurity Distribution and Terraced Band Structure.* Scientific Reports, 2015. **5**(1): p. 12925.
70. Aboud, A.A., M. Shaban, and N. Revaprasadu, *Effect of Cu, Ni and Pb doping on the photo-electrochemical activity of ZnO thin films.* RSC Advances, 2019. **9**(14): p. 7729-7736.

71. Sreedhar, A., et al., *Insight into anions and cations effect on charge carrier generation and transportation of flake-like Co-doped ZnO thin films for stable PEC water splitting activity.* Journal of Electroanalytical Chemistry, 2019. **855**: p. 113583.
72. Wen, P., et al., *A highly active three-dimensional Z-scheme ZnO/Au/g-C3N4 photocathode for efficient photoelectrochemical water splitting.* Applied Catalysis B: Environmental, 2020. **263**: p. 118180.
73. Zhou, T., et al., *Bird-nest structured ZnO/TiO2 as a direct Z-scheme photoanode with enhanced light harvesting and carriers kinetics for highly efficient and stable photoelectrochemical water splitting.* Applied Catalysis B: Environmental, 2020. **267**: p. 118599.
74. Hassan, M.A., et al., *Single-step fabrication of 3D hierarchical ZnO/ZnS heterojunction branched nanowires by MOCVD for enhanced photoelectrochemical water splitting.* Journal of Materials Chemistry A, 2020. **8**(17): p. 8300-8312.
75. Ziashahabi, A., et al., *The effect of silver oxidation on the photocatalytic activity of Ag/ZnO hybrid plasmonic/metal-oxide nanostructures under visible light and in the dark.* Scientific reports, 2019. **9**(1): p. 1-12.
76. Liu, L., et al., *Three-dimensional plasmonic photoanode of Au nanoparticles/ZnFe2O4 nanosheets coated onto ZnO nanotube arrays for photoelectrochemical production of hydrogen.* Solar Energy Materials and Solar Cells, 2019. **195**: p. 330-338.
77. Kavitha, R., S. Girish Kumar, and C.G. Sushma, *Plasmonic Ag-ZnO: Charge Carrier Mechanisms and Photocatalytic Applications.* Photocatalytic Functional Materials for Environmental Remediation, 2019: p. 191-214.
78. Güy, N. and M. Özacar, *Ag/Ag2CrO4 nanoparticles modified on ZnO nanorods as an efficient plasmonic photocatalyst under visible light.* Journal of Photochemistry and Photobiology A: Chemistry, 2019. **370**: p. 1-11.
79. Wang, Z.-j., et al., *Photo-assisted methanol synthesis via CO2 reduction under ambient pressure over plasmonic Cu/ZnO catalysts.* Applied Catalysis B: Environmental, 2019. **250**: p. 10-16.
80. Nguyen, P.D., T.M. Duong, and P.D. Tran, *Current progress and challenges in engineering viable artificial leaf for solar water splitting.* Journal of Science: Advanced Materials and Devices, 2017. **2**(4): p. 399-417.
81. Chiu, Y.-H., et al., *Mechanistic insights into photodegradation of organic dyes using heterostructure photocatalysts.* Catalysts, 2019. **9**(5): p. 430.
82. Chiu, Y.-H., et al., *Photoelectrochemical cells for solar hydrogen production: Challenges and opportunities.* APL Materials, 2019. **7**(8): p. 080901.
83. Fang, M.-J., C.-W. Tsao, and Y.-J. Hsu, *Semiconductor nanoheterostructures for photoconversion applications.* Journal of Physics D: Applied Physics, 2020. **53**(14): p. 143001.
84. Tamirat, A.G., et al., *Using hematite for photoelectrochemical water splitting: a review of current progress and challenges.* Nanoscale Horizons, 2016. **1**(4): p. 243-267.
85. Huang, Z., et al., *Nanomaterial-based SERS sensing technology for biomedical application.* Journal of Materials Chemistry B, 2019. **7**(24): p. 3755-3774.
86. Zhu, W., et al., *Monodispersed Plasmonic Prussian Blue Nanoparticles for Zero-background SERS/MRI-guided Phototherapy.* Nanoscale, 2020.

87. Nowak, M., et al., *Preparation and characterization of long-term stable SERS active materials as potential supports for medical diagnostic.* Applied Surface Science, 2019. **472**: p. 93-98.
88. Park, J.E., et al., *Plasmonic Microneedle Arrays for in Situ Sensing with Surface-Enhanced Raman Spectroscopy (SERS).* Nano Letters, 2019. **19**(10): p. 6862-6868.
89. Ran, Y., et al., *Fiber-optrode SERS probes using plasmonic silver-coated gold nanostars.* Sensors and Actuators B: Chemical, 2019. **287**: p. 95-101.
90. Ghosh, P., et al., *Directed Microwave-Assisted Self-Assembly of Au–Graphene–Au Plasmonic Dimers for SERS Applications.* Advanced Materials Interfaces, 2019. **6**(18): p. 1900629.
91. Farzinpour, P., et al., *Altering the dewetting characteristics of ultrathin gold and silver films using a sacrificial antimony layer.* Nanotechnology, 2012. **23**(49): p. 495604.
92. Spanu, D., et al., *Templated Dewetting–Alloying of NiCu Bilayers on TiO2 Nanotubes Enables Efficient Noble-Metal-Free Photocatalytic H2 Evolution.* ACS Catalysis, 2018. **8**(6): p. 5298-5305.
93. Kunwar, S., et al., *Improved Morphological and Localized Surface Plasmon Resonance (LSPR) Properties of Fully Alloyed Bimetallic AgPt and Monometallic Pt NPs Via the One-Step Solid-State Dewetting (SSD) of the Ag/Pt Bilayers.* Nanoscale Research Letters, 2019. **14**(1): p. 332.
94. Ghidelli, M., et al., *Light management in TiO2 thin films integrated with Au plasmonic nanoparticles.* Semiconductor Science and Technology, 2020. **35**(3): p. 035016.
95. Quan, J., et al., *A study on the correlation between the dewetting temperature of Ag film and SERS intensity.* Scientific Reports, 2017. **7**(1): p. 14771.
96. Pandey, P., et al., *Compositional effect on the fabrication of AgxPd1−x alloy nanoparticles on c-plane sapphire at distinctive stages of the solid-state-dewetting of bimetallic thin films.* RSC Advances, 2017. **7**(87): p. 55471-55481.
97. Hwang, C.S.H., et al., *Ag/Au Alloyed Nanoislands for Wafer-Level Plasmonic Color Filter Arrays.* Scientific Reports, 2019. **9**(1): p. 9082.
98. Kang, M., et al., *Bioplasmonic Alloyed Nanoislands Using Dewetting of Bilayer Thin Films.* ACS Applied Materials & Interfaces, 2017. **9**(42): p. 37154-37159.
99. Kunwar, S., et al., *Improved Configuration and LSPR Response of Platinum Nanoparticles via Enhanced Solid State Dewetting of In-Pt Bilayers.* Scientific Reports, 2019. **9**(1): p. 1329.
100. Knight, M.W., et al., *Aluminum for Plasmonics.* ACS Nano, 2014. **8**(1): p. 834-840.
101. Kochergin, V., et al., *Aluminum plasmonic nanostructures for improved absorption in organic photovoltaic devices.* Applied Physics Letters, 2011. **98**(13): p. 133305.
102. Christopher, P., H. Xin, and S. Linic, *Visible-light-enhanced catalytic oxidation reactions on plasmonic silver nanostructures.* Nature chemistry, 2011. **3**(6): p. 467.
103. Su, F., et al., *Dendritic Au/TiO2 nanorod arrays for visible-light driven photoelectrochemical water splitting.* Nanoscale, 2013. **5**(19): p. 9001-9009.
104. Zhou, L., et al., *Aluminum nanocrystals as a plasmonic photocatalyst for hydrogen dissociation.* Nano letters, 2016. **16**(2): p. 1478-1484.
105. Yuzawa, H., T. Yoshida, and H. Yoshida, *Gold nanoparticles on titanium oxide effective for photocatalytic hydrogen formation under visible light.* Applied Catalysis B: Environmental, 2012. **115-116**: p. 294-302.

106. McLellan, J.M., et al., *Comparison of the surface-enhanced Raman scattering on sharp and truncated silver nanocubes.* Chemical Physics Letters, 2006. **427**(1): p. 122-126.
107. Le Ru, E.C. and P.G. Etchegoin, *Single-molecule surface-enhanced Raman spectroscopy.* Annual review of physical chemistry, 2012. **63**: p. 65-87.
108. Jung, K., et al., *Plasmonic Organic Solar Cells Employing Nanobump Assembly via Aerosol-Derived Nanoparticles.* ACS Nano, 2014. **8**(3): p. 2590-2601.
109. Zhang, L., L.O. Herrmann, and J.J. Baumberg, *Size dependent plasmonic effect on BiVO 4 photoanodes for solar water splitting.* Scientific reports, 2015. **5**(1): p. 1-12.
110. Besteiro, L.V. and A.O. Govorov, *Amplified Generation of Hot Electrons and Quantum Surface Effects in Nanoparticle Dimers with Plasmonic Hot Spots.* The Journal of Physical Chemistry C, 2016. **120**(34): p. 19329-19339.
111. Zhang, H. and A.O. Govorov, *Optical Generation of Hot Plasmonic Carriers in Metal Nanocrystals: The Effects of Shape and Field Enhancement.* The Journal of Physical Chemistry C, 2014. **118**(14): p. 7606-7614.
112. Hsieh, P.-Y., et al., *Near infrared-driven photoelectrochemical water splitting: Review and future prospects.* Arabian Journal of Chemistry, 2020.
113. Zhang, Y., et al., *Synthesis of AuPd nanoparticle-decorated graphene-coated ZnO nanorod arrays with enhanced photoelectrochemical performance and stability.* RSC Advances, 2019. **9**(5): p. 2666-2672.
114. Sang, L., S. Zhang, and Y. Gao, *Investigation of plasmonic Cu with controlled diameter over TiO2 photoelectrode for solar-to-hydrogen conversion.* International Journal of Hydrogen Energy, 2019. **44**(47): p. 25486-25494.
115. Kang, S.W., et al., *Plasmonic gold sensitization of ZnO nanowires for solar water splitting.* Materials Today Communications, 2019. **21**: p. 100675.
116. Wei, R.-B., et al., *Plasmon-Enhanced Photoelectrochemical Water Splitting on Gold Nanoparticle Decorated ZnO/CdS Nanotube Arrays.* ACS Sustainable Chemistry & Engineering, 2017. **5**(5): p. 4249-4257.
117. Liu, Y., et al., *Synergistic Effect of Surface Plasmonic particles and Surface Passivation layer on ZnO Nanorods Array for Improved Photoelectrochemical Water Splitting.* Scientific Reports, 2016. **6**(1): p. 29907.
118. Patra, K.K. and C.S. Gopinath, *Bimetallic and Plasmonic Ag–Au on TiO2 for Solar Water Splitting: An Active Nanocomposite for Entire Visible-Light-Region Absorption.* ChemCatChem, 2016. **8**(20): p. 3294-3311.
119. Erwin, W.R., et al., *Plasmon enhanced water splitting mediated by hybrid bimetallic Au–Ag core–shell nanostructures.* Nanoscale, 2014. **6**(21): p. 12626-12634.
120. Sharma, V., et al., *Ag–Au-Bimetal Incorporated ZnO-Nanorods Photo-Anodes for Efficient Photoelectrochemical Splitting of Water.* Energy Technology, 2019. **7**(2): p. 233-239.
121. Siavash Moakhar, R., et al., *AuPd bimetallic nanoparticle decorated TiO2 rutile nanorod arrays for enhanced photoelectrochemical water splitting.* Journal of Applied Electrochemistry, 2018. **48**(9): p. 995-1007.
122. Moakhar, R.S., et al., *Enhancement in solar driven water splitting by Au–Pd nanoparticle decoration of electrochemically grown ZnO nanorods.* Journal of Applied Electrochemistry, 2016. **46**(8): p. 819-827.

123. Lickleder, M., et al., *Dewetted Au Nanoparticles on TiO2 Surfaces: Evidence of a Size-Independent Plasmonic Photoelectrochemical Response.* The Journal of Physical Chemistry C, 2019. **123**(27): p. 16934-16942.
124. Quester, K., et al., *SERS properties of different sized and shaped gold nanoparticles biosynthesized under different environmental conditions by Neurospora crassa extract.* PloS one, 2013. **8**(10).
125. Wang, K., et al., *Stable, Flexible, and High-Performance SERS Chip Enabled by a Ternary Film-Packaged Plasmonic Nanoparticle Array.* ACS Applied Materials & Interfaces, 2019. **11**(32): p. 29177-29186.
126. Severyukhina, A.N., et al., *Nanoplasmonic Chitosan Nanofibers as Effective SERS Substrate for Detection of Small Molecules.* ACS Applied Materials & Interfaces, 2015. **7**(28): p. 15466-15473.
127. Mei, R., et al., *Gold Nanorod Array-Bridged Internal-Standard SERS Tags: From Ultrasensitivity to Multifunctionality.* ACS Applied Materials & Interfaces, 2020. **12**(2): p. 2059-2066.
128. Rao, V.K. and T.P. Radhakrishnan, *Tuning the SERS Response with Ag-Au Nanoparticle-Embedded Polymer Thin Film Substrates.* ACS Applied Materials & Interfaces, 2015. **7**(23): p. 12767-12773.
129. Bi, L., et al., *Highly Sensitive and Reproducible SERS Sensor for Biological pH Detection Based on a Uniform Gold Nanorod Array Platform.* ACS Applied Materials & Interfaces, 2018. **10**(18): p. 15381-15387.
130. Liu, R., et al., *In situ decoration of plasmonic silver nanoparticles on poly(vinylidene fluoride) membrane for versatile SERS detection.* New Journal of Chemistry, 2019. **43**(18): p. 6965-6972.
131. Wang, L., et al., *Magnetic–plasmonic Ni@Au core–shell nanoparticle arrays and their SERS properties.* RSC Advances, 2020. **10**(5): p. 2661-2669.
132. Koleva, M.E., et al., *Fabrication of Ag/ZnO nanostructures for SERS applications.* Applied Surface Science, 2020. **508**: p. 145227.
133. Yan, X., et al., *Sandwich-like Ag@Cu@CW SERS substrate with tunable nanogaps and component based on the Plasmonic nanonodule structures for sensitive detection crystal violet and 4-aminothiophenol.* Applied Surface Science, 2019. **479**: p. 879-886.
134. Purwidyantri, A., et al., *Plasmonic nanomaterial structuring for SERS enhancement.* RSC Advances, 2019. **9**(9): p. 4982-4992.
135. Adams, J., S. Foiles, and W. Wolfer, *Self-diffusion and impurity diffusion of fee metals using the five-frequency model and the embedded atom method.* Journal of Materials Research, 1989. **4**(1): p. 102-112.
136. Dick, K., et al., *Size-Dependent Melting of Silica-Encapsulated Gold Nanoparticles.* Journal of the American Chemical Society, 2002. **124**(10): p. 2312-2317.
137. van der Hoeven, J.E.S., et al., *In Situ Observation of Atomic Redistribution in Alloying Gold–Silver Nanorods.* ACS Nano, 2018. **12**(8): p. 8467-8476.
138. Herz, A., et al., *Solid-state dewetting of Au/Ni bilayers: The effect of alloying on morphology evolution.* Journal of Applied Physics, 2014. **116**(4): p. 044307.
139. Lu, L., et al., *Cooperative plasmonic effect of Ag and Au nanoparticles on enhancing performance of polymer solar cells.* Nano Letters, 2012. **13**(1): p. 59-64.
140. Benten, W., et al., *Photon Emission Spectroscopy of Single Oxide-Supported Ag-Au Alloy Clusters.* Physical Review B, 2005. **72**(4): p. 045403.

141. Han, Q., et al., *Ag-Au alloy nanoparticles: Synthesis and in situ monitoring SERS of plasmonic catalysis.* Sensors and Actuators B: Chemical, 2016. **231**: p. 609-614.
142. Han, S.W., Y. Kim, and K. Kim, *Dodecanethiol-Derivatized Au/Ag Bimetallic Nanoparticles: TEM, UV/VIS, XPS, and FTIR Analysis.* Journal of Colloid and Interface Science, 1998. **208**(1): p. 272-278.
143. Chimentao, R., et al., *Synthesis of silver-gold alloy nanoparticles by a phase-transfer system.* Journal of materials research, 2006. **21**(1): p. 105-111.
144. Kruse, N. and S. Chenakin, *XPS characterization of Au/TiO2 catalysts: binding energy assessment and irradiation effects.* Applied Catalysis A: General, 2011. **391**(1-2): p. 367-376.
145. Kittel, T. and E. Roduner, *Charge Polarization at Catalytic Metal–Support Junctions, Part A: Kelvin Probe Force Microscopy Results of Noble Metal Nanoparticles.* The Journal of Physical Chemistry C, 2016. **120**(16): p. 8907-8916.
146. Macias, G., et al., *Surface roughness boosts the SERS performance of imprinted plasmonic architectures.* Journal of Materials Chemistry C, 2016. **4**(18): p. 3970-3975.
147. Carrara, M., et al., *Modulation of the Work Function in Layer-by-Layer Assembly of Metal Nanoparticles and Poly-L-lysine on Modified Au Surfaces.* ChemPhysChem, 2004. **5**(4): p. 571-575.
148. Schnippering, M., et al., *Electronic properties of Ag nanoparticle arrays. A Kelvin probe and high resolution XPS study.* Physical Chemistry Chemical Physics, 2007. **9**(6): p. 725-730.
149. Gao, L., L. Fan, and J. Zhang, *Selective Growth of Ag Nanodewdrops on Au Nanostructures: A New type of Bimetallic Heterostructure.* Langmuir, 2009. **25**(19): p. 11844-11848.
150. Gould, A.L., et al., *Segregation effects on the properties of (AuAg)147.* Physical Chemistry Chemical Physics, 2014. **16**(39): p. 21049-21061.
151. Mohan, S., B. Subramanian, and G. Sarveswaran, *A prototypical development of plasmonic multiferroic bismuth ferrite particulate and fiber nanostructures and their remarkable photocatalytic activity under sunlight.* Journal of Materials Chemistry C, 2014. **2**(33): p. 6835-6842.
152. Hosseinpour-Mashkani, S.M. and M. Ramezani, *Silver and silver oxide nanoparticles: Synthesis and characterization by thermal decomposition.* Materials Letters, 2014. **130**: p. 259-262.
153. Magari, Y., et al., *Origin of work function engineering of silver oxide for an In–Ga–Zn–O Schottky diode.* Applied Surface Science, 2020. **512**: p. 144519.
154. Lin, S., et al., *Rapid and sensitive SERS method for determination of Rhodamine B in chili powder with paper-based substrates.* Analytical Methods, 2015. **7**(12): p. 5289-5294.
155. Tan, K.H., et al., *Tunable Spectrum Selectivity for Multiphoton Absorption with Enhanced Visible Light Trapping in ZnO Nanorods.* Small, 2018. **14**(20): p. 1704053.
156. Chiu, Y.-H., et al., *Fully Depleted Ti–Nb–Ta–Zr–O Nanotubes: Interfacial Charge Dynamics and Solar Hydrogen Production.* ACS Applied Materials & Interfaces, 2018. **10**(27): p. 22997-23008.
157. Zhang, Y., et al., *Sensing the Charge State of Single Gold Nanoparticles via Work Function Measurements.* Nano Letters, 2015. **15**(1): p. 51-55.

# Appendix

## Appendix A: Figures

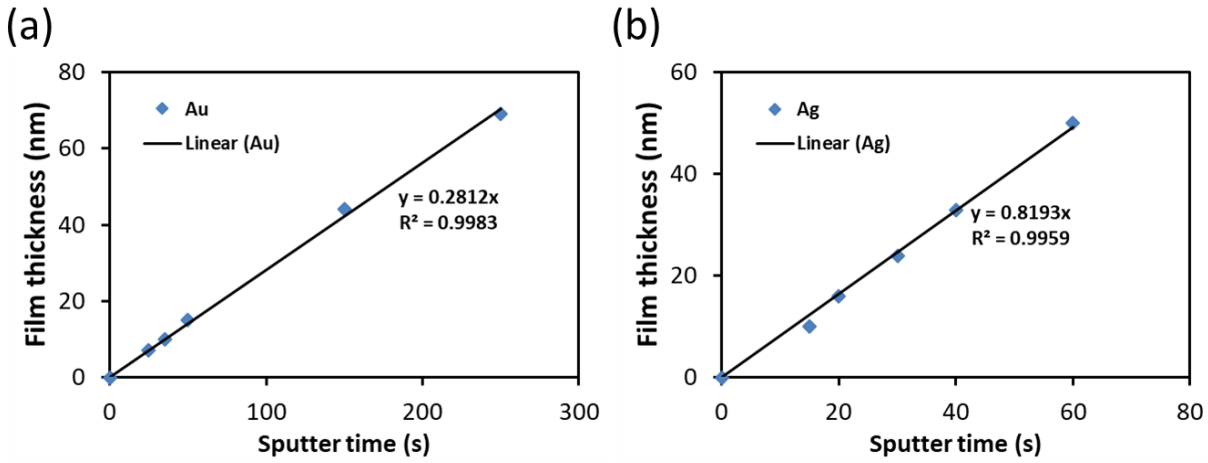


**Figure S1.** Film thickness calibration of (a) Au and (b) Ag using AFM thickness measurement.

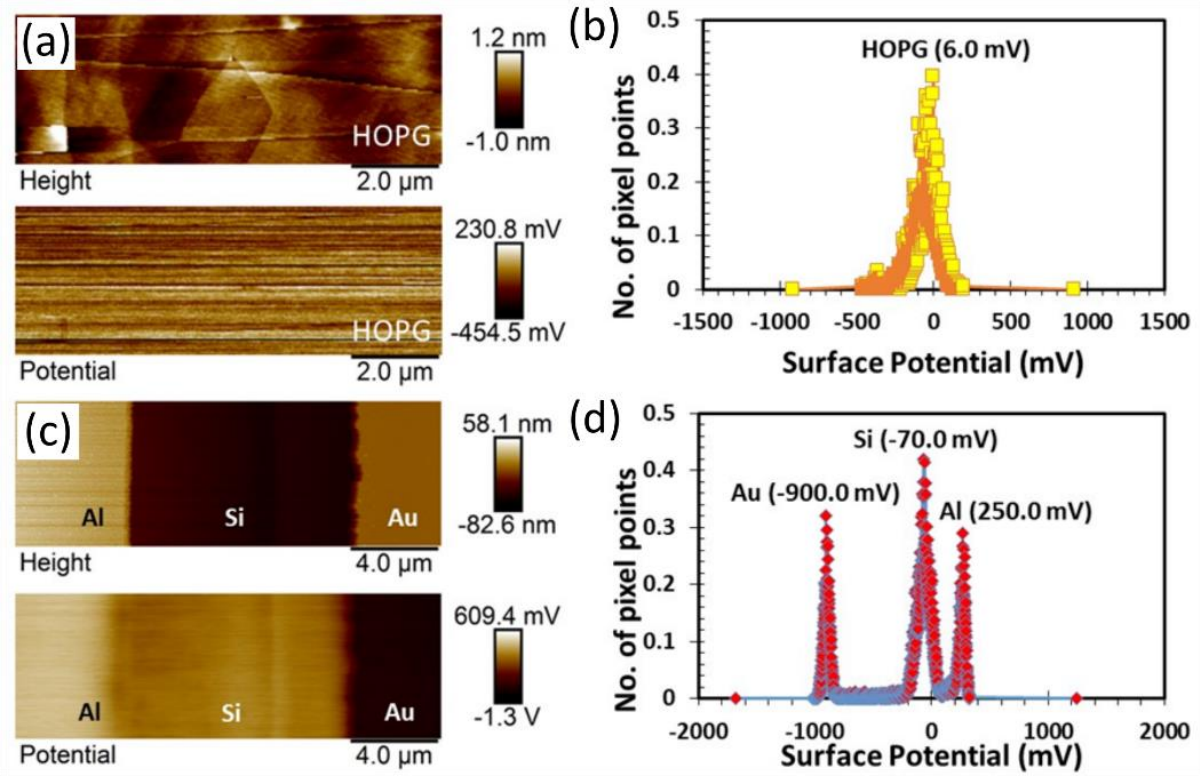


**Figure S2.** KPFM calibration using (a) highly orientated pyrolytic graphite (HOPG) and (b) surface potential histogram for HOPG. (c) Au-Si-Al standard sample and (d) surface potential histogram for Au-Si-Al standard sample.

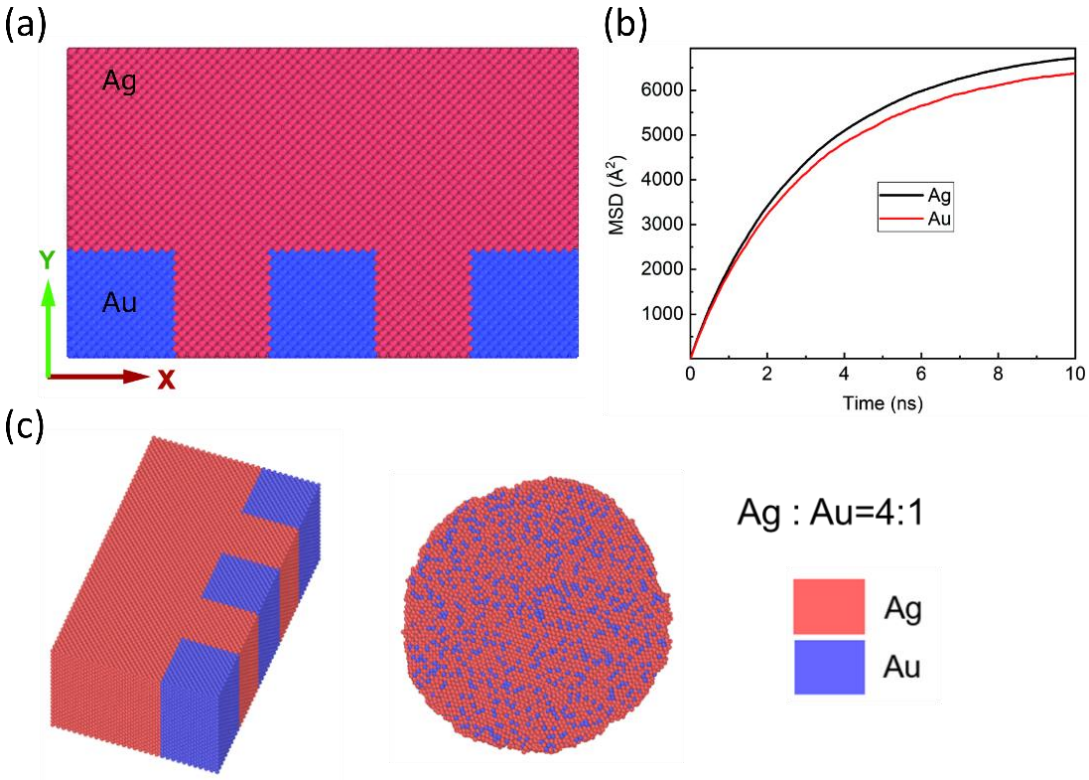


**Figure S3**. (a) Initial model showing the deposition process of Ag and Au films and (b) Mean square displacement (MSD) of Ag and Au. (c) Molecular dynamics simulation showing the element distribution of 0.25 Au/Ag BNPs. The simulation work is collaborated with Dr. Yu Hao, Dr Wu Bao and Dr Wu HengAn.

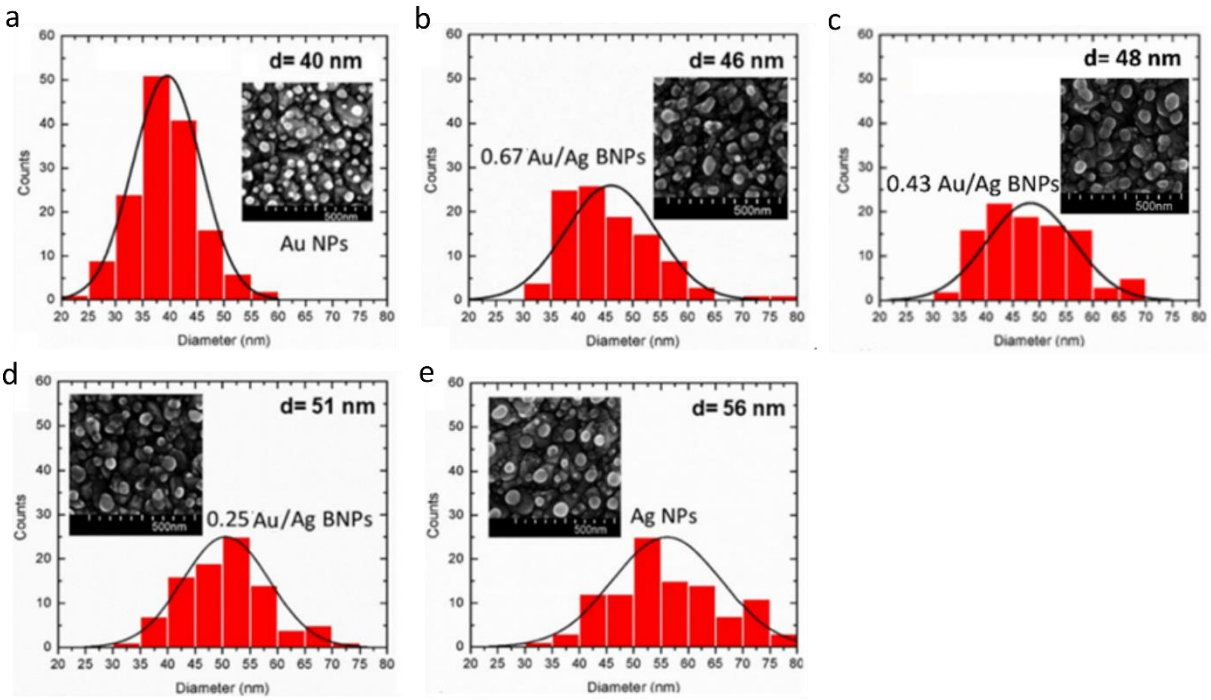


**Figure S4.** Histogram plot showing the average diameter and its distribution of monometallic (a) Au NPs, (b) 0.67 Au/Ag BNPs, (c) 0.43 Au/Ag BNPs, (d) 0.25 Au/Ag BNPs, and (e) Ag NPs.

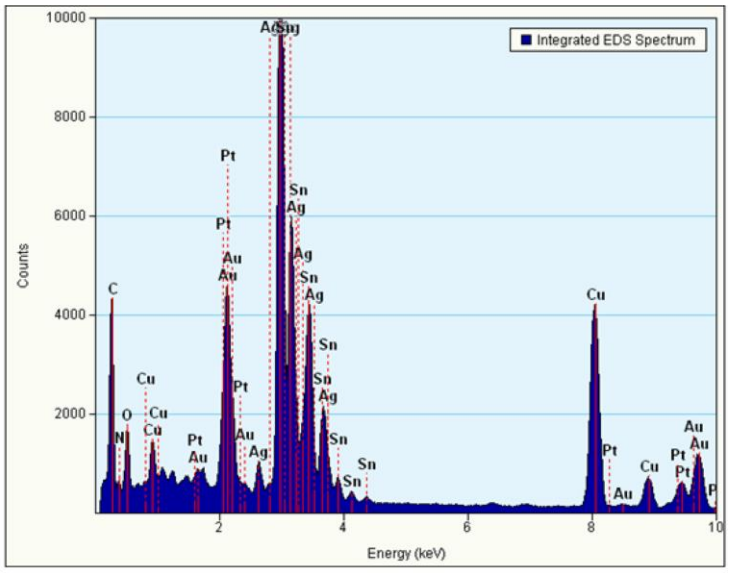


**Figure S5.** Energy dispersive spectroscopy (EDS) spectrum of 0.25 Au/Ag bimetallic nanoparticles. Few elements are detected namely Ag, Au, Sn and O, whereas the observed Cu and

Pt peaks attributed to Cu grid and Pt was used for the preparation of lamella lift out process, respectively.

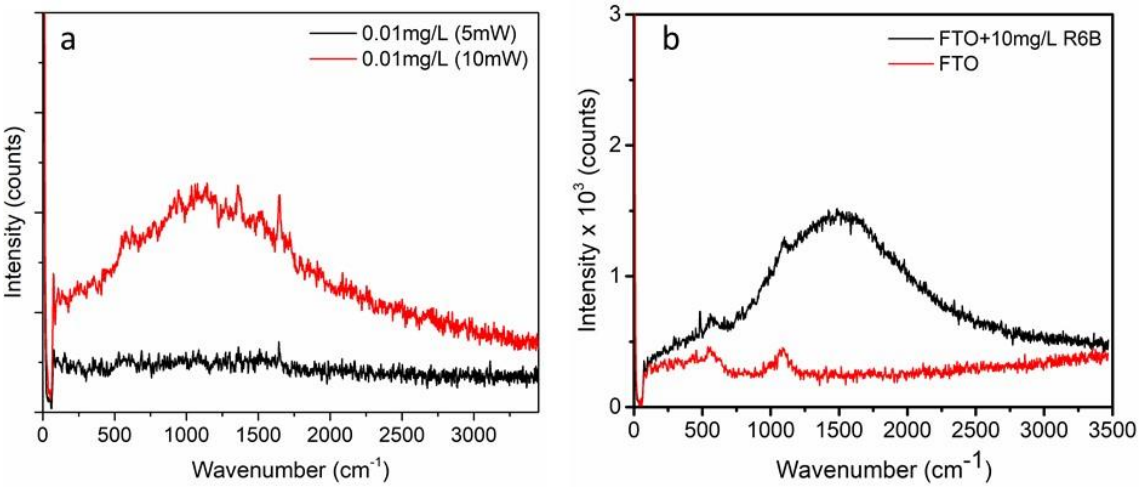


**Figure S6.** SERS signal of 0.01 mg/L R6B detected using 0.25 Au/Ag BNPs under different irradiation power of 5 mW and 10 mW, and (b) is the SERS respond of R6B detected using a bare FTO substrate.

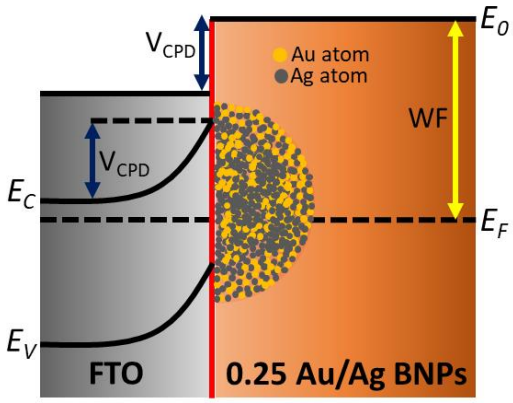


**Figure S7.** Schematic diagram illustrates the work function (WF) and contact potential difference (CPD) after electrical contact between FTO and 0.25 Au/Ag BNPs.

In KPFM, the oscillating conductive tip is utilized as the reference electrode of a Kelvin probe. As the tip approaches the sample surface, a capacitor is formed, and the contact potential difference (CPD) between the two electrodes results in an electrostatic tip-surface force. Thus, the CPD value can be determined by applying a direct current (DC) voltage to nullify the electrostatic force.

The surface potential or CPD of the NPs and BNPs can be estimated using the following relation [157]:

$$\text{Contact Potential Difference (CPD)} = (WF_{tip} - WF_{NPs}) / e \qquad \text{Equation S1}$$

where $WF_{tip}$ is the work function of cantilever tip, $WF_{NPs}$ is the work function of the NPs, and $e$ is the elementary charge.

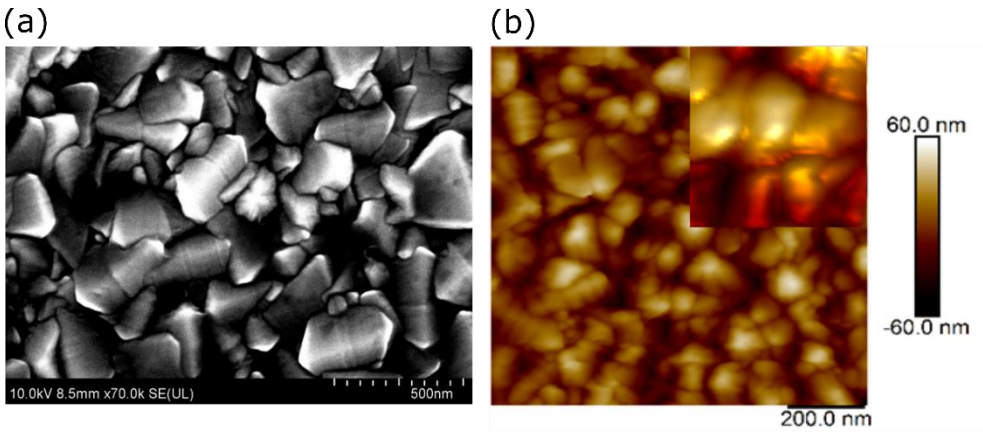


**Figure S8.** (a) FESEM image of the FTO substrate. (b) AFM topography images of FTO substrate. The inset shows the 3D topography mapping.

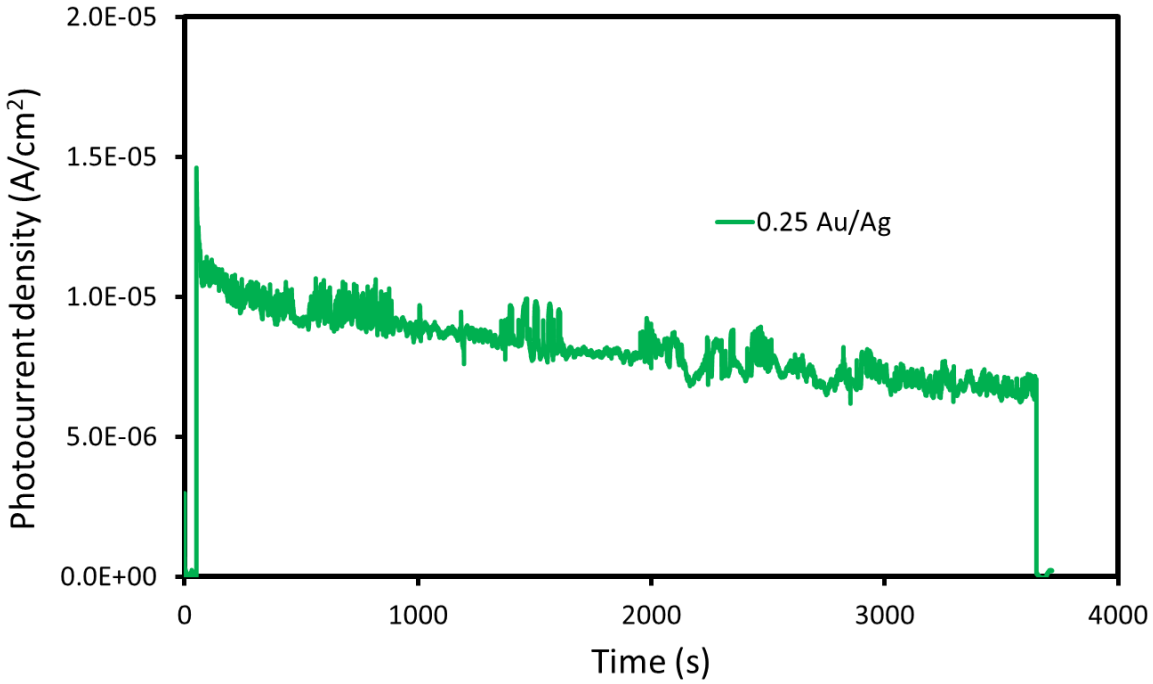


**Figure S9.** Photo-stability measurement of 0.25 Au/Ag-ZnO photo-anode under AM 1.5 using 0.5 M $Na_2CO_3$ electrolyte solution with 1 Sun illumination (with an intensity of 100 mW/cm$^2$).

Appendix B: Tables

**Table S1.** List of thickness of deposited film before the dewetting process and EDS atomic ratio of the synthesized film.

| Sample | Thickness of deposited film (nm) | | EDS atomic ratio | |
|---|---|---|---|---|
| | Au | Ag | Au | Ag |
| Ag NPs | 0 | 10 | 0 | 1.00 |
| Au NPs | 10 | 0 | 1.00 | 0 |
| 0.25 Au/Ag BNPs | 2 | 8 | 0.24 | 0.76 |
| 0.43 Au/Ag BNPs | 3 | 7 | 0.34 | 0.66 |
| 0.67 Au/Ag BNPs | 4 | 6 | 0.43 | 0.57 |

**Table S2.** List of work function and contact potential difference, Vcpd of monometallic and bimetallic nanoparticles measured using KPFM analysis.

| Sample | Work Function (eV) | $V_{cpd}$ (mV) |
|---|---|---|
| Ag NPs | 5.18 | -118.88 |
| Au NPs | 5.29 | -245.80 |
| 0.25 Au/Ag BNPs | 5.16 | -99.16 |
| 0.43 Au/Ag BNPs | 5.21 | -124.27 |
| 0.67 Au/Ag BNPs | 5.26 | -154.50 |

**Table S3.** X-ray photoelectron spectroscopy (XPS) binding energy peak positions of Au ($4f_{7/2}$ and $4f_{5/2}$) and Ag ($3d_{5/2}$ and $3d_{3/2}$).

| Sample | Au | | Ag | |
|---|---|---|---|---|
| | $4f_{7/2}$ | $4f_{5/2}$ | $3d_{5/2}$ | $3d_{3/2}$ |
| Au NPs | 84.0 | 87.7 | n/a | n/a |
| 0.67 Au/Ag BNPs | 84.1 | 87.8 | 368.1 | 374.1 |
| 0.43 Au/Ag BNPs | 84.1 | 87.8 | 367.9 | 373.9 |
| 0.25 Au/Ag BNPs | 84.1 | 87.8 | 367.7 | 373.7 |
| Ag NPs | n/a | n/a | 368.2 | 374.2 |

**Table S4.** Results from measurement and calculation of sheet resistance of FTO, Au NPs and Ag NPs, and Au/Ag BNPs.

| Sample | V (V) | I (A) | Sheet Resistance (Ω/sq) |
|---|---|---|---|
| FTO | 2 | 0.029931 | 13.00 |
| Au NPs | 2 | 0.038498 | 10.11 |
| 0.67 Au/Ag BNPs | 2 | 0.05244 | 7.42 |
| 0.43 Au/Ag BNPs | 2 | 0.058989 | 6.60 |
| 0.25 Au/Ag BNPs | 2 | 0.084078 | 4.63 |
| Ag NPs | 2 | 0.081723 | 4.76 |

**Table S5.** Fitting results from the electrochemical impedance spectroscopy (EIS) measurements.

| Sample | $R_1$ (ohm) | $R_2$ (ohm) | $R_3$ (ohm) | $R_4$ (ohm) | $C_1$ (F) | $CPE_1$ (F) | $CPE_2$ (F) |
|---|---|---|---|---|---|---|---|
| 0.25 Au/Ag-ZnO | 4.627 | 4.376 | 15.19 $x10^3$ | 4.585 | 376.9 $x10^{-9}$ | 85.61 $x10^{-6}$ | 856.0 $x10^{-3}$ |
| Pristine ZnO | 30.90 | 230.6 $x10^3$ | 33.83 $x10^3$ | 11.17 $x10^3$ | 4.425 $x10^{-6}$ | 18.32 $x10^{-6}$ | 893.7 $x10^{-3}$ |
| Au-ZnO | 17.14 | 666.3 2 | 23.86 $x10^3$ | 17.736 | 3.263 $x10^{-6}$ | 9.173 $x10^{-6}$ | 780.2 $x10^{-3}$ |
| Ag-ZnO | 10.38 | 7.972 | 17.053 $x10^3$ | 4.697 | 6.061 $x10^{-6}$ | 49.07 $x10^{-6}$ | 817.8 $x10^{-3}$ |
| 0.67 Au/Ag-ZnO | 15.92 | 301.6 | 21.19 $x10^3$ | 15.67 | 3.817 $x10^{-6}$ | 7.310 $x10^{-6}$ | 621.3 $x10^{-3}$ |
| 0.43 Au/Ag-ZnO | 13.07 | 128.8 | 19.42 $x10^3$ | 10.05 | 3.360 $x10^{-6}$ | 7.608 $x10^{-6}$ | 546.7 $x10^{-3}$ |

## Appendix C: Calculations and Methodology

### Appendix C1: Surface-Enhanced Raman Spectroscopy (SERS) enhancement factor calculations

The SERS enhancement factor is calculated by comparing the SERS signals excited on the Congo red dye molecule adsorbed on the nanoparticles and reference sample (FTO substrate). The equation used to calculate the SERS enhancement factor can be expressed as:

$$SERS\ enhancement\ factor = \frac{I_{SERS}}{N_{SERS}} \times \frac{N_{Raman}}{I_{Raman}} \qquad \text{Equation S2}$$

Where $N_{Raman}$ and $N_{SERS}$ denote the number of Raman active probe molecules on the reference sample and nanoparticles sample, respectively, while $I_{Raman}$ and $I_{SERS}$ denote the corresponding intensity from the reference sample and nanoparticles sample, respectively. As the value of $N_{Raman}$ and $N_{SERS}$ is 1 M and $5x10^{-6}$ M, respectively, hence the equation can be expressed as:

$$SERS\ enhancement\ factor = \frac{I_{Surf}}{I_{Raman}} \times (2 \times 10^5) \qquad \text{Equation S3}$$

Appendix C2: Calculation of lattice spacing from XRD results using Bragg's Law

Bragg's Law can be expressed using the equation as shown below.

$$n\lambda = 2dsin(\theta) \qquad \text{Equation S4}$$

where $\lambda$ is the x-ray wavelength which has value of 1.54Å, $n$ is an integer which is commonly expressed as 1, $d$ is the lattice spacing, and $\theta$ is the diffraction angle. To determine the lattice spacing, the equation can be rearranged to be:

$$d = \frac{1.54}{2\sin(\theta)} \qquad \text{Equation S5}$$

Appendix C3: Calculation of Quantitative Work Function

The formula to calculate the work function of the samples can be expressed as:

$$CPD(V) = \frac{\left(W_{Tip}(eV) - W_{sample}(eV)\right)}{e} \qquad \text{Equation S6}$$

Where $CPD(V)$ is the surface potential value between the sample and the cantilever tip, $W_{Tip}(eV)$ is the work function of the cantilever tip, $W_{NPs}(eV)$ is the work function of the sample, and $e$ is the elementary charge. $W_{Tip}$ was calibrated using HOPG and determined to be 4.6 eV. Result of quantitative work function of nanoparticles were tabulated in Table S2.

Appendix C4 Calculation of Sheet Resistance ($R_s$)

The formula to calculate the sheet resistance of a thin film can be expressed as

$$R_s = K(\frac{V}{I})$$ Equation S7

Where $K$ is the geometric factor, which can be expressed as $\pi/(\ln 2) = 4.53$, for a semi-infinite thin film. $V$ and $I$ is the applied voltage and measured current, respectively.

However, as a 2-point probe system was utilized instead of a 4-point probe system, a contact resistance, $R_{contact}$ was introduced into the measurement.

$$R_s = 4.53\ R_{contact}\ (\frac{V}{I})$$ Equation S8

In order to determine $R_{contact}$, the sheet resistance of FTO was assumed to be $13\ \Omega/\text{sq}$ as measured by the manufacturer.

$$13 = 4.53\ R_{contact}\ (\frac{2}{0.029931})$$ Equation S9

By rearranging the equation, $R_{contact}$ was calculated to be 0.04294. Therefore, the sheet resistance can be approximated by substituting the calculated $R_{contact}$ value into Equation S10 and it is as shown below. The sheet resistance values are tabulated in Table S4.

$$R_s = 4.53\ (0.04294)(\frac{V}{I})$$ Equation S10